

ION BEAM-PLASMA INTERACTIONS

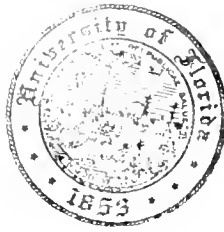
By

WILLIAM ARTHUR DUNNILL

A DISSERTATION PRESENTED TO THE GRADUATE COUNCIL OF
THE UNIVERSITY OF FLORIDA
IN PARTIAL FULFILLMENT OF THE REQUIREMENTS FOR THE
DEGREE OF DOCTOR OF PHILOSOPHY

UNIVERSITY OF FLORIDA

June, 1965



UNIVERSITY OF FLORIDA



3 1262 08552 5466

ACKNOWLEDGMENTS

The author wishes to thank the members of his committee: Professors J. W. Flowers, J. Kronsbein, T. L. Bailey, F. E. Dunnam, and R. W. Cowan for their assistance throughout his graduate program. Especially he wishes to express his thanks to Dr. Flowers for suggesting the topic of this dissertation and for general assistance and suggestions. He also wishes to show his appreciation to Dr. Kronsbein for the many discussions covering theoretical work in the field.

The author is also very grateful to his wife Alice for her patience and understanding during the final stages of his work.

Finally, the author wishes to gratefully acknowledge the partial support given him by the Atomic Energy Commission, under Contract AT-(40-1) 2783.

TABLE OF CONTENTS

	Page
ACKNOWLEDGMENTS	ii
LIST OF ILLUSTRATIONS	iv
 CHAPTER	
I. INTRODUCTION	1
II. THEORY	4
III. APPARATUS AND PROCEDURE	28
IV. RESULTS	56
V. CONCLUSIONS	94
LIST OF REFERENCES	104
BIOGRAPHICAL SKETCH	106

LIST OF ILLUSTRATIONS

Figure		Page
1.	Voltage drop measured across two probes 0.345 m apart as a function of the magnetic field	10
2.	Escape flux of ions transversally to the magnetic field from a cold-cathode P. I. G. discharge working with hydrogen	12
3.	Escape flux of ions transversally to the magnetic field for $B > 1000$ gauss	13
4.	The critical magnetic field is plotted as a function of the pressure	15
5.	Left-handed screw instability for $m = 1$	18
6.	A cross sectional view of the upper part of Fig. 5	19
7.	A cross section of the Penning discharge with the charge distribution and resultant drifts .	23
8.	High energy dual beam experimental apparatus . .	30
9.	Magnetic field strength along the axis of the cone is plotted as a function of the distance from the cone tip	32
10.	High current ion source	37
11.	Detail of the cathode of the high current source	39
12.	The magnetic field along the arc axis is plotted as a function of the distance from the anode	40
13.	Side and front view of the water-cooled magnetic anode	42

Figure		Page
14.	Radial dependence of the magnetic field on the surface of the anode is plotted for three different magnet currents	43
15.	Diagram of the pulse circuit and the arc	45
16.	Disk pulsing arrangement	46
17.	Diagram of the current pulse circuit and the arc	47
18.	Reflex arc discharge apparatus	51
19.	Detail of the anode-button structure of the reflex arc	53
20.	Detail of the moveable cathode of the reflex arc discharge	54
21.	Collector potential in an air plasma is plotted as a function of the magnetic field	57
22.	Collector potential is plotted as a function of the hydrogen ion beam energy	59
23.	Collector potential in an argon plasma is plotted as a function of the magnetic field	60
24.	Collector potential in a helium plasma is plotted as a function of the magnetic field	61
25.	Collector potential is plotted as a function of the magnetic field	63
26.	Collector current I_c is plotted as a function of the source pressure for a 2.5-amp arc with a 1-inch-diameter shield aperture	65
27.	Collector current I_c is plotted as a function of the collector voltage V_c for a 2.5-amp arc	67
28.	Collector current I_c is plotted as a function of the collector voltage V_c for a 1.5-amp arc	68

Figure		Page
29.	The beam current from a 1.5-amp arc is plotted as a function of the radially increasing anode magnetic field	70
30.	The beam current from a 1.5-amp arc is plotted as a function of the radially decreasing anode magnetic field	71
31.	Pulse voltage measured across 47-ohm resistor between the collector and ground	73
32a.	The pulsed beam voltage resulting from a 60-sec.- 200-volt arc pulse is shown as a function of time	74
32b.	The pulsed beam voltage resulting from a 60-sec - 400-volt arc pulse is shown as a function of time	74
33.	The arc current is plotted as a function of the maximum sustainable pulse voltage at a pressure of .22 microns	75
34.	The pulsed beam voltage resulting from a 6-amp arc pulse is plotted as a function of time	77
35.	The oscillogram represents the variable current fluctuation in time to the probe and arc electrodes	79
36.	The frequency is plotted as a function of the magnetic field for different cathode-button separation distances	80
37.	The frequency is plotted as a function of the cathode-button separation distance for different magnetic fields	81
38.	The frequency is plotted as a function of the pressure for given cathode-button separation distances	83
39.	The oscillogram represents the constant current fluctuation in time to the probe and arc electrodes	84

Figure		Page
40.	The frequency is plotted as a function of the button radius	85
41.	The frequency is plotted as function of the arc current	86
42.	The floating potential of the variable probe is plotted as a function of the radial position of the probe	88
43.	The arc voltage is plotted as a function of the magnetic field for different cathode-button separation distances	90
44.	The arc voltage is plotted as a function of the cathode-button separation distance for different button diameters	91
45.	The arc voltage is plotted as a function of the button diameter for three different pressures	92

CHAPTER I

INTRODUCTION

The interaction of a beam of charged particles with a plasma has been studied in great detail since Bohm and Gross have shown that a constant velocity homogeneous beam moving through a homogeneous plasma is unstable.¹ Since the plasma density n_0 , even for a dense plasma, is generally small ($n_0 \approx 10^{12} - 10^{14}$ particles/cm³), the energy lost per unit length by a charged particle is insignificant, being of the order of $10^{-3} - 10^{-5}$ eV per cm.² However, in the majority of cases, the beam becomes self-modulated, leading to a coherent interaction between the particles in the beam and plasma. The energy lost by the beam particles in exciting oscillations can be considerable, being of the order of $10^3 - 10^4$ eV per cm for particle bunches of $N \approx 10^7 - 10^8$.² The fact that this interaction energy is larger for beams and charged particle bunches, than it is for individual particles, may be either an advantage or disadvantage. For example, advantage may be taken of this phenomena when devising means of injecting plasma into magnetic traps and in increasing the energy of the plasma particles.

For instabilities to arise, the number of particles in the beam giving up energy to the electromagnetic field must exceed the number of particles in the plasma absorbing energy from the field. This requirement has been shown to impose certain restrictions on the particle velocity distributions in the beam and in the plasma.³ If the ions alone have a peaked velocity, the electron species must have an average thermal energy covering the ion velocity range for instabilities to occur. This indicates a restriction on ion beam instabilities unless the electron distribution is of a special nature. This leads one to think that it is really the electrons that govern instabilities, even in the ion beam case.

Thus far in all devices designed to study means of controlling fusion, instabilities of various natures have arisen with the result being somewhat the same in each case. As the density or energy of the charged particles has been increased toward thermonuclear values, large particle losses from the containing region have suddenly appeared, effectively destroying the plasma. These instabilities are normally accompanied by radio frequency noise over a large portion of the spectrum. Clearly, the understanding of such oscillations is of fundamental importance in understanding beam-plasma systems.

In this dissertation the work with possible oscillatory systems has been divided into three phases. The first phase has been an investigation of high energy beam-plasma combinations in which the beam was a hydrogen ion beam in the energy range from 10 to 20 keV with currents of 5 to 10 ma. The second phase concerned a low energy ion beam in the range of several hundreds of volts. Finally, a discharge of a reflex type has been studied as a beam-plasma interacting system. For this system both an ion beam or stream and an electron beam are present at low energies with relatively large current densities.

CHAPTER II

THEORY

In the investigation of plasma-ion beam interactions, results of other experiments and theories have been useful. Since a great deal of work has been done on studying plasma-electron beam interactions, it has been advantageous to compare this work with analogous plasma-ion beam experiments.

Dual Beam-Plasma Interaction Theory

The first phase of this work, in a sense, concerned a dual ion beam-plasma interaction, so the analogous two electron beam-plasma interaction has been investigated and studied. Standing waves of longitudinal plasma electron oscillations have been produced between boundary electrodes by oppositely directed, independent, interpenetrating electron beams passing through a plasma.⁴ The theory describing this two stream instability determined by Bohm and Gross may be obtained by examining the dispersion relation found by considering two oppositely directed beams moving through a background plasma.⁵

In order to solve for the organized motion of particles in a plasma, consider a system whose velocity distribution is given by

$$dN_o = n_o f(V_o) dV_o = n_o f(U_o + V_1) dU_o \quad (1)$$

where U_o is the velocity in the wave system and V_1 is the velocity of the wave in the laboratory system.

The average potential $\phi(x)$, assumed to vary trigonometrically in space and time, causes each particle to undergo a periodic change of velocity and a corresponding change of its contribution to the density.

Solving for the total charge density ρ by integrating over all U_o and inserting this into Poisson's equation gives

$$-\nabla^2 \phi = 4\pi\rho = 4\pi n_o \left[1 - \frac{f(V_o) dV_o}{\left(1 + \frac{2e\phi(x)}{mU_o^2}\right)^{1/2}} \right] \quad (2)$$

Assuming $\phi(x)$ is static in the wave system restricts us to traveling wave solutions for all quantities of the form $(x - V_1 t)$. By assuming small values for $2e\phi(x)/mU_o^2$, we can expand the square root, obtaining the linear approximation

$$-\nabla^2 \phi = \frac{4\pi n_o e^2}{m} \phi \int \frac{f(V_o) dV_o}{(V_o - V_1)^2} \quad (3)$$

The dispersion relation found by writing $V_1 = \omega/k$ and $\nabla^2 \phi = -k^2 \phi$ yields the non-trivial solution of

$$1 = \frac{4\pi n_0 e^2}{m} \int \frac{f(V_0) dV_0}{(\omega - k \cdot V_0)^2} . \quad (4)$$

For the two beam-plasma interaction system, we let $f(V_0)$ be $\delta/2$, when $|V_0|$ lies between a and $a - \delta$, and $f(V_0)$ be 0 for all other values of V_0 . This means each beam has a velocity spread of width δ while the total system has a zero mean velocity.

Neglecting collisions and restricting k to small values yields the two roots

$$\omega^2 \approx \omega_p^2 + k^2 [a^2 + (a - \delta)^2 + a(a - \delta)] \quad (5)$$

and
$$\omega^2 \approx -k^2 a(a - \delta) . \quad (6)$$

Unless $\delta = a$, the second root corresponds to an imaginary frequency, representing the two beam-plasma instability.

To experimentally investigate the dual beam-plasma interaction, it is necessary to produce either two beams or a reflected component of a single beam available from a single source. Since two sources were unavailable, it was decided to use a reflected component of an ion beam to initiate the dual beam studies.

When an electron beam impinges on a target in the presence of a plasma, the negative potential build-up becomes related to the beam velocity and its distribution. Electrons can then be reflected providing essentially the situation of two opposing beams with intermodulation, and thus feedback of any growing disturbance on either beam. For the ion beam case a similar behaviour has been found difficult to achieve since the ion beam will not support positive charge and potential required in the region of reflection. This is primarily due to the high mobility of electrons to the target, allowing charge, and hence, potential neutralization to take place.

It has been found that intense hydrogen ion beams are automatically space-charge neutralized when focused by a magnetic solenoid lens unless an electron drain is provided.⁶ If electrons are drawn out of the drift space by a positive bias on the target, for example, a spreading may be visually observed in the beam. This is consistent with the expected behaviour of the beam with no neutralization. If a transverse magnetic field is applied near the target, space-charge neutralization takes place whether the target is biased or not. When the target is positively biased, the transverse magnetic field from the target bias creates an $E \times B$ electron trap in front of the target. This electron build-up effectively cancels the positive bias on

the target, so the electrons remain in the drift space and charge neutralize the ion beam. With this thought in mind, a transverse magnetic field in the target region of the ion beam could allow positive potential build-up sufficient to produce the required reflected ion beam component.

High Current Source and Reflex Discharge Theory

The theory discussing the processes involved in the second and third phases of this tract will now be considered. This grouping is done since both experiments are concerned with the fact that particle diffusion rates may be coupled to the low frequency oscillations found in the discharge. Much work has been done on this problem since Bohm found that single particle ambipolar diffusion theory does not predict the particle diffusion rates across magnetic field lines in various discharges.⁷ Bohm postulated that fluctuations of the charge density may produce electric fields which give rise to particle drifts across magnetic fields. Simon has shown that this discrepancy between theory and experiment is due to the fact that diffusion across the magnetic field is not ambipolar in character in all experiments.⁸ This absence of ambipolar diffusion is due to the highly anisotropic conductivity in the medium, resulting in the observed higher diffu-

sion rate. Electrons moving parallel to the magnetic field neutralize the space charge set up by the ions moving perpendicular to the magnetic field. This electron flow parallel to the magnetic field is completed through the conducting electrodes at the ends of the discharge and is called the short-circuit effect. With this in mind, Hoh and Lehnert devised an experiment eliminating the short-circuit effect by using a very long discharge tube with a diverging magnetic field at the tube ends.⁹ Their experiments showed that the classical theory for ambipolar diffusion held below a critical magnetic field B_c . Above this field value, an instability set in resulting in a diffusion rate much greater than that given by the classical theory. The increased diffusion was inferred from noting that the potential difference in Fig. 1 along the column increased when the magnetic field was above B_c .⁹ Measurements of the ion current to a negatively charged probe at the tube wall supported this view. The characteristics remained approximately the same for hydrogen, helium, argon and krypton plasmas. The fact that the short-circuit effect was eliminated by the geometry of the system and that the noise in the discharge current increased when abnormal diffusion set in indicated oscillations, turbulence, or other asymmetric large scale motion in the plasma. Bonnal et al.

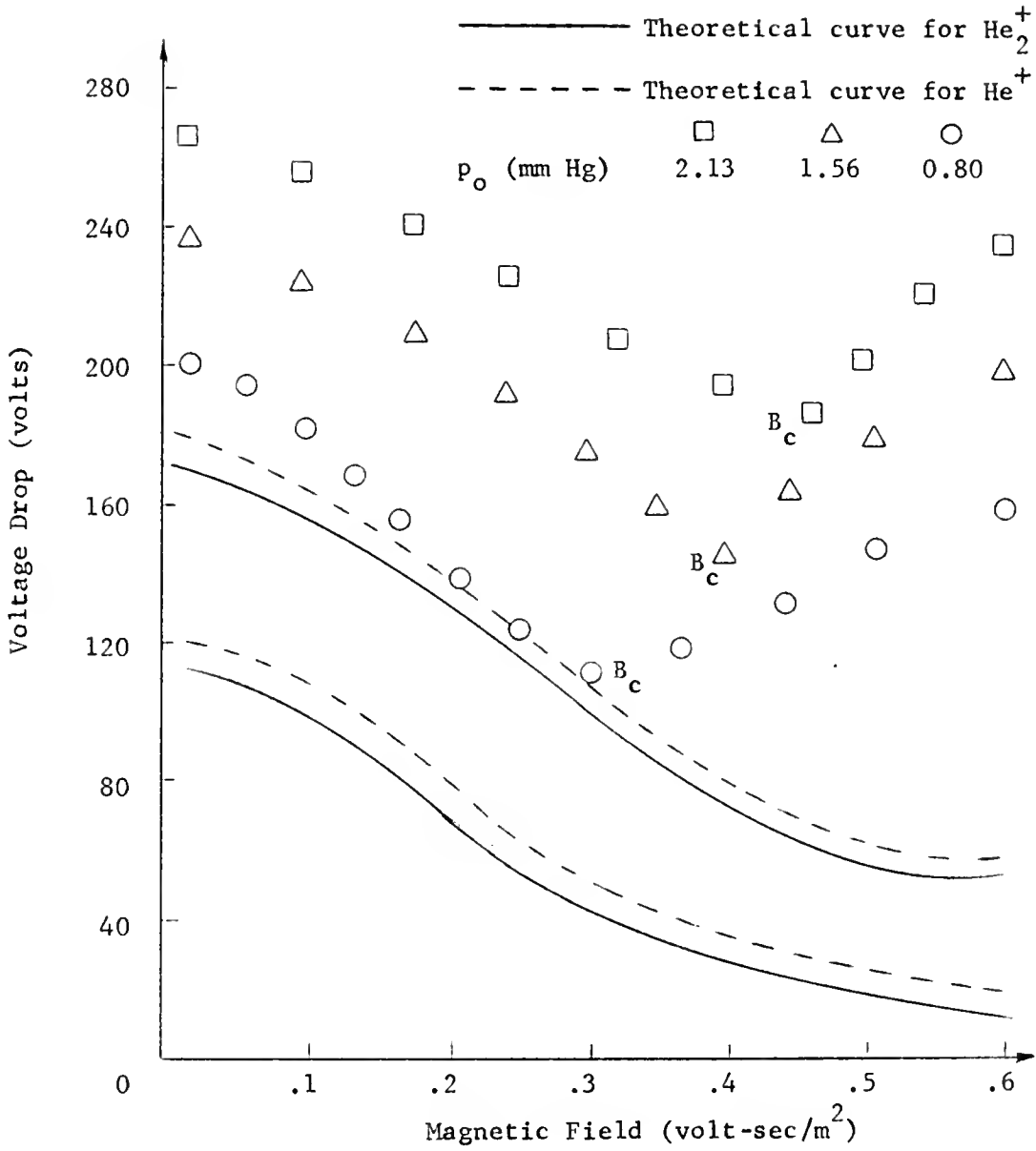


Fig. 1. Voltage drop measured across two probes 0.345 m apart as a function of the magnetic field. Full curves are calculated from the theory for molecular ions and the dashed curves are for atomic ions.

measured the particle escape flux as a function of the magnetic field and pressure.¹⁰ Figures 2 and 3 show that above a critical magnetic field B_c , a new diffusion mode appears accompanied by noise emission in which the escape flux increases with the magnetic field. Above B_m , the escape flux decreases again along with the noise level. As the pressure is decreased, both B_c and B_m shift toward lower magnetic field values.

Other instability mechanisms accounting for enhanced diffusion could be due to unstable wall sheaths or sound wave resonance effects. Bohm's criterion for a stable wall sheath formation is

$$v_+ \geq (kT_e/m_+)^{1/2} \quad (7)$$

where v_+ is the ion velocity perpendicular to the wall on entering the sheath.⁷ Since $v_+ \propto B^{-2}$, the velocity will decrease as the magnetic field is increased. For a sufficient magnetic field strength, Eq. (7) will not hold and the wall sheath will become unstable.¹¹

Further theoretical investigations of the instability in the positive column in a longitudinal magnetic field were carried out by Kadomtsev and Nedospasov.¹² They showed that a screw-shaped disturbance in the plasma column was responsible for the observed phenomenon. Experimental results summarized

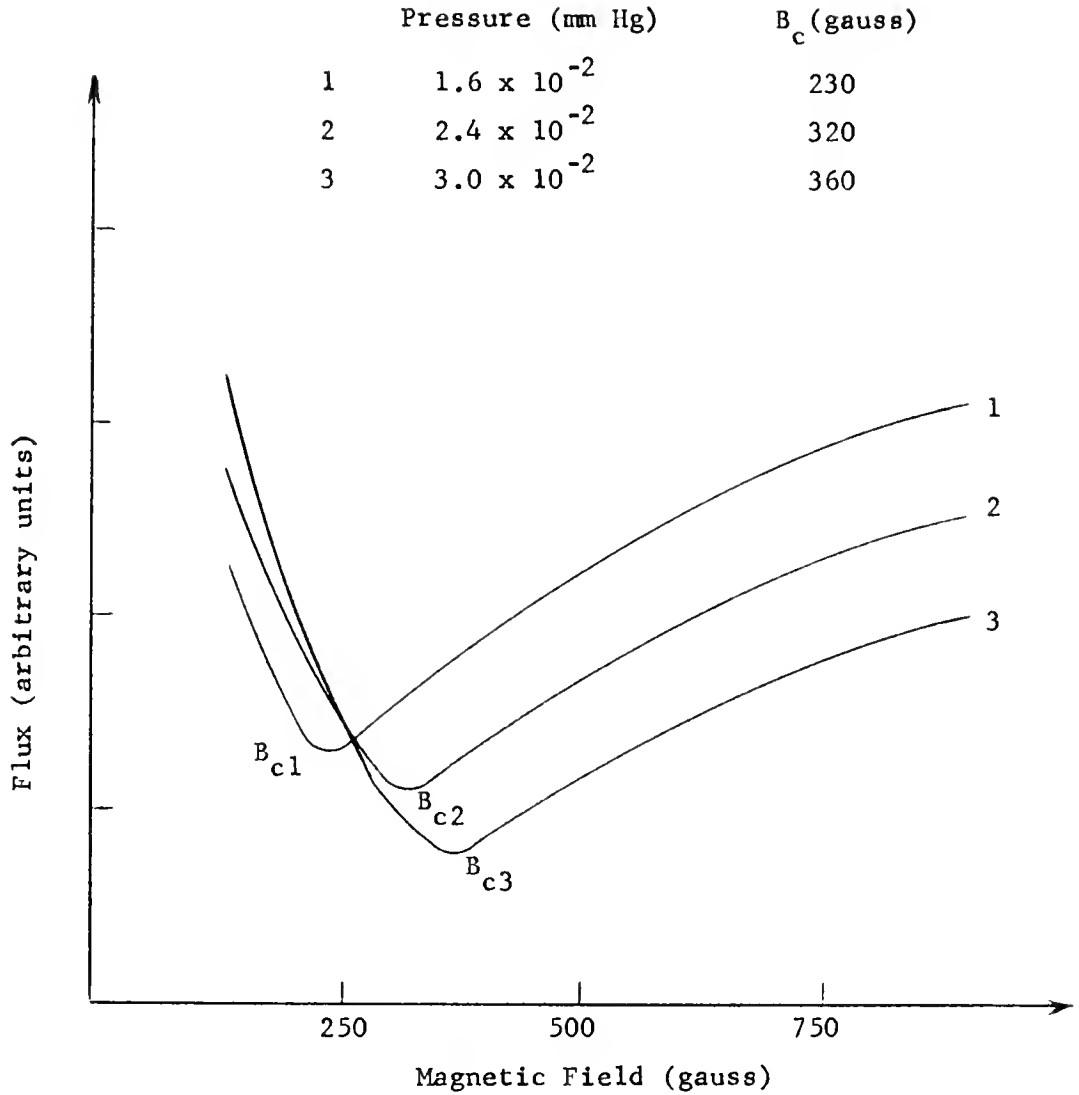


Fig. 2. Escape flux of ions transversally to the magnetic field from a cold-cathode P.I.G. discharge working with hydrogen. The discharge length is 110 mm, diameter 30 mm, voltage drop 400 volts and current 200 ma.

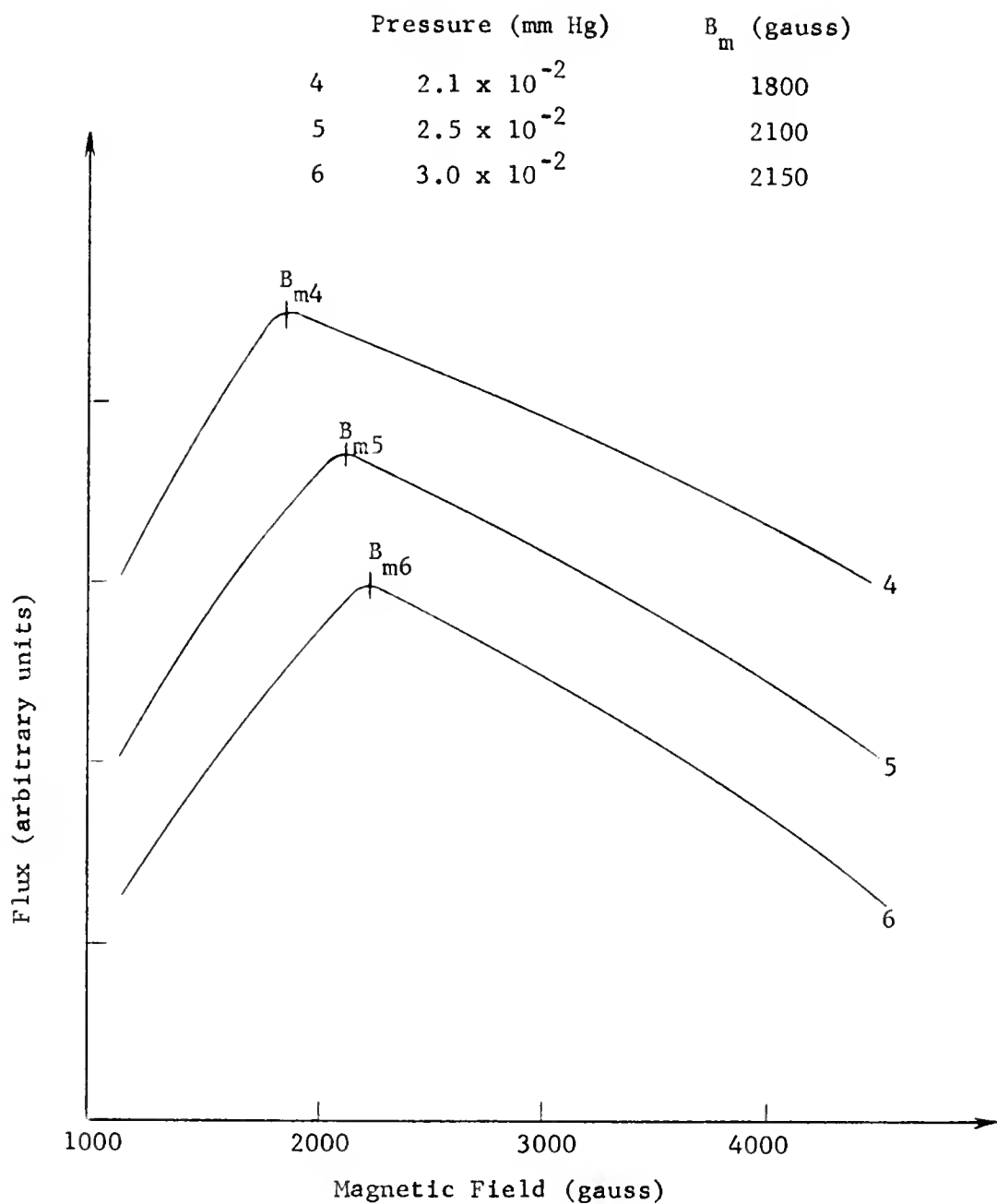


Fig. 3. Escape flux of ions transversally to the magnetic field for $B > 1000$ gauss.

in Fig. 4 have shown that it is indeed the screw-shaped disturbance rather than the wall sheath instability that is responsible for enhanced diffusion.¹³ Due to the importance of the screw instability, an outline of the theory and a physical description of the mechanisms involved will be given below.^{14, 15}

The plasma density of a cylindrical positive column in a magnetic field is given by

$$n_o(r) = N_o J_o(\alpha_o r/R) \quad \alpha_o \approx 2.405 \quad (8)$$

where r denotes the radial distance from the cylinder axis, N_o is the plasma density on the axis, J_o is the Bessel function of zero order, and R is the tube radius.¹⁶ The radial ambipolar electric field is

$$E_o(r) = - (\Phi_o/n_o)(dn_o/dr) \quad (9)$$

where
$$\Phi = (D_{- \perp} - D_{+ \perp}) / (b_{- \perp} + b_{+ \perp})$$

$$\begin{aligned} D_{- \perp} &= D_- / (1 + \omega_-^2 \tau_-^2) & b_{- \perp} &= b_- / (1 + \omega_-^2 \tau_-^2) \\ D_{+ \perp} &= D_+ / (1 + \omega_+^2 \tau_+^2) & b_{+ \perp} &= b_+ / (1 + \omega_+^2 \tau_+^2) \\ D_- &= b_- kT_- / e & D_+ &= b_+ kT_+ / e \end{aligned} \quad (10)$$

where D_- is the diffusion coefficient, b_- is the mobility, ω_- the gyrofrequency, τ_- the collision time with neutrals, and

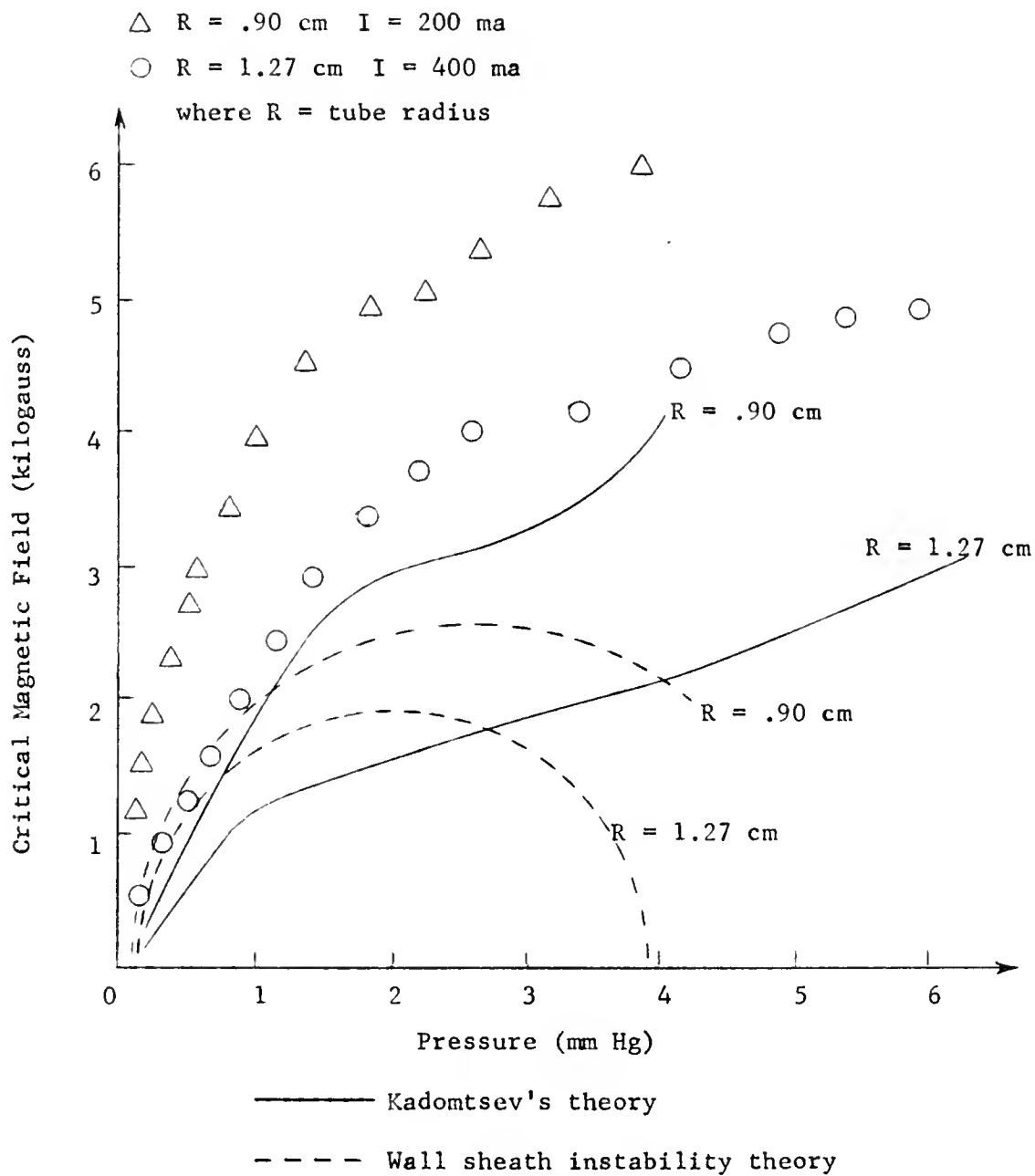


Fig. 4. The critical magnetic field is plotted as a function of the pressure.

T_- the electron temperature.^{14, 17} The same notation with subscript + is used for the ions, where k is the Boltzmann constant and e is the charge. It is assumed that the collision frequency of the ions is much larger than their gyrofrequency in the positive column. The production rate of electrons and ions in the positive column is¹⁶

$$Z = D_a (\alpha_o/R)^2 \quad (11)$$

where $D_a = (D_{-1} b_{+1} + D_{+1} b_{-1}) / (b_{-1} + b_{+1})$.

The left-handed screw-shaped density perturbation n' which is originally quasi-neutral, is superimposed on the steady-state density distribution from Eq. (8), where

$$n' = n_1(r) \cos(m\theta + kz) . \quad (12)$$

In this notation, $n_1(r)$ denotes the radial variation of the perturbed density, θ the azimuthal angle, z the distance along the axis, and k the wave number. Since the temperature and mobility of the ions are considerably less than those of the electrons, it is assumed that the rate of growth and dissipation of the ion part of the screw are small in comparison with those of the electron screw.

A perturbed space charge ρ' , given by Eq. (13), will arise when the electron screw is given a small angular displacement δ relative to the ion screw in the positive θ direction.

$$\begin{aligned}\rho' &= en_1(r) \left[\cos(m\theta + kz) - \cos(m\theta + kz - \delta) \right] \\ &\approx -e\delta n_1(r) \sin(m\theta + kz)\end{aligned}\quad (13)$$

It can be seen in Fig. 5 that ρ' produces an azimuthal electric field E'_θ . The subsequent E'_θ/B_z drift feeds electrons from the main density distribution $n_o(r)$ into the screw perturbation.

When the net gain of electrons averaged over the screw ($\pi/2 > \theta > -\pi/2$ in Fig. 6) is larger than the losses, the electron screw will grow, i. e. when

$$\begin{aligned}-\frac{E'_\theta}{B} \frac{\partial n_o}{\partial r} &\cong \left[-\frac{\partial}{\partial z} \left(D \frac{\partial n_1}{\partial z} \right) - \frac{1}{r} \frac{\partial}{\partial \theta} \left(\frac{D_{\perp}}{r} \frac{\partial n'}{\partial \theta} \right) \right. \\ &\quad \left. - \frac{1}{r} \frac{\partial}{\partial r} \left(r D_{\perp} \frac{\partial n'}{\partial r} \right) - \frac{1}{r} \frac{\partial}{\partial r} (r n' b_{\perp} E_{or}) - z n' \right].\end{aligned}\quad (14)$$

The first three terms on the right side of Eq. (14) represent electron losses in the screw due to diffusion along and perpendicular to the magnetic field. The fourth term represents conduction losses in the unperturbed ambipolar field while the last term gives the rate of electron production.

From the field quantities given in Fig. 5, it can be seen that E_{oz} tends to "lift up" the electron screw relative to the

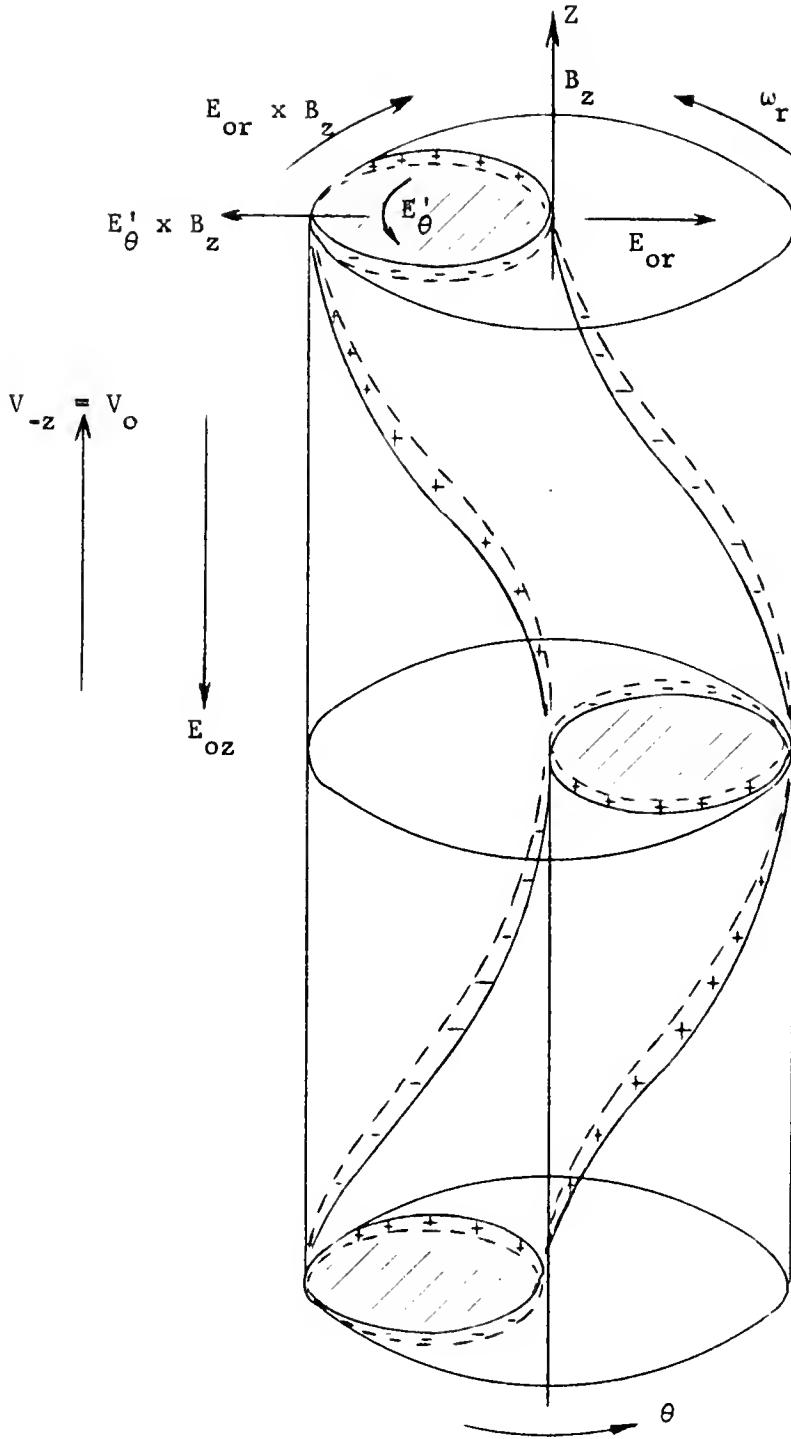


Fig. 5. Left-handed screw instability for $m = 1$. The perturbed density distribution of ions is given by the body confined by the full lines. The corresponding electron distribution is indicated by the dashed lines.

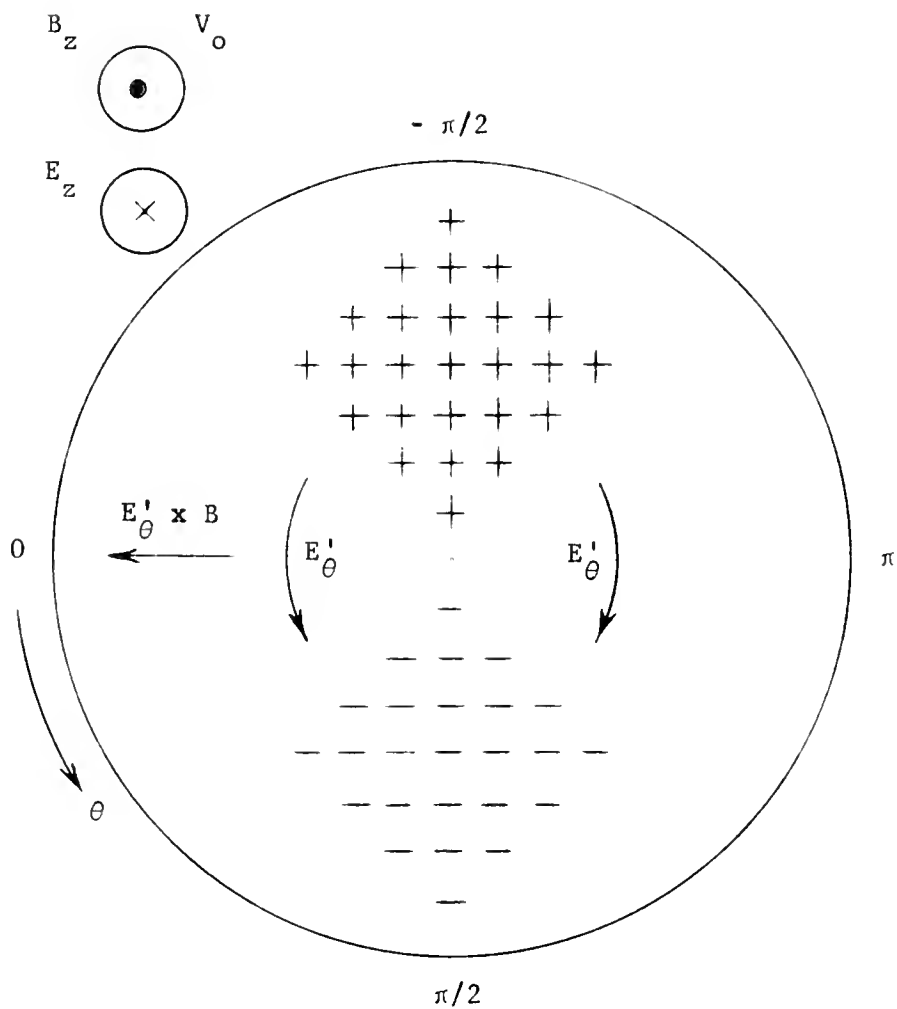


Fig. 6. A cross sectional view of the upper part of Fig. 5. This shows a more realistic charge distribution and the outward $E'_\theta \times B_z$ drift which is responsible for instability.

ion screw. This is equivalent to a rotation in the positive θ direction of the electron screw. The charge separation in a given plane produces the azimuthal electric field E'_θ . Note that the initial destabilizing mechanism is induced by the axial electric field. The ambipolar electric field, however, tends to cause the electron screw to rotate in the negative θ direction relative to the ion screw. When this negative rotation plus the stabilizing diffusion and conduction effects balance the rotation in the positive θ direction, the particle distribution will become steady with electrons moving in screw-shaped paths inside the ion screw. This balance takes place at the critical magnetic field B_c .

Other work has been done in which rotational instabilities were observed. Perkins and Post found that the plasma rotated eccentrically as one body while escaping radially across the magnetic field lines when instabilities occurred in their hot electron and hot ion plasmas.¹⁸

Simon and Guest investigated the screw-type instability in perhaps a more realistic manner.¹⁹ Instead of requiring an external longitudinal electric field to initiate the spiral behaviour, they assumed the direct streaming of ions and electrons out of the plasma to the end walls provided the mechanism. Although ambipolar fields tend to balance the ion and electron

currents, exact cancellation does not occur. This seems reasonable since ions diffuse more rapidly in the directions perpendicular to the magnetic field. Thus, there is net current flow along the axis and a helical perturbation may be unstable. Another important feature of their work is the differentiation between the phenomena taking place in the positive column and that which takes place in the low pressure region outside of the main discharge. Kadomtsev and Nedospasov considered only the positive column region where the ion collision frequency was greater than the ion gyrofrequency. Thus $\omega_+ \tau_+ < 1$ indicating that the magnetic field acts only on the electrons, where ω_+ is the ion cyclotron frequency and τ_+ the ion collision time. In the low pressure region ($p_0 \approx 10^{-3}$ mm), $\omega_+ \tau_+$ and $\omega_- \tau_-$ are both greater than 1, so that the magnetic field influences both types of particles. The particle conservation equations are also different for both regions. In the low pressure case ions are produced only along the axis of the discharge while in the positive column, continuous ionization of the neutral gas is always going on. For low pressure conditions, Guest and Simon found that the frequency of rotation ω_k , to the first approximation, is independent of B and is given by

$$\omega_k = (\pi V_+ / 4d) (1 + T_- / T_+) \quad (15)$$

where d is the discharge length, and V_+ is the average particle velocity to the end walls. From experimental considerations, this model indicated a rotation frequency of 25 kc, in good agreement with the measured values. The rotation frequency dependence on the discharge length for constant pressure and magnetic field was measured.²⁰ The low pressure conditions were satisfied by injecting a beam from a duoplasmatron ion source into background gases of hydrogen, helium, and nitrogen at pressures from 0.05 to 2 μ . The discharge length d was varied continuously from 10 to 110 cm. Frequency measurements showed the inverse wall separation dependence from $d = 12$ to $d = 18$ cm. For larger d , however, irregularities or other types of oscillations occurred.

A "three fluid" model has been used to predict diffusion processes and turbulence in weakly ionized plasmas in a Penning discharge.²¹ As shown in Fig. 7, the plasma column has a radial electric field E_r due to the Penning discharge geometry and is immersed in an axial magnetic field B . An azimuthal perturbation applied to the axisymmetric plasma allows the electrons to drift in the θ direction with a velocity $v_\theta = E_r/B$. The neutrals, acting as a third fluid, exert a larger frictional drag on the ions than they do on the electrons. Thus the ion perturbation lags behind the electrons setting up an E_θ field. The $E_\theta \times B$

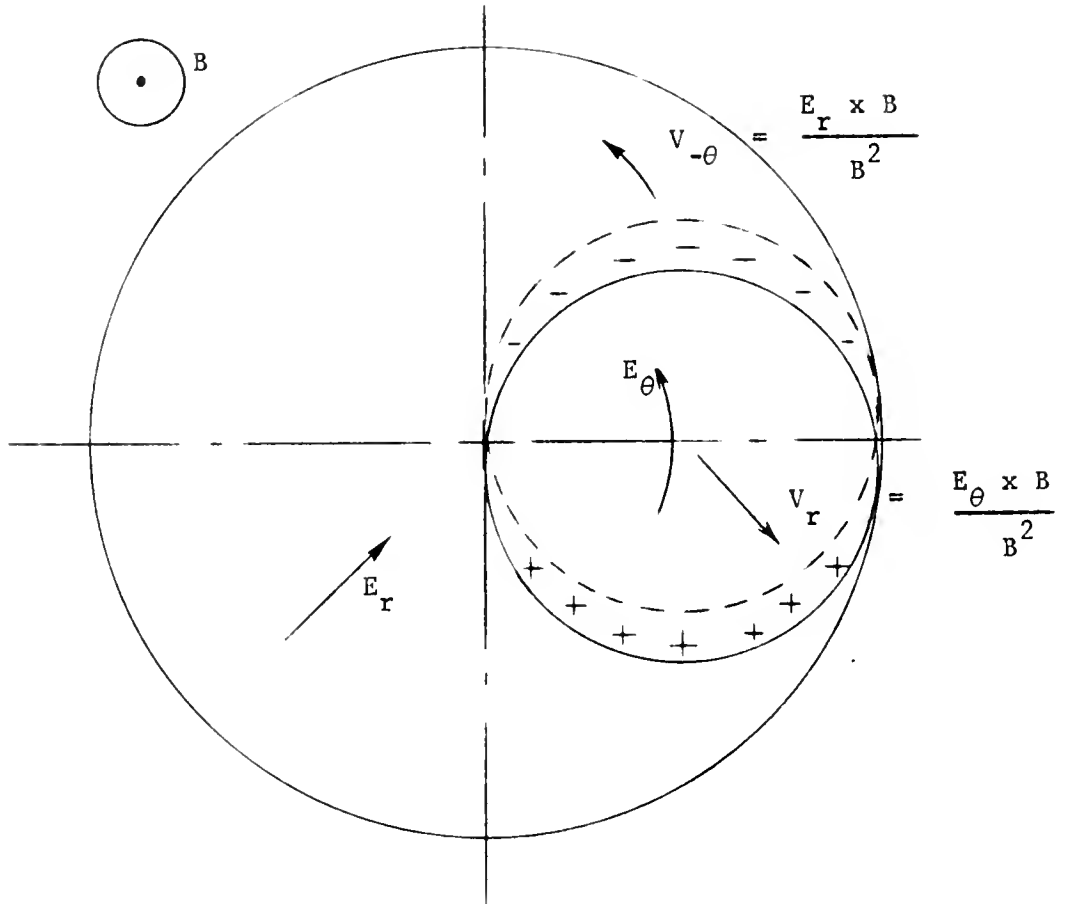


Fig. 7. A cross section of the Penning discharge with the charge distribution and resultant drifts.

drift drives the plasma outward and amplifies the perturbation. This differs from the screw instability in that a radial electric field, rather than an axial electric field, drives the perturbation. The dissipative effects also allow a smooth transition to the unstable mode in contrast to the sharp onset of the screw instability. This model is in good agreement with critical magnetic fields found experimentally in a reflex discharge by other workers.

Chen and Cooper found that the longitudinal wavelength of the measured oscillations in a reflex discharge were much too long to be associated with ion waves.²² From measured wavelengths, they calculated a wave velocity of the order of 2×10^7 cm/sec which is much smaller than the Alfvén velocity ($\sim 10^9$ cm/sec) and much larger than the acoustic velocity ($\sim 10^6$ cm/sec). The dispersion relation obtained from the "three fluid" model does, however, give results for the critical magnetic field which agree with the measured Chen and Cooper values. Crawford attempted to explain this phenomenon by a radial electrostatic sound wave mechanism but he noted that an azimuthally varying mode was strongly excited and easily detected.²³

Alexeff and Neidigh have carried out extensive experimental studies on the ionic sound waves in plasmas predicted by Tonks and Langmuir.^{24, 25} The sound waves were found in both a

magnetically supported plasma column formed by a reflex discharge, and in the plasma of a spherical chamber with no B field. Resonant modes restricted the ionic sound waves to steady oscillations of discrete frequencies.

The basic equation leading to the ionic sound waves derived by Tonks and Langmuir is

$$\nu = \left[ne^2 / (\pi m_+ + ne^2 m_+ \lambda^2 / \gamma k T_-) \right]^{1/2} \quad (16)$$

where ν is the frequency in cycles/sec, n is the electron or ion density in particles/cm³, e is the electron charge in esu, m_+ is the mass of the ion in grams, λ is the ionic wavelength in cm, γ is the adiabatic compression coefficient of the electron gas, k is Boltzmann's constant in ergs/°K, and T_- is the electron temperature in °K. The plasma is assumed to be charge neutral, the ions singly ionized, and the electron temperature much higher than the ion temperature.

If only wavelengths λ much larger than the Debye cutoff length L_o are considered, where

$$L_o = (kT_- / 4\pi ne^2)^{1/2}, \quad (17)$$

$$\text{then} \quad \nu = \lambda^{-1} (\gamma k T_- / m_+)^{1/2} \quad (18)$$

where Eq. (18) is the dispersion relation for ionic sound waves.

With the assumptions that the ions and neutral gas atoms have the same mass and the coherent velocity of the ions due to the ionic sound wave motion is small compared to the thermal velocities of the ions, it can be shown that the ionic sound waves can be strongly damped out by neutral background gas. It is then possible for the lower frequency standing waves to be damped out while allowing excitation of the higher frequency waves to take place. So, at higher pressures, only higher overtones of the fundamental frequency should be observable.

Experimental verification of the ion sound wave model was attempted in a reflex discharge arc. With proper adjustments of the source parameters, pure sinusoidal wave forms were measured. The frequency was found to be independent of the magnetic field, the gas density, and the plasma supply voltage and current. However, if the filament temperature of the source was changed enough, the frequency would change discontinuously from the fundamental to the first overtone. Occasionally, overtones up to the fourth order were observed. The different plasma gases used indicated that the frequency was proportional to $m_+^{-1/2}$. It was also noted that by varying the length of the column, it was found that the frequency was approximately inversely proportional to the column length.

Since it appears that no one theory has been developed which accurately explains the phenomena observed in the different experiments, it will be the object here to compare our results presented in the fourth chapter, with the instability models discussed above.

CHAPTER III

APPARATUS AND PROCEDURE

The apparatus used in these experiments will be divided into three parts. Initially a high energy, low current hydrogen ion beam extracted from a duoplasmatron ion source was used to investigate ion beam-plasma interactions. Secondly, a hollow cathode, low energy, higher current ion source was developed to further the interaction studies. Finally, a reflex discharge of special design was developed and used to terminate the studies covered in this tract.

Dual Beam-Plasma System

Experimental work previous to this effort had investigated the passage of a single high energy ion beam through a plasma.²⁶ No strong interaction of the single beam was found within the limitations of the beam magnitudes and path lengths available. For two beams which counterstream, the interactions, if existent, should be greatly amplified by the associated mechanisms for modulation and feedback processes. Lacking two complete duoplasmatron sources, an investigation was made in the attempt to reflect a single beam from a region of positive potential. If this were found to be possible to a sufficient extent, a dual ion beam system would be achieved in a manner in which an

electron beam is often found to behave. In addition, the behaviour of an ion beam under reflection was thought to be strongly indicative of its ability to excite plasma oscillations by collective coupling. To investigate this reflection possibility, the ion beam was arranged to fall upon a suitable and versatile target after passing through a plasma in the target vicinity.

The duoplasmatron source, including the extraction and focusing electrodes was purchased as a single unit and then enclosed in a vacuum tight, cylindrical brass container. The container was insulated from the source by a 3/4-inch lucite ring as shown in Fig. 8. It was then mounted horizontally on a steel and aluminum frame. A sylphon bellows was attached to the orifice of the lens system to allow for mechanical adjustment. A valve was inserted between the bellows and the rest of the system. With the valve closed, pressure was maintained at 10^{-6} mm Hg in the source by a N. R. C. type HS6 oil diffusion pump with a pumping speed of 1500 liters/sec. This pump was mounted in a brass container directly below the Einzel lens. Thus work could be done on the rest of the system without disturbing the high vacuum in the source. Two 4-inch-diameter Pyrex crosses, connected by a 1/4-inch-diameter, water-cooled, brass, beam defining aperture, were mounted in series next to the valve. A C. V. C. type MCF 700 diffusion pump with a pumping speed of 500 liters/sec was

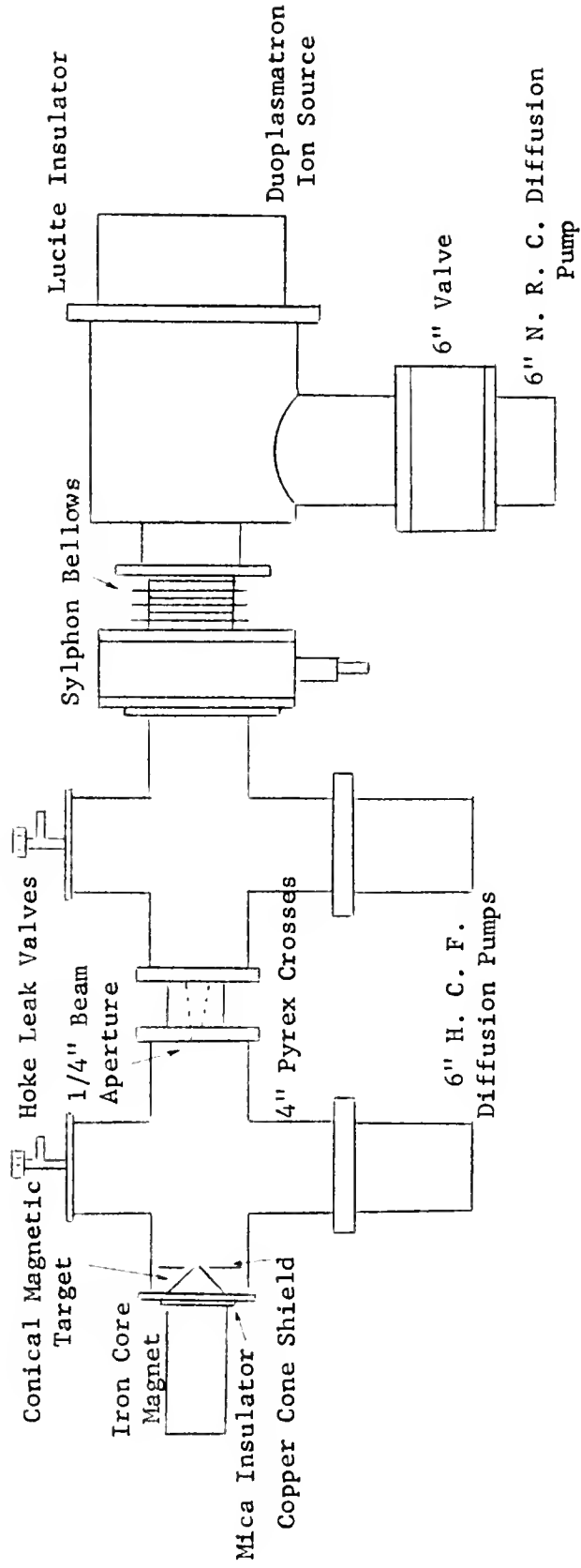


Fig. 8. High energy dual beam experimental apparatus.

mounted on the bottom of each cross and a conducting plate with a Hoke leak valve was mounted on the top of each cross. A 45° conical pole piece, silver-soldered into the brass end plate, was used as the beam target.

A thin mica disk insulated the conical pole piece target from the wire-wound iron core magnet, allowing this end plate structure to float in potential. The magnetic field strength of the target was measured as a function of the distance along the conical axis with a Radio Frequency Hall Probe Gaussmeter. The field characteristics are shown in Fig. 9. The strongly divergent magnetic field obtained with this target geometry gave rise to the required transverse component of the magnetic field. A copper disk with a 1/8-inch-diameter hole in its center and electrically insulated from all other components was placed in front of the cone tip. A vacuum tube voltmeter was used to measure the potential build-up between the pole piece and ground.

The power supplies required to run the source, extract and focus the beam, and to reflect the beam are summarized in Table 1.

Before the source was started, the Einzel lens was "conditioned" by slowly raising the extraction voltage to 45 keV. Threaded nylon bolts were used to hold the brass container and lucite insulator ring to the source. Even with the threaded lucite, breakdown occurred through some of the bolts. After

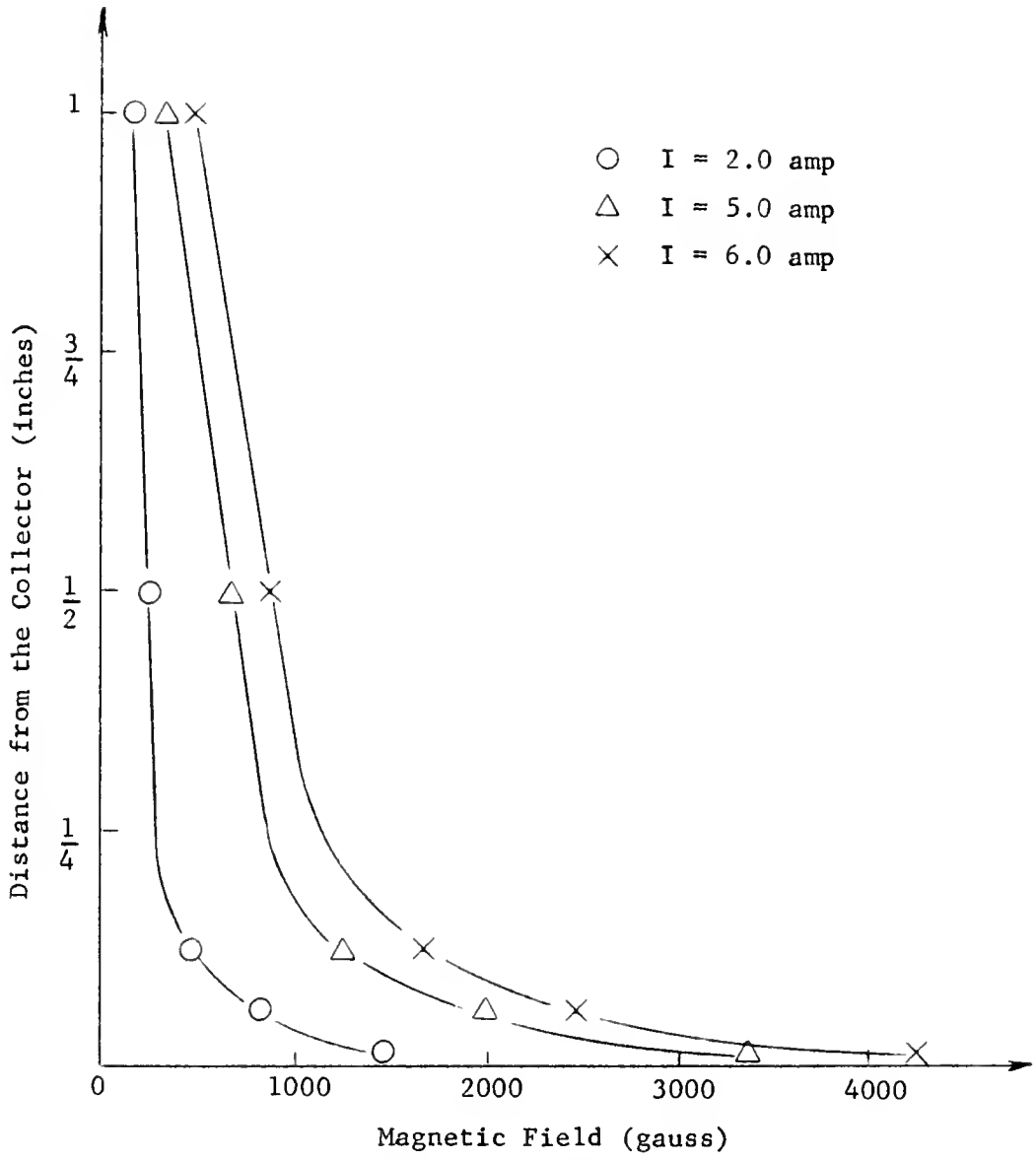


Fig. 9. Magnetic field strength along the axis of the cone is plotted as a function of the distance from the cone tip. Three different values of magnet current are used.

TABLE I

Power Supplies for Source Operation

Arc (current regulated)	450 volt	5 amp
Source magnet	150 volt	10 amp
Filament	6 volt	100 amp
Palladium leak	7.5 volt	30 amp
Extraction focus		
Extraction	50 kV	50 ma
Focus	10 kV	25 ma
Reflection magnet	150 volt	10 amp

trying various cleaning methods, it was found that the breakdown could be stopped by dipping the bolts in corona "dope" and then bolting the container and lucite ring to the source. A 250-watt string of resistors allowed 1 ma to drain to ground at 10 kV, eliminating most of the corona losses and stabilizing the high voltage source.

The standard procedure for operating the duoplasmatron ion source is as follows. The palladium leak was first turned on, bringing the source pressure up to a desired pressure. The current to the source magnet was then set at 2 amps. The filament current was adjusted to approximately 22 amps, and the arc was then ignited. Before extraction, the source magnet current was

generally set back to approximately 1 amp, since this gave the best results. To be certain the pressure would remain essentially constant, the arc was allowed to run for five minutes. The pressure could always be adjusted by varying the current in the palladium leak or by varying the filament current. Increasing the filament current lowered the pressure and increasing the palladium leak current increased the pressure. The focus potential was then set at 3 kV. Finally, the beam was extracted by raising the accelerating voltage to 10 to 20 kV. The beam was easily seen in a darkened room and optical focusing was readily attained by adjustment of the focus potential and the source magnet current.

During a typical run, the source, accelerating and focusing characteristics were kept constant. Normally, the source pressure remained constant without adjustment; for some runs, however, the palladium leak current and/or the filament current had to be changed to keep this pressure constant.

When steady beam conditions were realized, gas was emitted through the leak valve into the target region at a rate set to establish a given background pressure. The potential build-up on the pole piece and the interaction frequencies were then measured as a function of the magnetic field in the collector region. These measurements were repeated for different

background pressures, beam energies, and plasma gases and are discussed in the next chapter.

High Current Source System

One limitation of the collective behaviour of the high energy beam is associated with the limited beam current. Higher beam currents of appreciable amounts have not been possible from any known sources from which ions are accelerated. The major factor in this limitation is associated with space charge arising from charge separation. However, there appeared the possibility of using, as a source, ions from a long cylindrical arc operating in the magnetic field. From such a source both the ions and electrons diffuse radially from the main column. The ions are accelerated toward the cathode by the arc operating voltage. They then have the possibility of forming an intense beam if they do not strike the cathode or a support of the cathode. At the same time limitations found on the arc potentials, for the arc geometry reasonably available, have restricted the beam to low potentials; but this is of little interest toward interacting possibilities. In principle, large beams and energetic beams could likely be achieved. The limitations of such a source would depend upon the diffusion rate and not space charge. Moreover,

there appeared the possibility of pulsing this arc to obtain a high energy beam, again without a space charge limitation.

At this stage, however, it was appreciated that the ion stream alone does not seem to be capable of collective interaction in the presence of low temperature thermal electrons. The dual beam interacting aspects for two such simple, intense ion sources were not therefore carried to completion. Instead, aspects of the diffusion process appear extremely important and the arc source has been studied to uncover some of these processes which are also beam interaction processes. These possibilities have been investigated and the apparatus developed is presented in this section.

The hollow cathode, low energy, high current ion source, hereafter called the high current source, is shown in Fig. 10. The high current source, focusing magnets, and collector were attached to a 4-inch-diameter Pyrex cross. The entire assembly was mounted on a steel and aluminum frame.

The anode structure initially consisted of an insulated water-cooled brass plate mounted on one arm of the Pyrex cross. On the opposite side of the cross another brass plate, floating in potential, collected the ion beam. After several trial cathode arrangements, a satisfactory water-cooled cathode structure was developed and mounted on top of the cross.

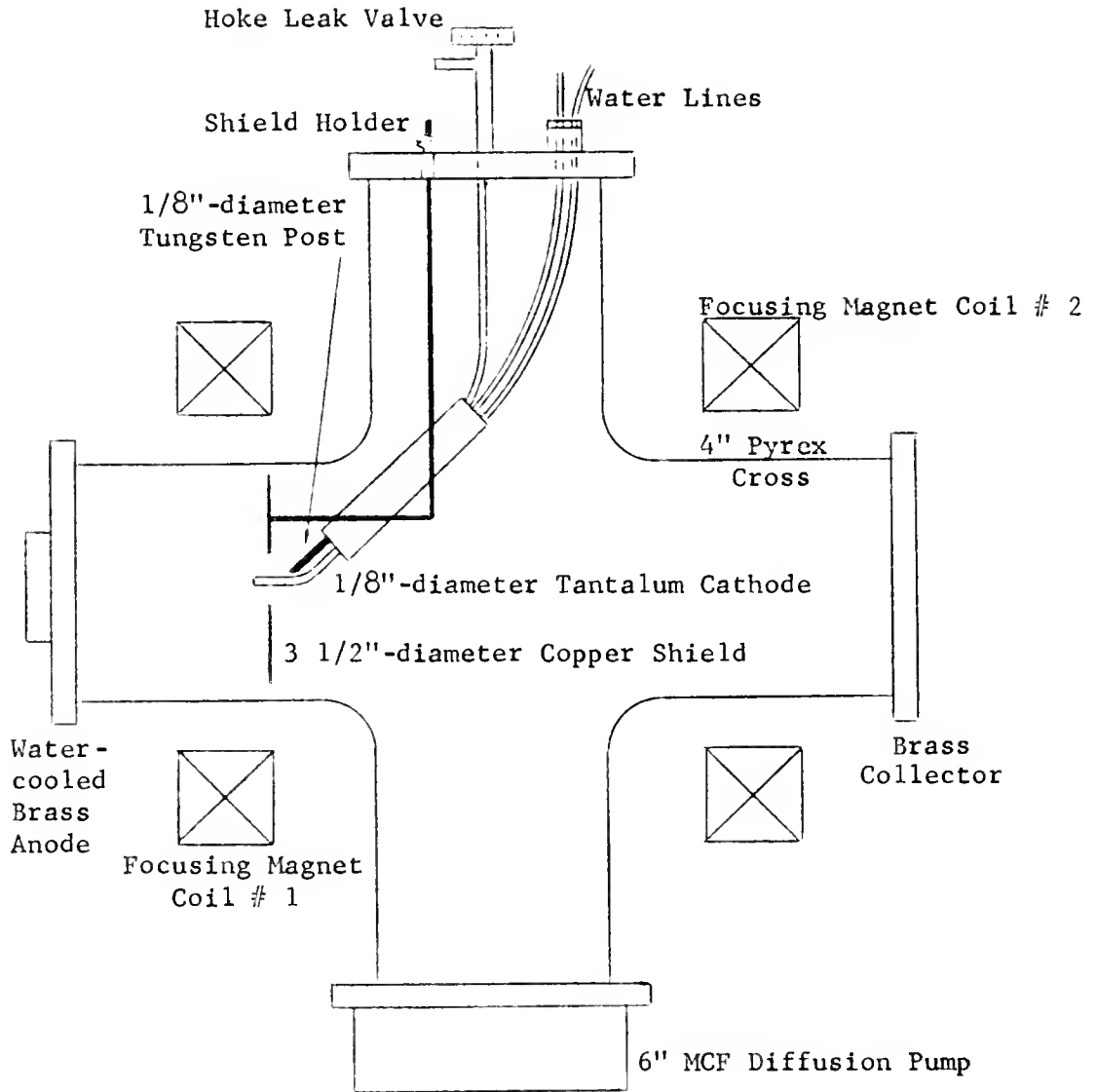


Fig. 10. High current ion source.

Details of the cathode are shown in Fig. 11. The hollow 1/8-inch-diameter tantalum tube served both as a gas feed and as the self-heated cathode. The gas flow was controlled by having a Hoke leak valve and needle valve in series with the argon tank. A section of Tygon tubing inserted between the needle valve and Hoke valve insulated the cathode from ground. A 1/8-inch-diameter tungsten post shielded the tantalum cathode at the bend and prevented cutting due to ion impact at this vulnerable point. A 3 1/2-inch-diameter copper shield disk with a 1/2 to 1-inch-diameter beam aperture was placed on the collector side of the cathode tip. This shield, which could be grounded or allowed to float, had several purposes. When grounded, the shield and grounded collector essentially defined a field free region for the beam to move in. Potentials applied to the shield gave it the properties of an accelerating electrode. The shield also reduced the tantalum sputtering to the Pyrex walls in the beam and collector regions.

The 450-volt current-regulated arc supply was connected between the cathode and anode in series with a 71-ohm surge-limiting resistor. A 30-volt - 50-amp D.C. supply powered the focusing magnets, producing a mirror-shaped field along the axis of the discharge. The spacial dependence of the field along the axis is shown in Fig. 12.

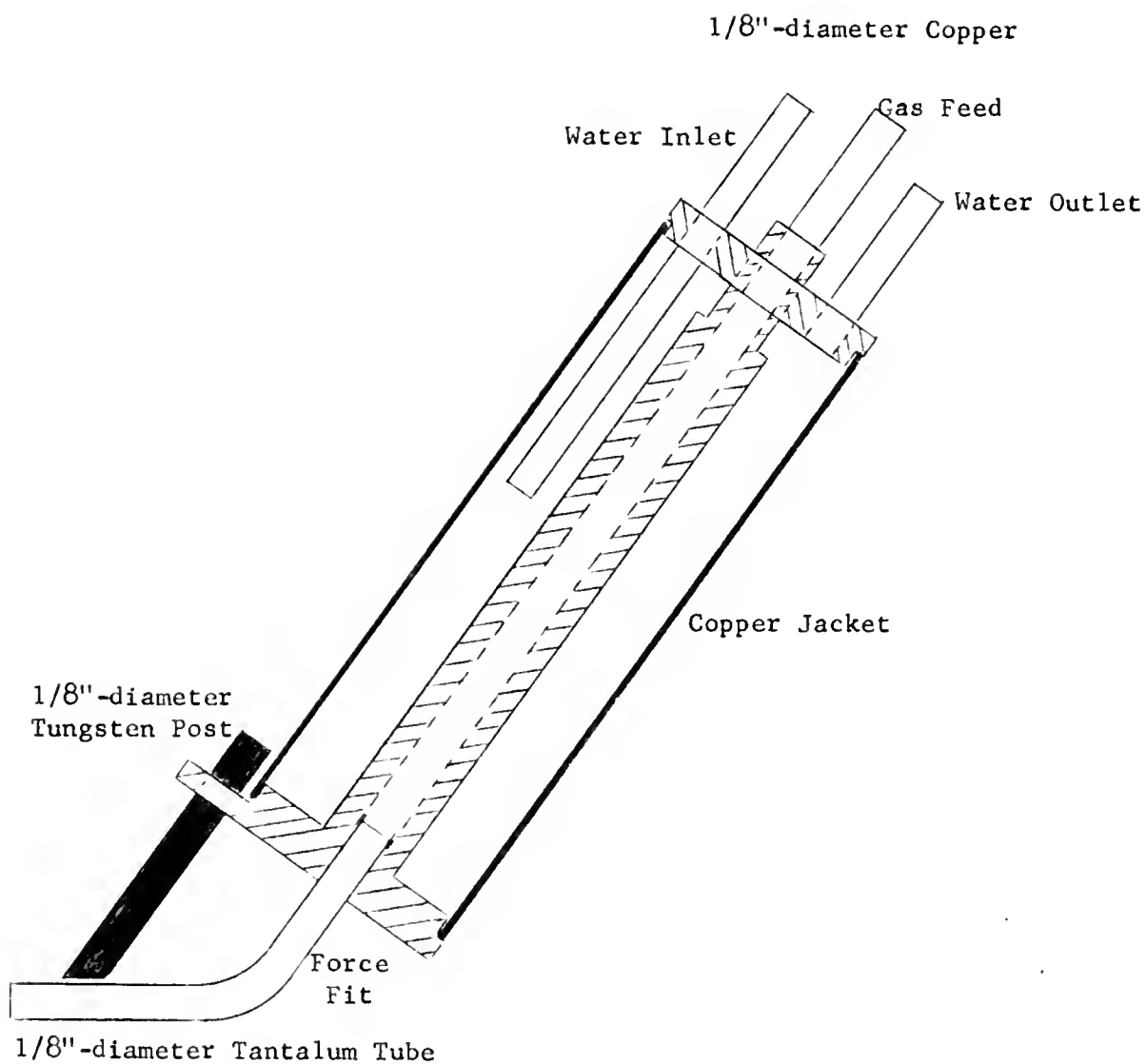


Fig. 11. Detail of the cathode of the high current source.

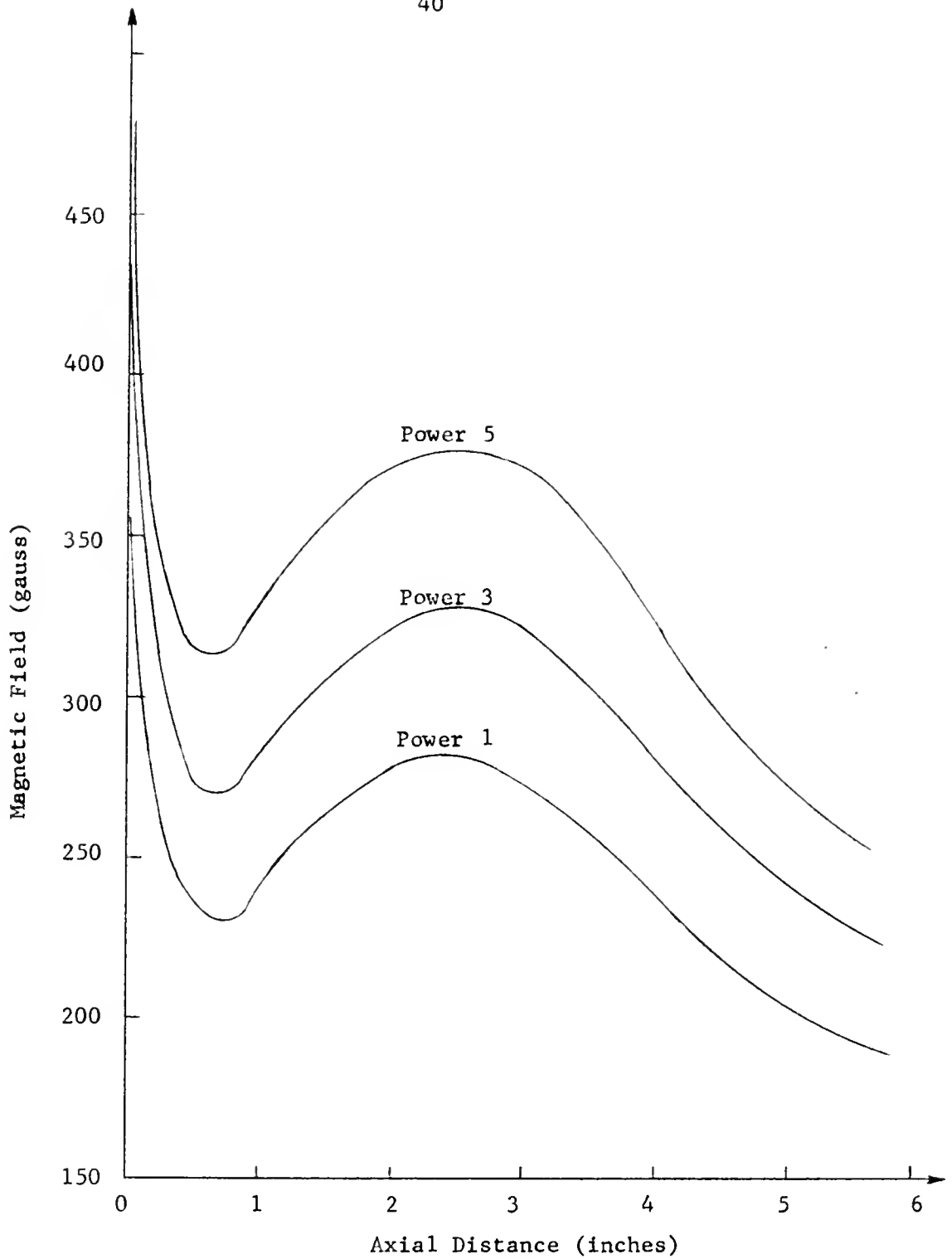


Fig. 12. The magnetic field along the arc axis is plotted as a function of the distance from the anode. Three settings on the power supply are shown.

The water-cooled magnetic anode designed to allow a more flexible magnetic field variation in the active arc column is shown in Fig. 13. A 1 1/4-inch-diameter water-cooled copper disk was hard soldered to a truncated soft iron core. The iron core, 1/8-inch-diameter water lines, and probe fixtures were soldered to the brass anode plate. A thin mica disk insulated the anode assembly from the external iron core electromagnet and rubber tubes insulated the water lines. Fig. 14 gives the radial dependence of the magnetic field on the surface of the anode.

The 9 pin header allowed potential measurements at five different radial positions along the surface of the anode. A variable probe allowed potential measurements from the center of the arc to the Pyrex walls and from the anode surface to the cathode. The variable probe consisted of a 40-mil tungsten wire epoxied into a 5/16-inch-diameter capillary tube. The tube and wire were bent at 90° so that the external rotation of the probe allowed a complete radial sweep of the arc region. An O-ring sleeve fitting maintained the high vacuum when the probe was adjusted.

The equipment used in the three methods of pulsing the arc is described below. First a two-section artificial transmission line matched roughly with the characteristic arc

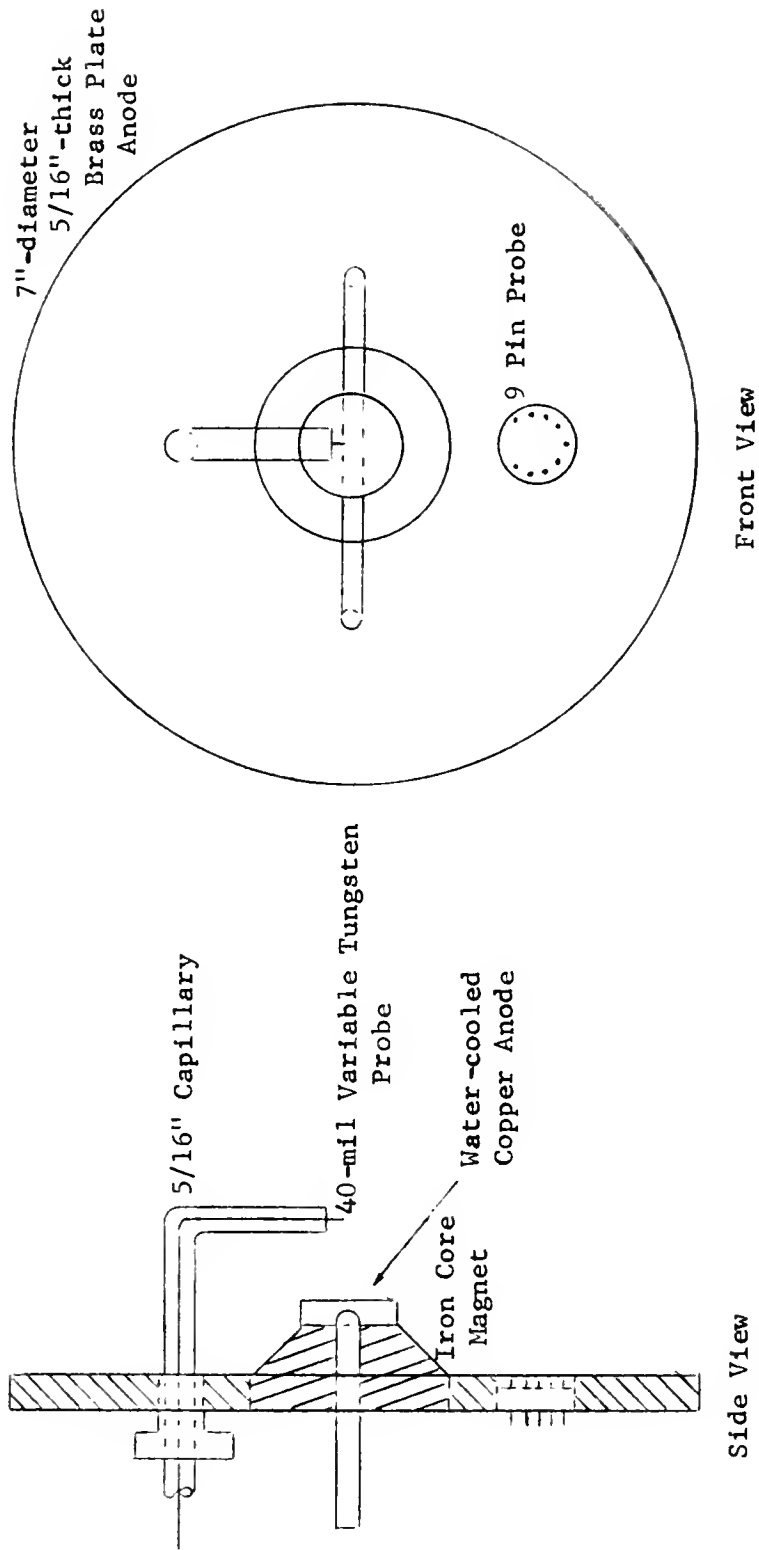


Fig. 13. Side and front view of the water-cooled magnetic anode.

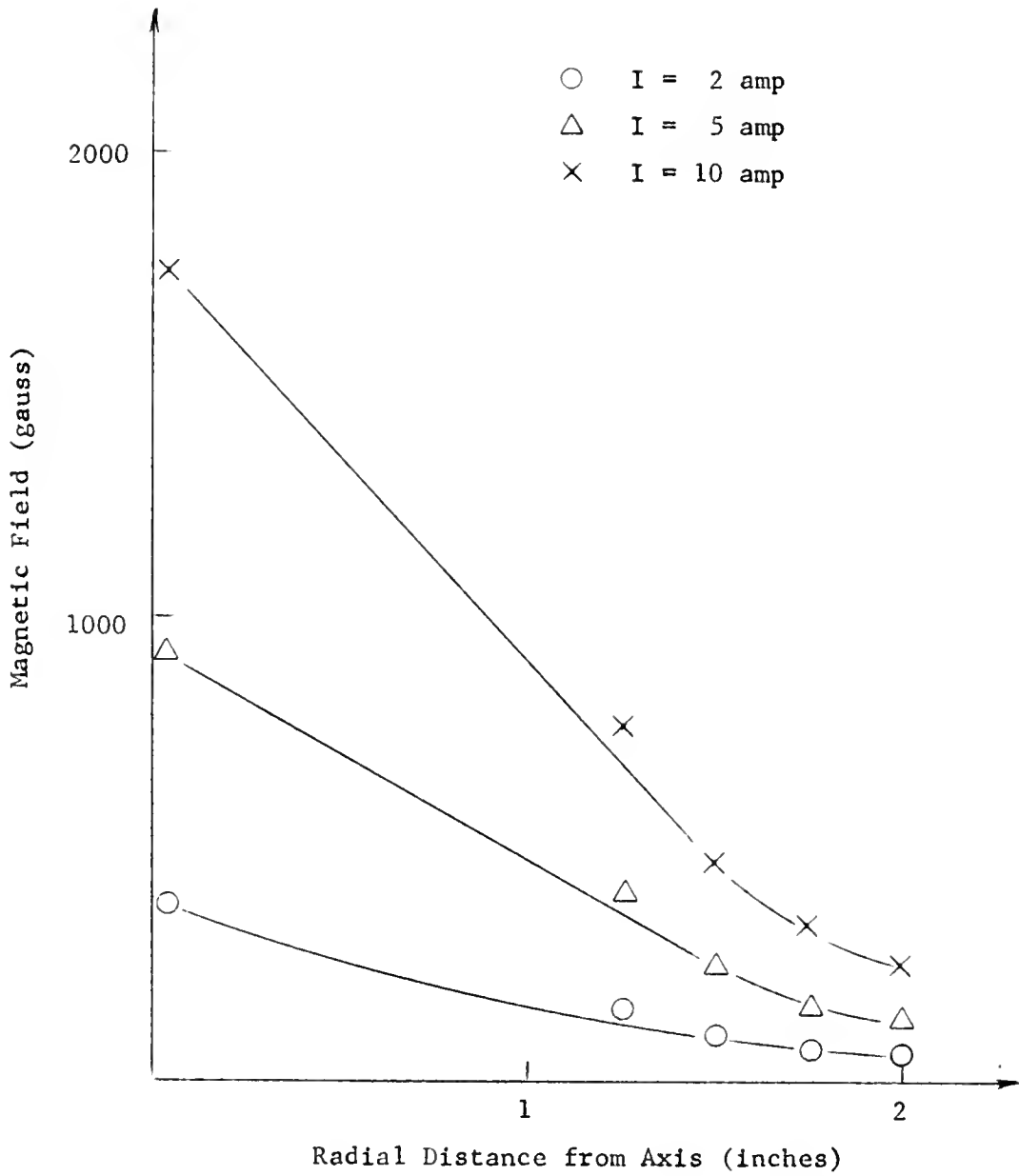


Fig. 14. Radial dependence of the magnetic field on the surface of the anode is plotted for three different magnet currents.

impedance was used to apply an over-voltage to the anode of the arc for 60 microseconds. Each section of the line consisted of a .46-millihenry inductor and a .5-microfarad capacitor. The capacitors in the circuit in Fig. 15 were charged with a Model 30-5-1 Del Electronics power supply. The magnitude of the pulse was governed by setting the spark gap at different values. The effects of the pulse on the beam current were obtained by monitoring the voltage drop across a variable resistor between the collector and ground with a Tektronix Model 517 CRO. .

A variation of pulsing the arc potential is shown in Fig. 16. Two insulated copper disks with 1-inch-diameter holes were mounted next to the anode. The pulse circuit was then connected to the outer disk with the inner disk shielding the anode. The pulse circuit, arc circuit, and beam monitoring were the same as above.

The circuit in Fig. 17 was used to provide a current pulse to the arc. The pulse circuit used the same power supply and spark gap arrangement as above. A 1-microfarad capacitor, 1000-ohm resistor, and the spark gap were connected in series with the arc. A 12-ohm resistor attached at the cathode was also tied in series with the pulse circuit. The 517 CRO was used to measure the potential drop across this resistor and across the variable resistor between the collector and ground.

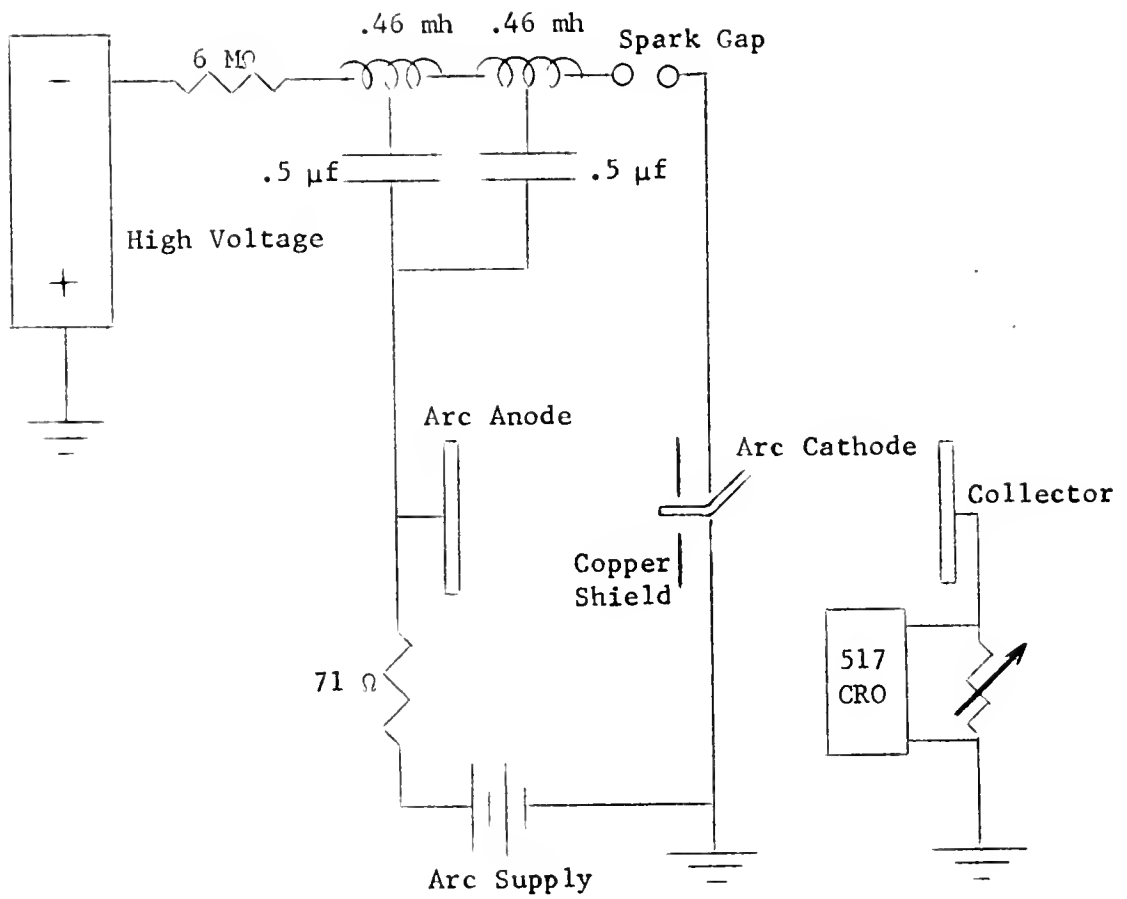


Fig. 15. Diagram of the pulse circuit and the arc.

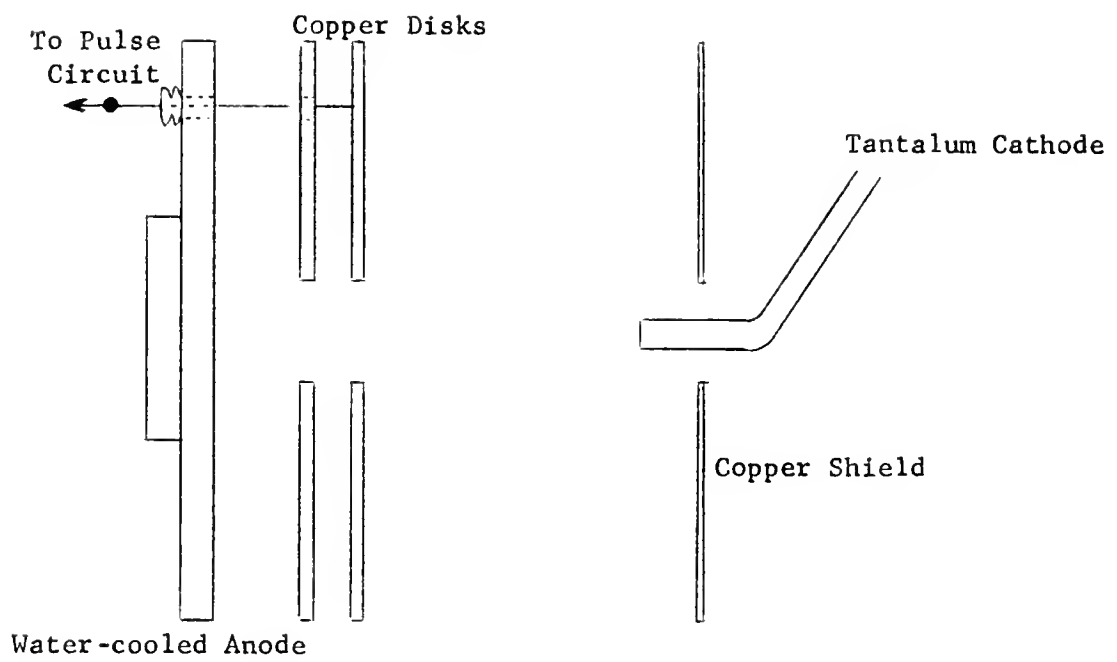


Fig. 16. Disk pulsing arrangement.

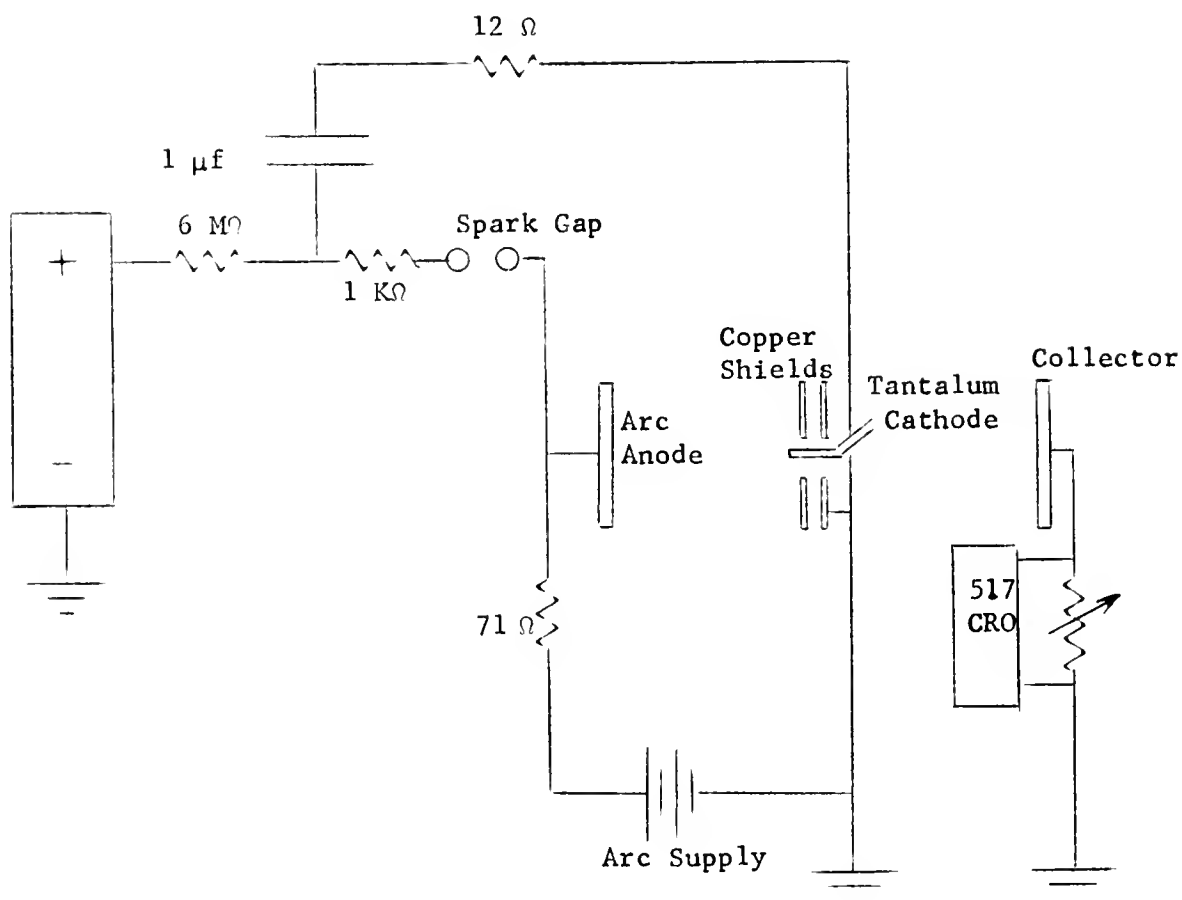


Fig. 17. Diagram of the current pulse circuit and the arc.

A 3 1/2-inch-diameter copper disk was placed behind the original shield surrounding the cathode. This second disk was grounded while the original shield was allowed to float. A Faraday Cup arrangement was periodically used in place of the collector to check for secondary emission.

The standard procedure for operating the high current source is as follows. A base pressure of 10^{-6} mm Hg or less generally indicated no leak problems. The water for cooling the electrodes was turned on and a check against electrical shorts was made. The argon gas pressure was increased to approximately 1 atmosphere and the magnetic field was turned on. The current-regulated arc supply was then adjusted until a glow discharge ran between the anode and tantalum cathode. When the tantalum turned red hot, the power was increased until the arc was struck. The arc current was generally set at 1.0 amp and the pressure reduced by adjusting the leak valves to the .1 micron-range.

During a typical run, the above procedure was followed with minor adjustments made depending on the electrode structure. For the initial set-up shown in Fig. 10, the collected steady ion beam current was measured as a function of the collector potential by using a Lambda Electronics Corporation Model 71 current-regulated supply. These measurements were repeated for different pressures, arc currents, and disk-hole diameters.

No changes were necessary in the arc striking procedure when the magnetic anode was inserted in place of the flat plate anode. For constant arc conditions, the potential on the variable probe and on the anode probes was measured as a function of the magnetic field. The collector current, variable probe current, and probe oscillations were also measured as a function of the magnetic field. The field was adjusted by varying the current to the anode magnet and by changing the polarity of the focusing magnets as well as the current. The oscillations were observed with either a Tektronix Model 517 or with a Tektronix Model 545 CRO. The measurements were then repeated for different arc currents and pressures.

The arc striking procedures were again the same as described above when the pulsing circuits were incorporated into the experiment. For the circuit shown in Fig. 15, a voltage pulse was applied directly to the arc. The pulse voltage in Fig. 16 was applied to the region immediately surrounding the discharge. Fig. 17 shows the circuit used to provide a current pulse to the arc. The pulse effects on the collector current were observed by noting the potential drop across a variable resistor between the collector and ground. These measurements were repeated for various pulse voltages, arc currents, and pressures; and oscillograms were recorded with a Wollensak 75 mm scope camera.

Reflex Arc Discharge Assembly

A number of observations on the beam collected from the high current ion source indicated that oscillatory behaviour of the arc was very likely associated with the diffusion rate. The source was therefore re-designed to provide the highly oscillatory reflex mode of the arc. It was also designed to allow mechanical facility for adjustment in all dimensions in order to determine if such adjustment was related to resonant modes of oscillation excited by beam-plasma interaction within the arc column.

The reflex discharge set up by changing the anode and cathode structures of the high current source, is shown in Fig. 18. The vacuum chamber, magnetic focusing coils, and power supplies were unchanged. The water-cooled anode-button arrangement was mounted on one arm of the Pyrex cross while the adjustable cathode was placed on the opposite arm of the cross. The vacuum chamber was again evacuated from the bottom by a 500 liter/sec diffusion pump, while the top of the cross was covered with an aluminum plate. A 4-inch section of 1/8-inch-diameter tantalum tubing was sealed to a hollow 5/16-inch-diameter brass rod. The cathode assembly could be varied longitudinally through the O-ring vacuum seal in the cathode plate. Water-cooled copper reflex buttons, 1/8-inch thick and of

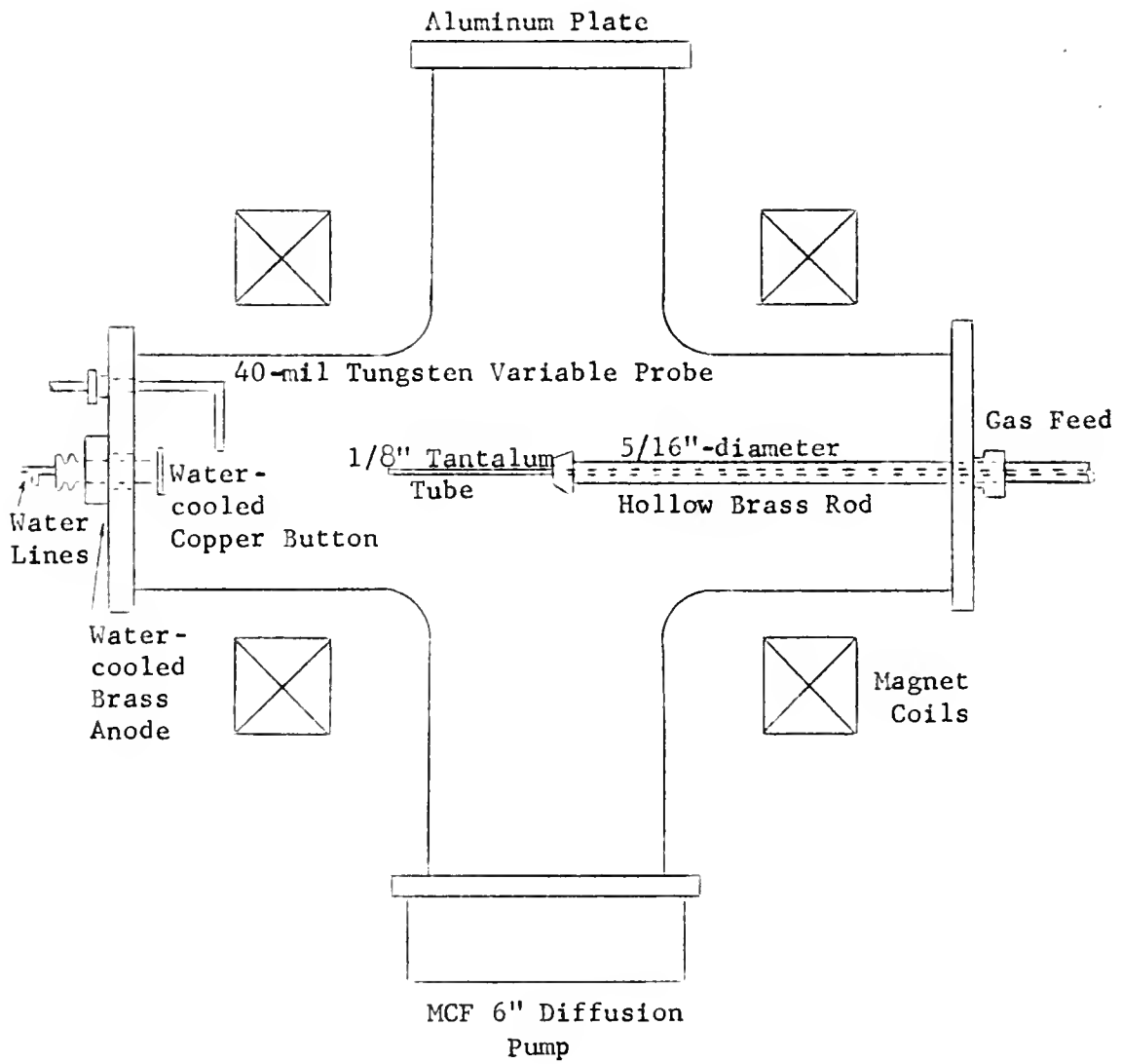


Fig. 18. Reflex arc discharge apparatus.

varying diameters, were positioned $3/8$ inch in front of the brass anode plate. Figures 19 and 20 show the details of the reflex discharge electrodes.

Operating procedures for the reflex discharge are identical to those of the high current source except for one point. It was found that the arc struck easier when the anode and button were electrically tied together. Once the arc struck, the button and cathode were generally grounded while the anode carried the high voltage. It should be noted that the discharge would not operate at low pressure whenever a hole was burned into the wall of the tantalum cathode.

During a typical run with a fixed button assembly, the pressure was set by carefully adjusting the tank valve and the two needle valves. For a given arc current and anode-cathode separation, the arc potential and oscillations measured with a Tektronix 545 CRO could be picked up on the variable probe or on any of the ungrounded electrodes. With the pressure and electrode separation remaining the same, the arc current was changed and the magnetic field dependence of the arc potential and oscillations were measured again. The electrode separation was then changed and the above procedure repeated. Finally, the pressure was changed by adjusting the needle valves and the whole experiment was repeated. The button diameter was then

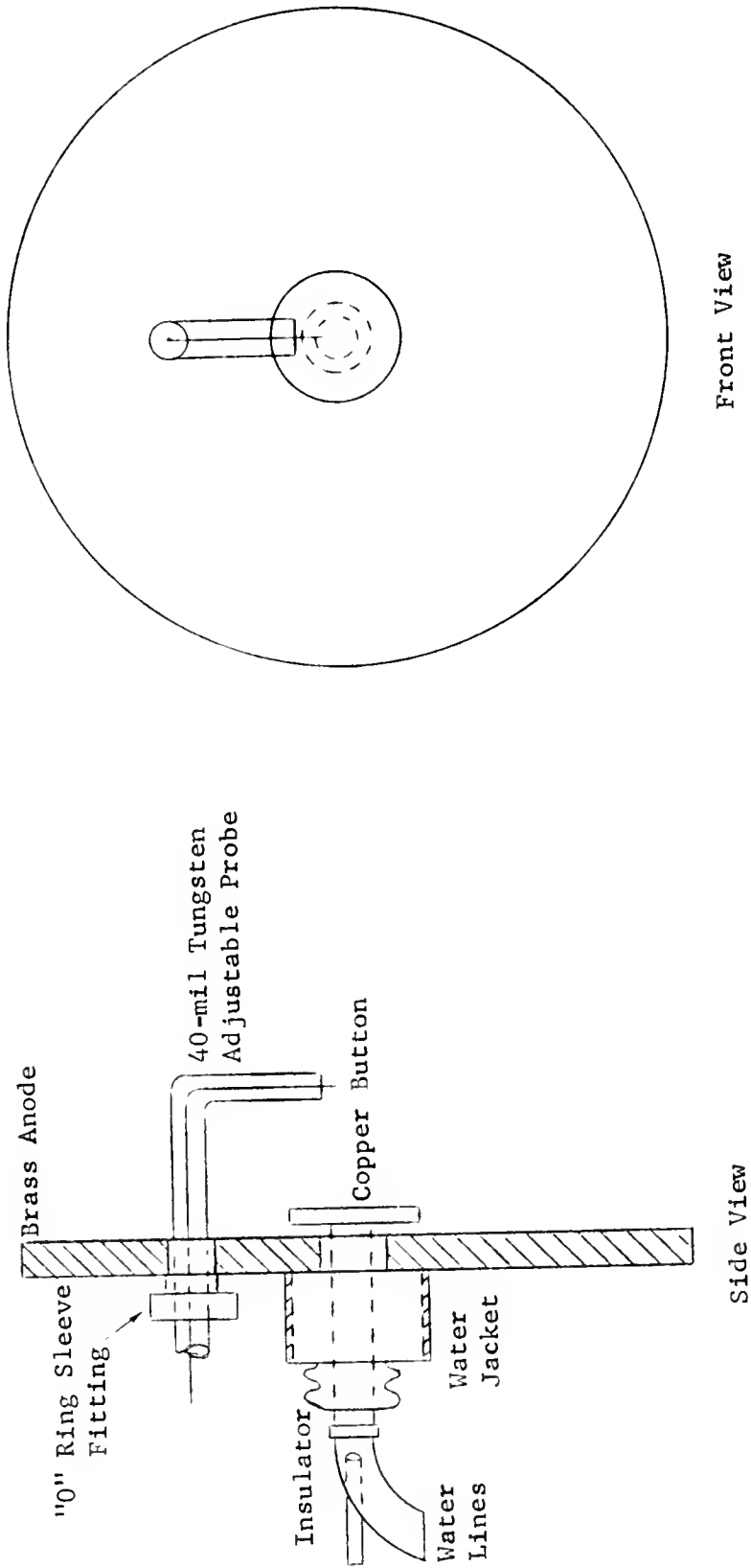


Fig. 19. Detail of the anode-button structure of the reflex arc.

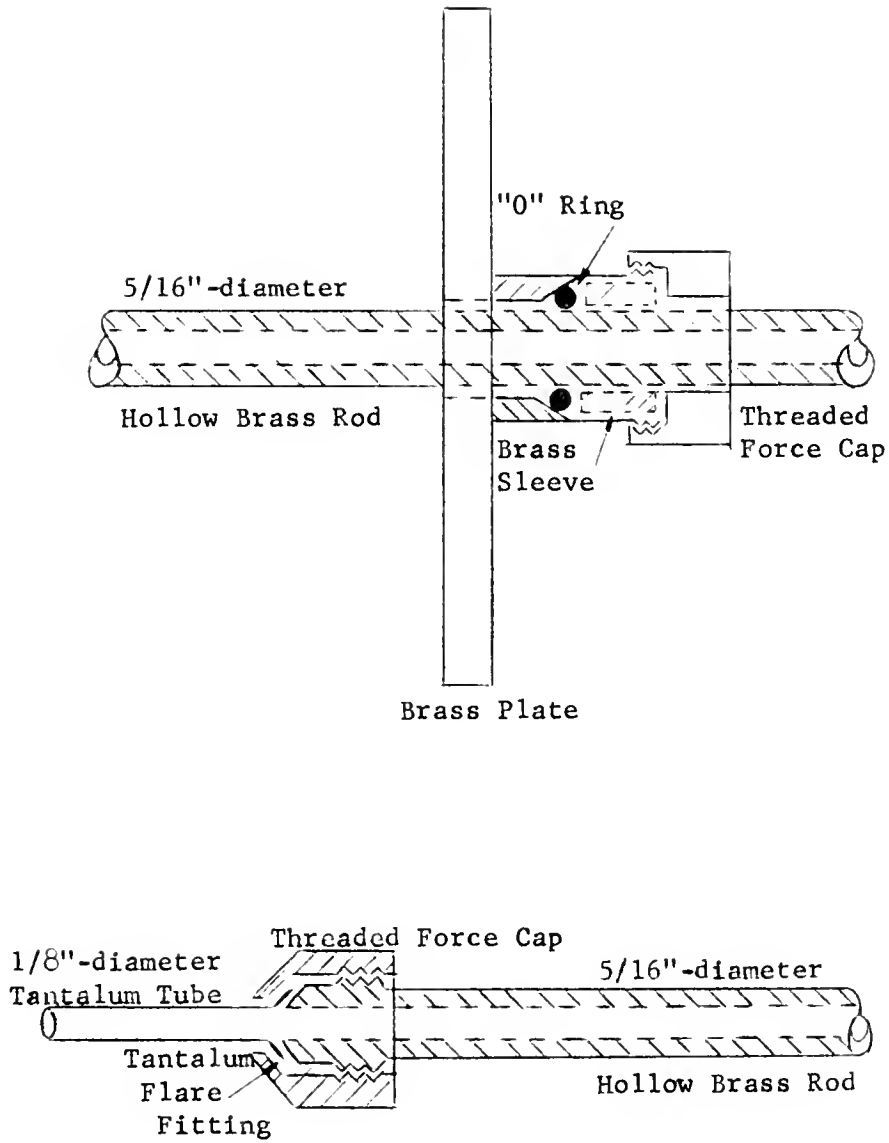


Fig. 20. Detail of the moveable cathode of the reflex arc discharge.

changed by replacing the old button with a new one. Four different button diameters were used in compiling the data which are presented and discussed in the next chapter.

CHAPTER IV

RESULTS

The results and graphs presented below are divided into three groups, consistent with the general trend of this paper.

Dual Beam-Plasma Results

In order to have an idea of the energy range of the reflected ion beam, the potential build-up on the target collector was measured as a function of the impinging beam energy and the magnetic field. Fig. 21 shows the collector potential versus the magnetic field for a beam energy of 15 keV. The beam consisted mainly of H_3^+ since the source was operated in the high pressure (~ 1000 microns) region.²⁷ Air, at three different pressures was used in these measurements to create the background plasma. From the figure it can be seen that for low magnetic field strengths, the collector potential increased rapidly as the magnetic field was increased. For magnetic fields on the cone tip above a range of 600 to 900 gauss, the collector potential decreased as the magnetic field was increased. It was also noted that the collector potential increased as the background pressure was decreased.

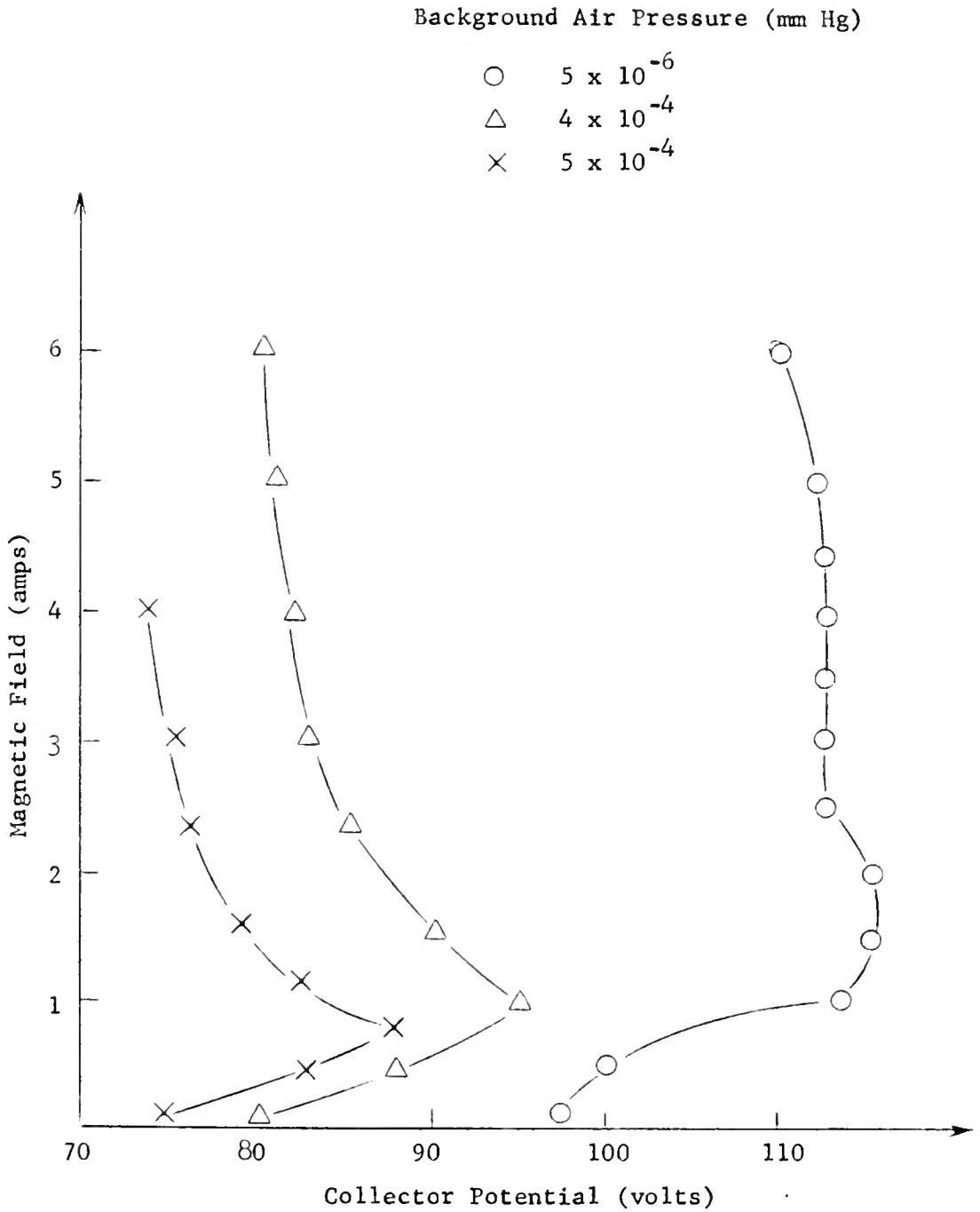


Fig. 21. Collector potential in an air plasma is plotted as a function of the magnetic field. Three different air pressures are used in conjunction with a 15-keV hydrogen ion beam.

In Fig. 22 the collector potential is plotted as a function of the beam energy for a given magnetic field strength at two different background air pressures. It can be seen that the potential increased as the beam energy was increased. It should be noted, however, that the beam current increased slightly as the accelerating potential was increased.

In Fig. 23 the potential on the collector is plotted as a function of the magnetic field for a 15.5-keV, 4-ma beam and for given background pressures in argon. The source parameters were adjusted so that the beam consisted mainly of H_2^+ and H_1^+ . From the figure it can be seen that in the low pressure region the potential decreased slightly as the magnetic field was increased to around 600 gauss. For magnetic fields above this value, the collector potential increased. It can also be seen that for a given B, the potential decreased as the pressure was increased for pressures below .3 microns. For a given argon pressure above .3 microns, the collector potential was essentially unaffected by the magnetic field. In fact, in this higher pressure range, the potential increased as the pressure was increased for a given magnetic field strength.

The collector potential dependence on the magnetic field strength using helium as the background gas is shown in Fig. 24. The source parameters were again adjusted so that the

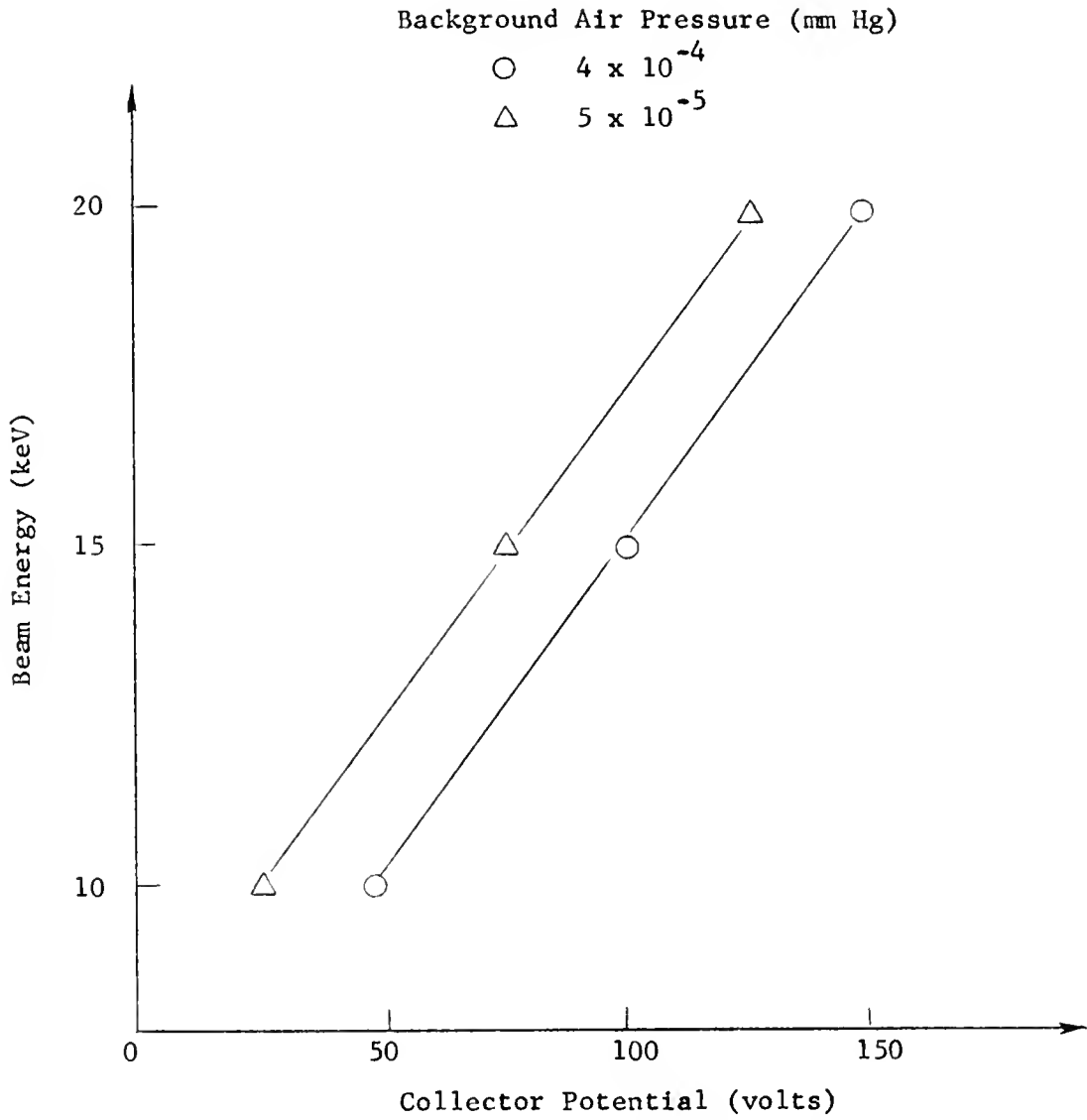


Fig. 22. Collector potential is plotted as a function of the hydrogen ion beam energy. Two different air plasma pressures are used in a constant magnetic field powered at 4 amps.

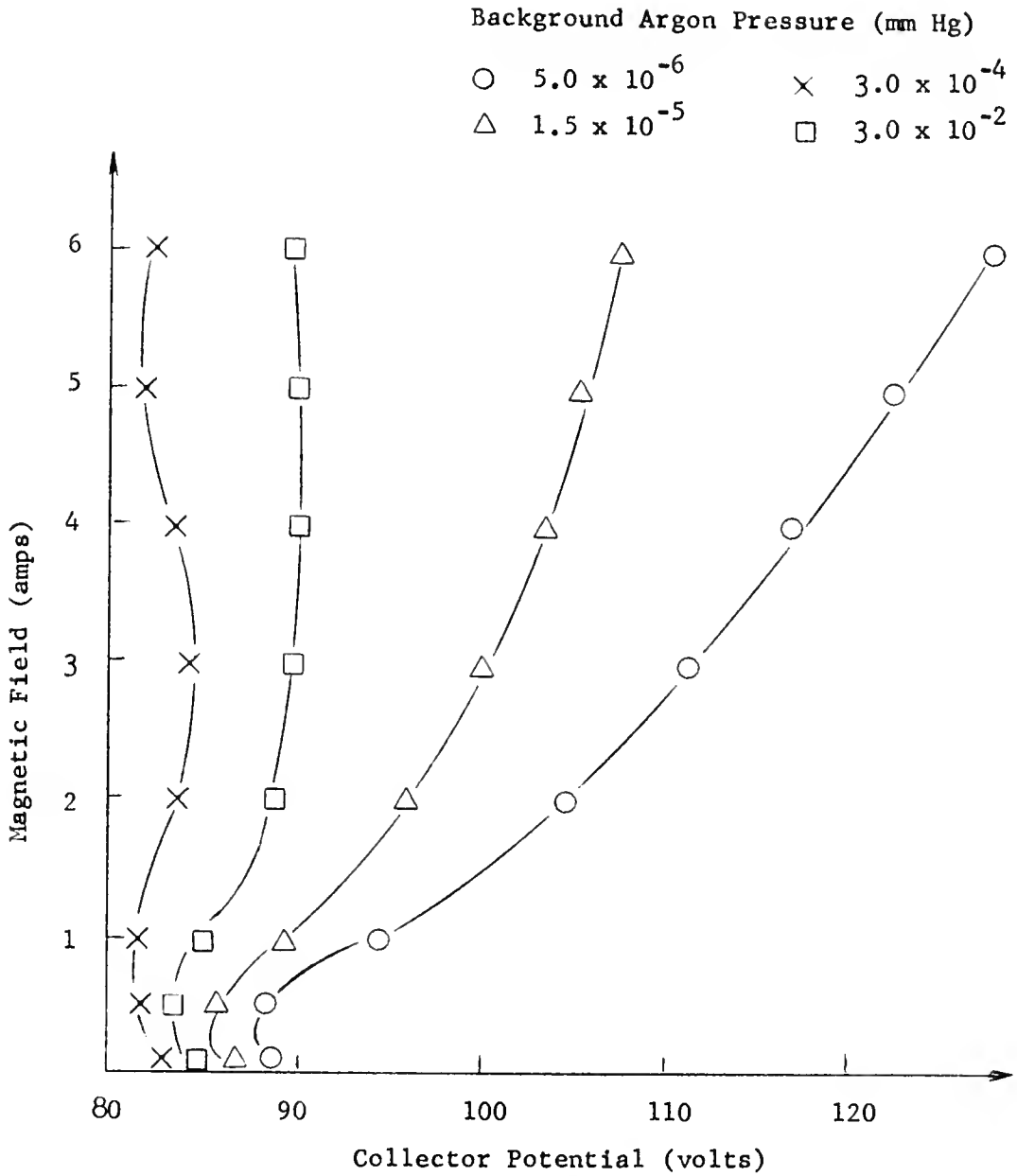


Fig. 23. Collector potential in an argon plasma is plotted as a function of the magnetic field. Four different argon pressures are used in conjunction with a 15.5-keV, 4-ma hydrogen ion beam.

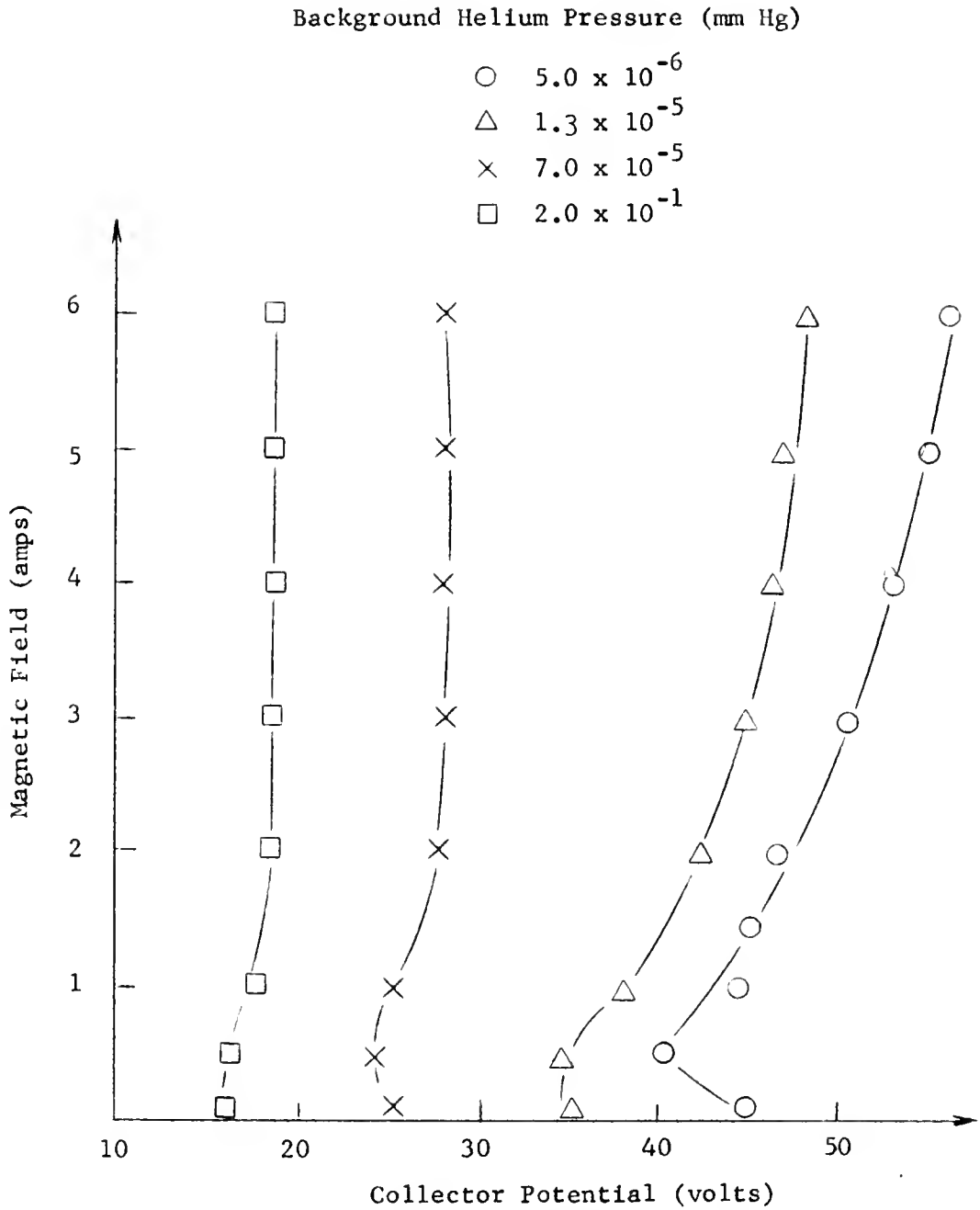


Fig. 24. Collector potential in a helium plasma is plotted as a function of the magnetic field. Four different helium pressures are used in conjunction with a 15-keV, 3-ma hydrogen ion beam.

15 keV, 3 ma beam consisted mainly of H_2^+ and H_1^+ . As in the case for argon, the potential decreased slightly as the magnetic field was increased up to 600 gauss. Above this field value, the collector potential increased and for a given magnetic field strength, the potential decreased as the pressure was increased.

Using hydrogen as the background gas, Fig. 25 shows the collector potential versus the magnetic field for a 16-keV, 4-ma beam consisting mostly of H_2^+ and H_1^+ ions. It can be seen that the slopes of the curves for the various pressures are very similar to those found using argon and helium as the background gases. The potential decreased slightly at first and then increased for values of B above 600 gauss. Again for a given magnetic field strength, the collector potential decreased as the pressure in the collector region was increased.

The slopes of the potential versus magnetic field curves were the same for the different gases with air being the exception as noted above. This exception, however, may be explained by the fact that two system conditions were different when air was used. First, the pressure changes with air were made by simply capping off one or more pumps whereas the other gas pressure changes were made by adjusting the gas flow with leak

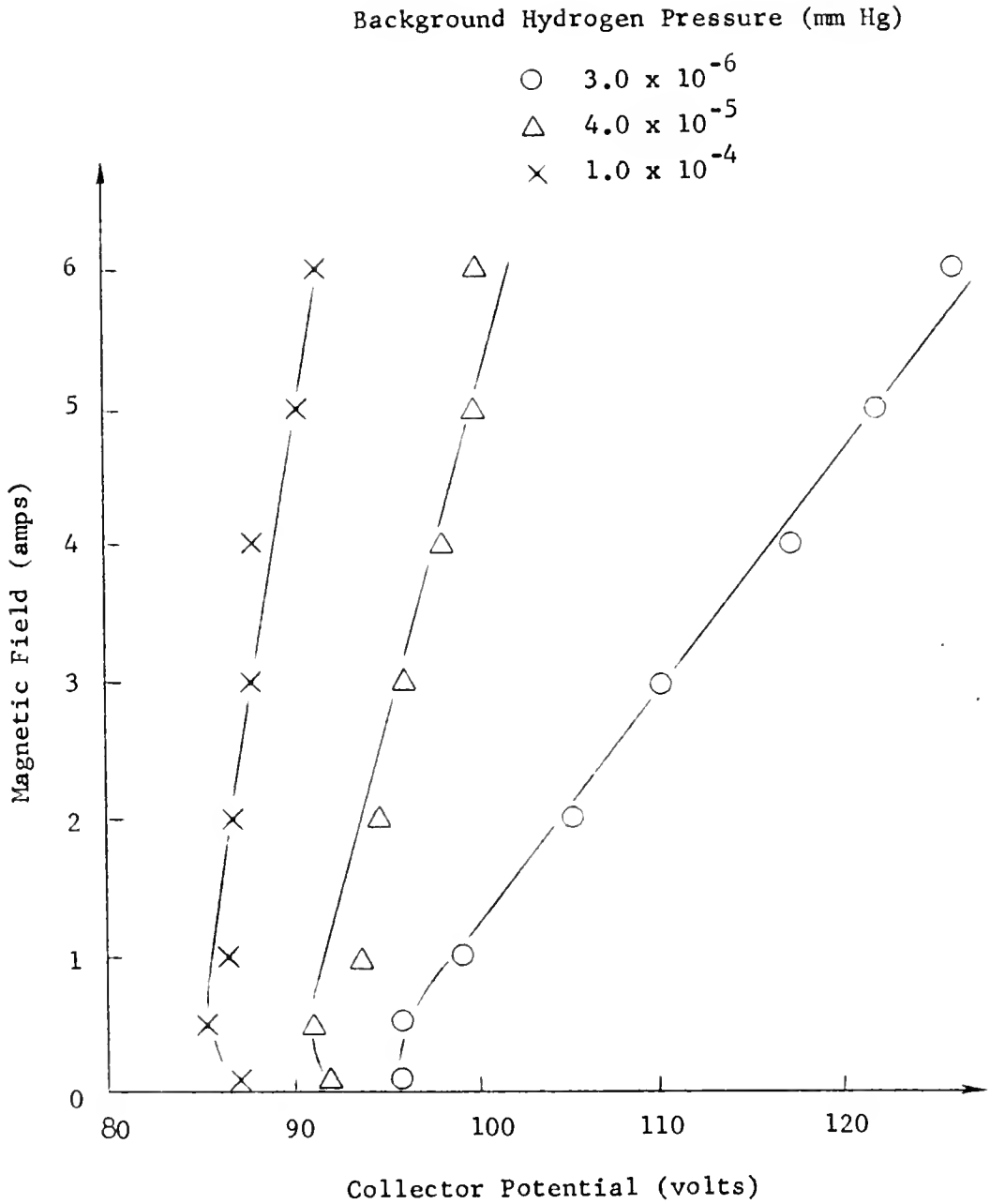


Fig. 25. Collector potential is plotted as a function of the magnetic field. Three different hydrogen pressures are used in conjunction with a 16-keV, 4-ma hydrogen beam.

valves while leaving all the pumps open. Second, the beam used in the air experiments consisted mainly of H_3^+ ions, while the beam used to interact in argon, helium and hydrogen consisted mainly of H_2^+ and H_1^+ .

All the potentials measured on the collector were relatively low compared to the beam accelerating potential, but may have given rise to a reflected beam component in any or all of the background plasmas. However, in each case, no coherent or decipherable oscillations could be found in the collector region or on the collector itself. This effect was found to occur in all of the gases used to create the background plasmas. The fact that the potential changes were the same for all gases indicates that the plasma ions were relatively unimportant in determining the final target potentials.

High Current Source Results

A relatively high current argon ion beam was extracted from the source shown in Fig. 10 when the cathode was grounded. A typical ion current-pressure dependence curve is shown in Fig. 26 for an arc current of 2.5 amp and a 1-inch-diameter shield aperture. From the figure it can be seen that no appreciable current was collected until the pressure dropped to the 1-micron range. The current then rapidly increased to 200 ma for a

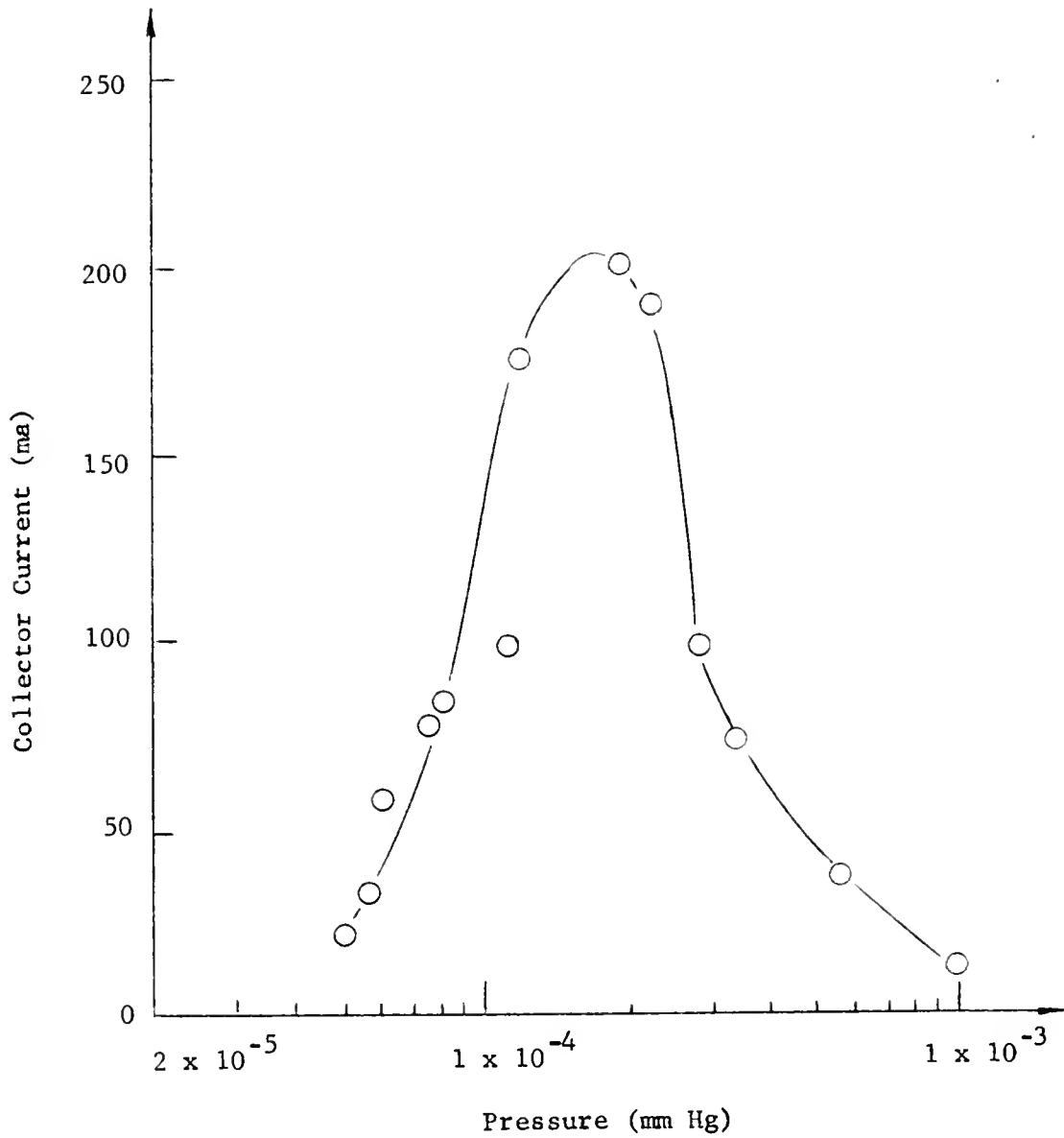


Fig. 26. Collector current I_c is plotted as a function of the source pressure for a 2.5-amp arc with a 1-inch-diameter shield aperture.

pressure of .2 microns. As the pressure was lowered even further, the ion current decreased. Fig. 27 describes the voltage-current characteristic curve for the collector at a pressure of .1 microns. The ion current remained essentially constant as the collector was biased from -500 volts to +30 volts. A further voltage increase caused a sharp current reversal indicating the onset of electron streaming to the positively biased collector.

The maximum ion current obtained from the source with a 3/4-inch-diameter shield aperture was 190 ma. The current dependence on the pressure followed the curve in Fig. 26 with a slight downward shift of the current for each pressure point. When the arc current was reduced, the beam current dropped. The voltage-current characteristic curve for the collector when the arc current was 1.5 amp and the pressure was .3 microns is shown in Fig. 28. Again the beam current remained essentially the same when the collector was negatively biased. The total collector current dropped to zero quite abruptly when the bias potential was increased to 100 volts indicating that most of the beam particles had energies in the 100-volt range. This was slightly less than the voltage drop across the arc. It should be noted that although the magnetic field has to be turned on for the beam to appear, the

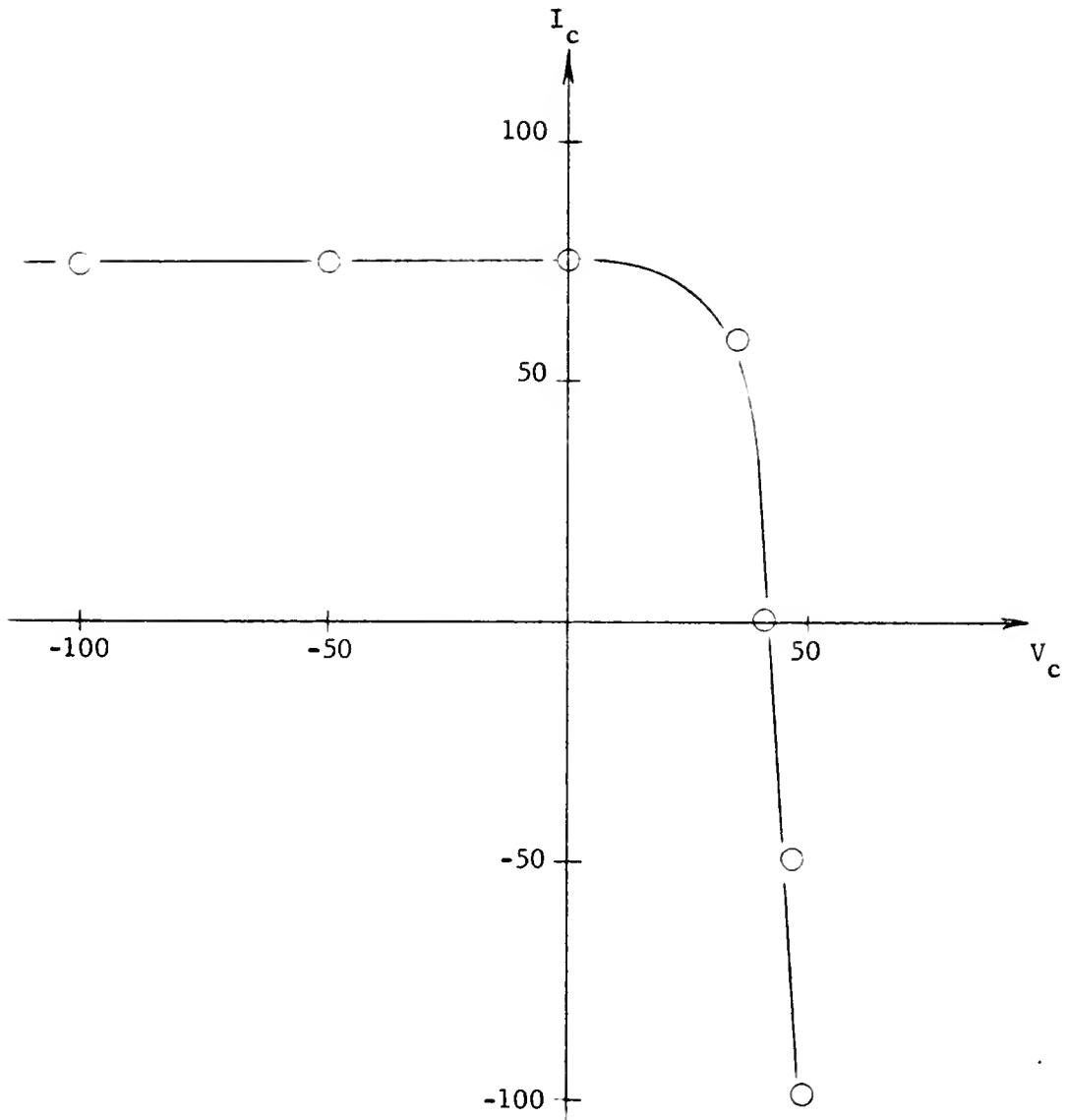


Fig. 27. Collector current I_c is plotted as function of the collector voltage V_c for a 2.5-amp arc. A 1-inch-diameter shield aperture is used and the source pressure is .1 microns.

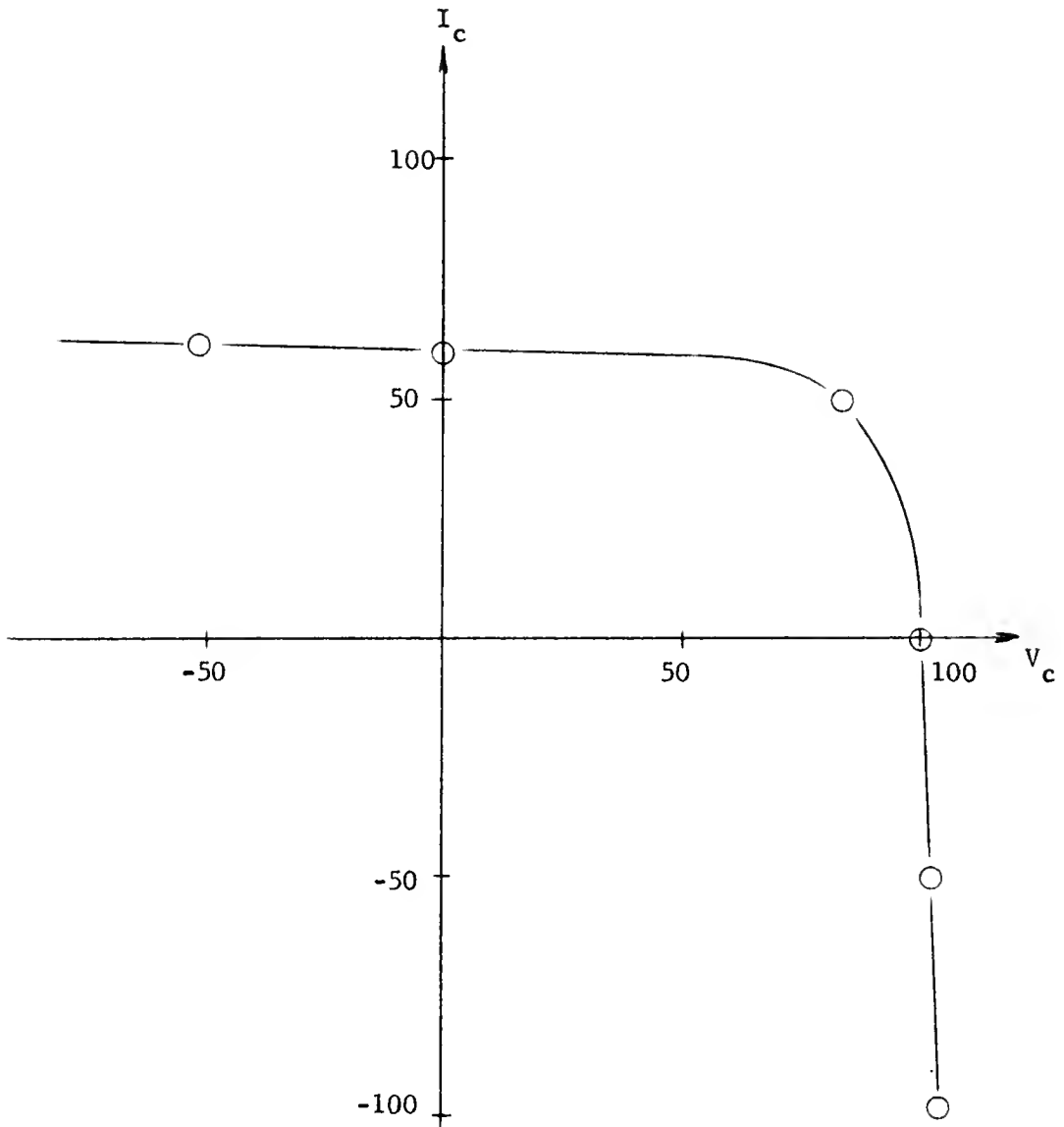


Fig. 28. Collector current I_c is plotted as a function of the collector voltage V_c for a 1.5-amp arc. A 3/4-inch-diameter shield aperture is used and the source pressure is .3 microns.

beam current appears to be unaffected by a limited change in the magnetic field. This point, however, was not studied in detail.

The anode arrangement shown in Fig. 13 was used to show that the additional magnetic field could be used to enhance the beam current. Fig. 29 shows how the beam current varies as a function of the magnetic field for a 1.5-amp arc. It can be seen that the beam current decreased for low anode magnetic fields, increased above the initial beam current, and finally decreased to an almost null current. This was observed with the coils polarized to give a total magnetic field, which increased in the radial direction. With the magnet coils polarized to give a total field decreasing in the radial direction, the beam current had the anode magnetic field dependence shown in Fig. 30. Here it can be noted that as the anode field was increased, the beam current increased until a saturation point was reached. It was also noted that a small beam current became evident as the anode field was increased when both coils were off. The potentials measured on the probes, although dependent on the polarity and strength of the fields, could not be used to interpret the observed phenomena. The noise picked up on the probes varied from 220 cycles/sec to 10^7 cycles/sec. Reproducible frequency measurements were hard

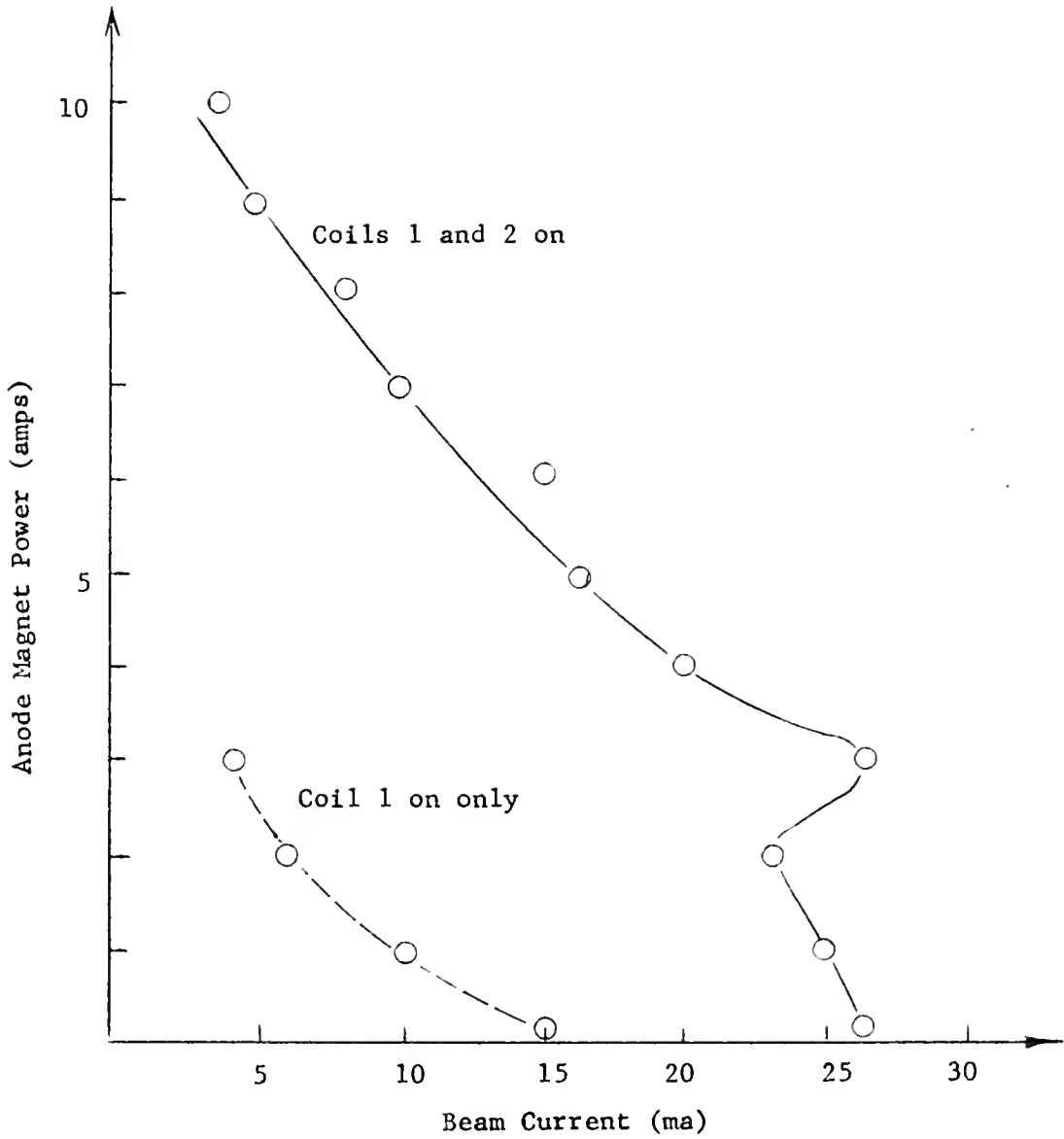


Fig. 29. The beam current from a 1.5-amp arc is plotted as a function of the radially increasing anode magnetic field.

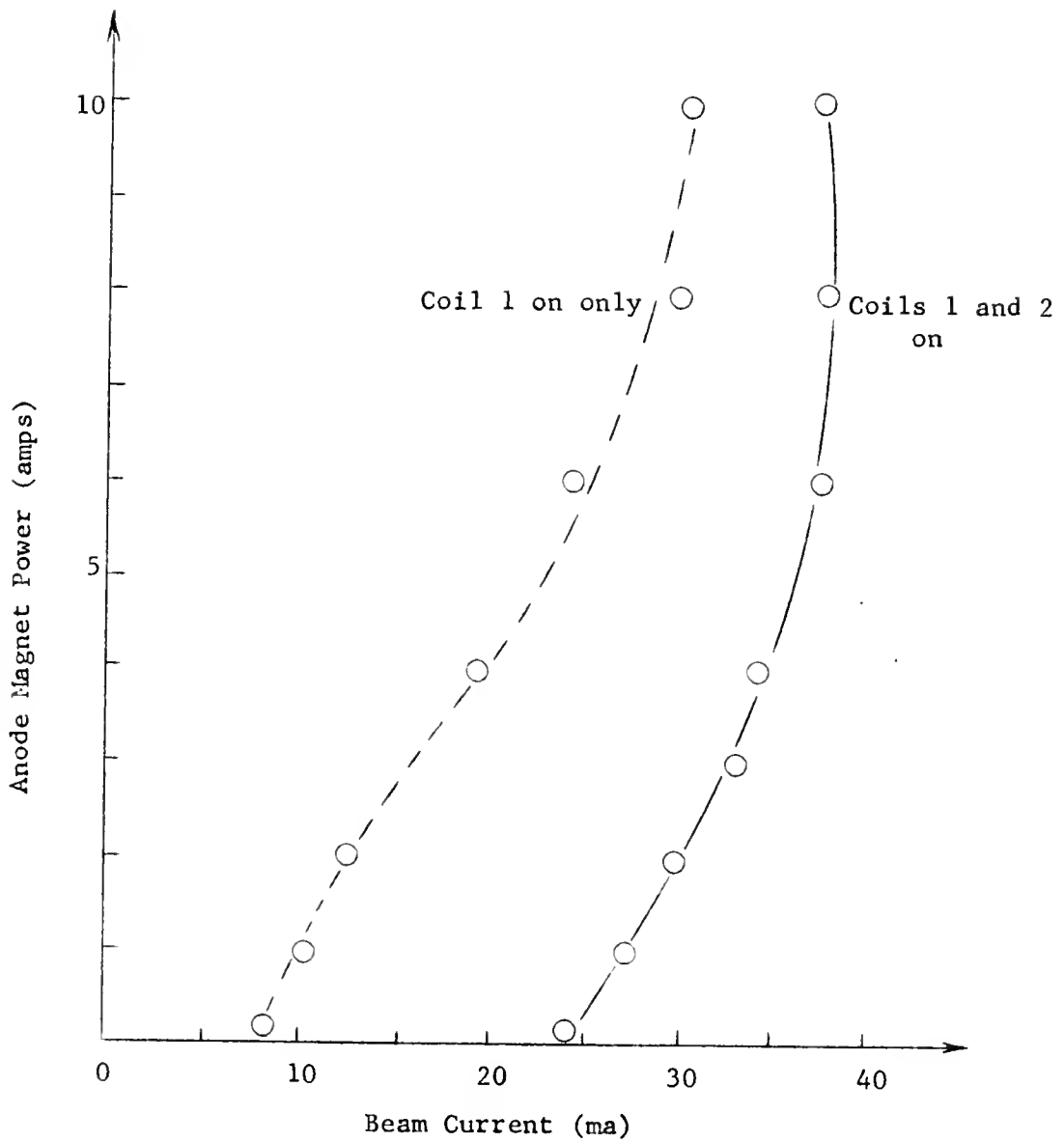


Fig. 30. The beam current from a 1.5-amp arc is plotted as a function of the radially decreasing anode magnetic field.

to obtain so no correlation could be made between the arc parameters, field strengths and radio frequency noise.

The pulse circuit shown in Fig. 15 was used to apply a variable pulse to the arc while the effect on the beam current was measured by noting the potential drop across a 2.4-ohm resistor between the collector and ground. A typical oscillogram of the pulsed beam current is shown in Fig. 31. For given source conditions, the pulsed beam current increased somewhat proportionally to the applied arc pulse as shown in Fig. 32. In Fig. 32a, a 200-volt pulse on the arc producing the .24-volt drop measured across the 2.4-ohm resistor indicated a pulse current of 100 ma above the steady beam current. In Fig. 32b, a 400-volt arc pulse producing the 12-volt drop measured across the 47-ohm resistor indicated a 250-ma current pulse above the steady 60-ma beam. The pressure in the system for this run was .7 microns and a further increase in the amplitude of arc pulse resulted in breakdown. In general, the maximum pulse voltage the arc could sustain for a given arc current, was proportional to the pressure. Fig. 33 shows that at constant pressure, arcs of higher currents could hold higher amplitude voltage pulses before breakdown occurred.

The anode arrangement shown in Fig. 16 was used to apply a variable pulse to the copper ring concentric with the arc

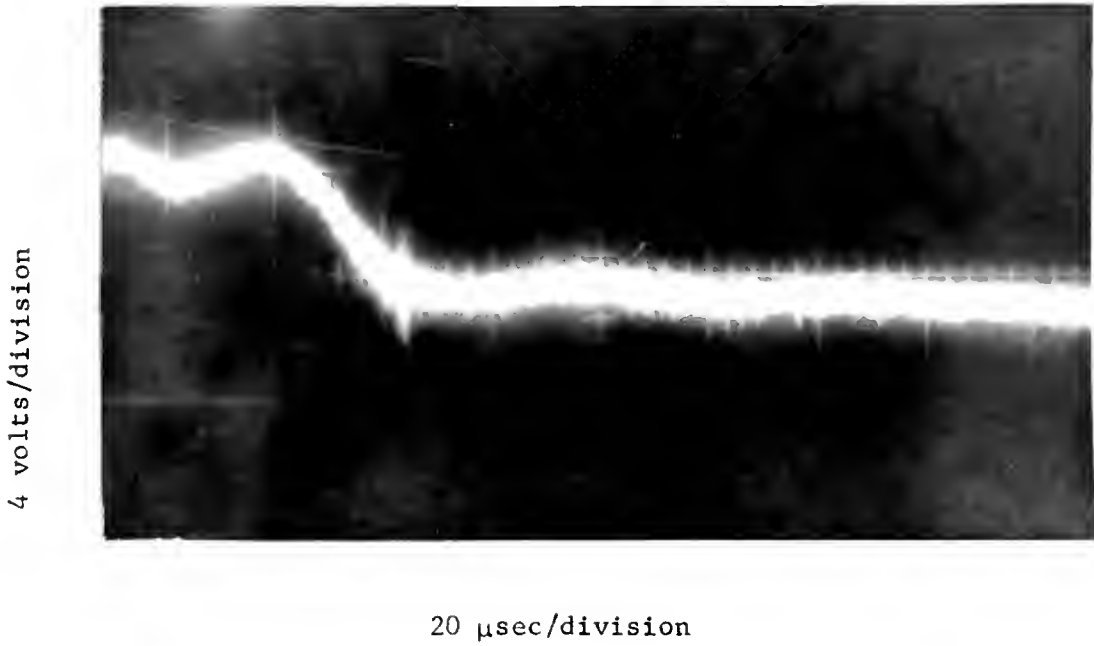
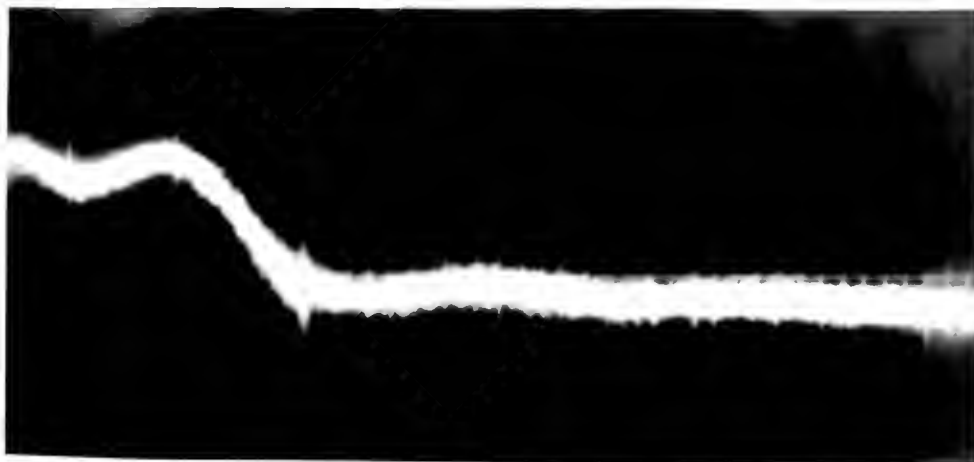


Fig. 31. Pulse voltage measured across 47-ohm resistor between the collector and ground. The 1.5-amp arc running at a pressure of .2 microns had a 60- μ sec - 340-volt square pulse applied to it.

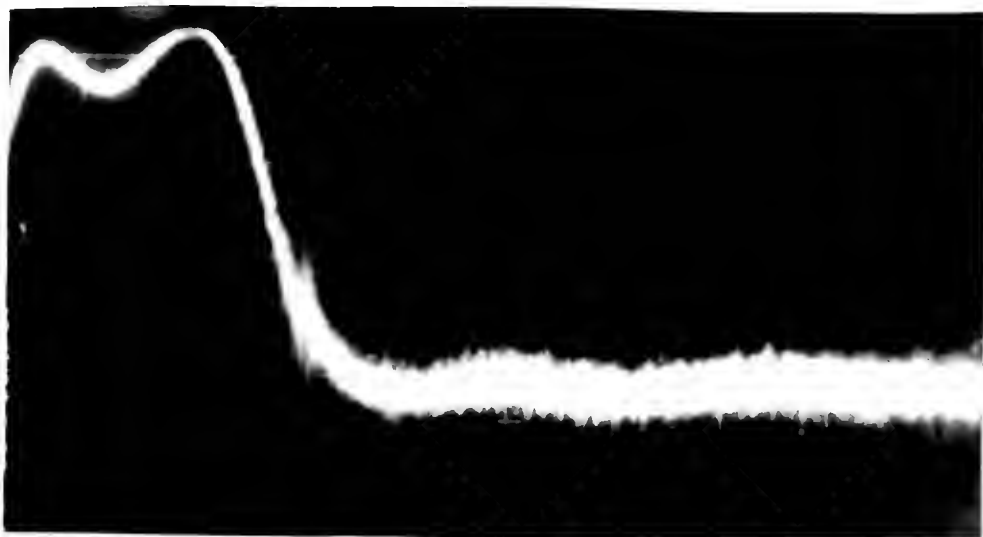
.2 volts/division



20 μsec/division

Fig. 32a. The pulsed beam voltage resulting from a 60-μsec - 200-volt arc pulse is shown as a function of time.

.2 volts/division



20 μsec/division

Fig. 32b. The pulsed beam voltage resulting from a 60-μsec - 400-volt arc pulse is shown as a function of time.

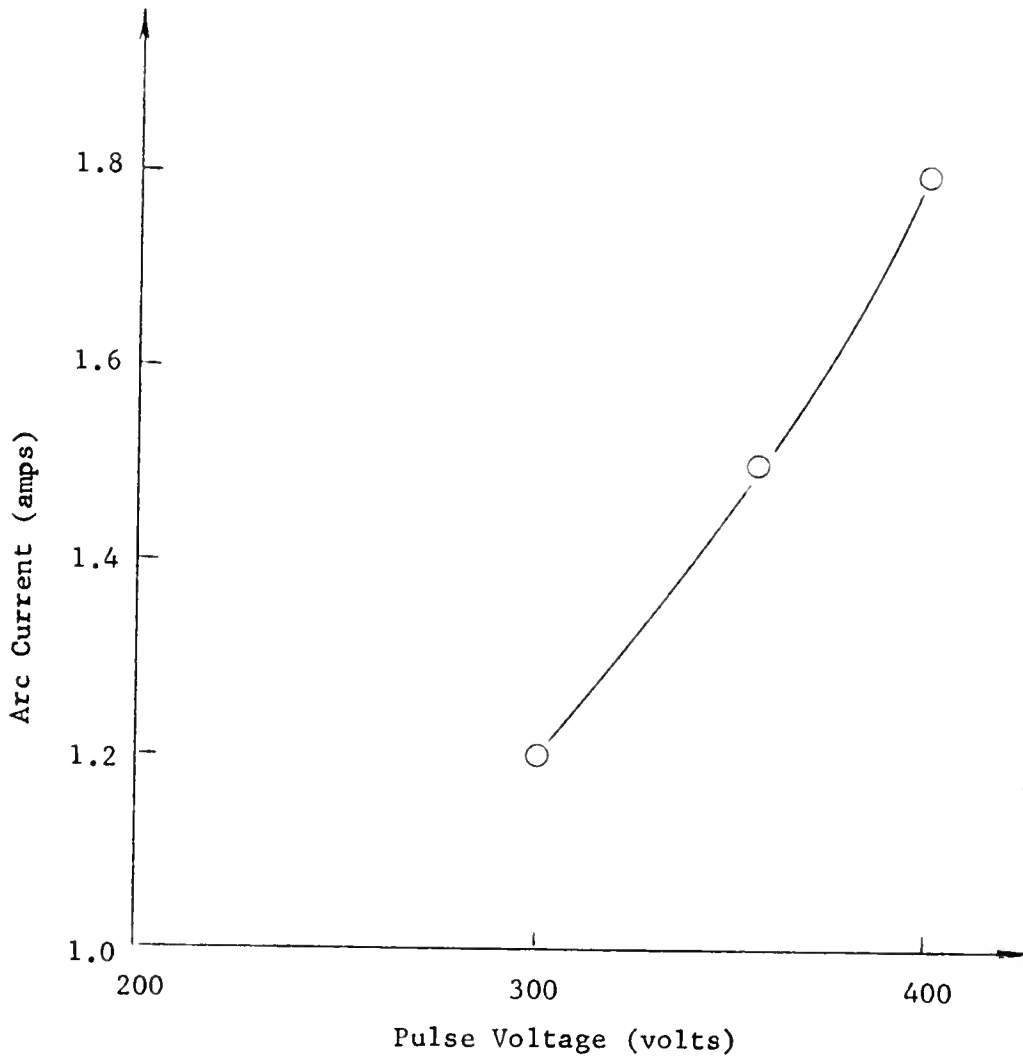


Fig. 33. The arc current is plotted as a function of the maximum sustainable pulse voltage at a pressure of .22 microns.

axis. The effects on the beam current were again determined by measuring the potential drop across a resistor between the collector and ground. Since the beam ions were not directly extracted from the main discharge, pulsing the outer disk seemed to have some possibility of pulsing the beam current without the loading effects on the main discharge. In operation, however, it was not possible to hold any appreciable potential difference on the pulsed disk relative to the anode. Therefore, the pulsed beam current using this geometry had the same characteristics as those found when the anode was pulsed.

The circuit shown in Fig. 17 was used to provide a constant current pulse to the arc. The control of current with this circuit provided a smoother potential to the arc with over-voltages of several hundred volts for approximately .5 milliseconds duration. Fig. 34 is a typical oscillogram of the pulsed beam current found by again measuring the potential drop across a resistor between the collector and ground. From the figure it can be seen that the pulsed beam current was 20 ma above the steady 30-ma beam current. The pulsed currents obtained with this circuit were always considerably lower than those found using the two previous pulse circuits. It was also found that the amplitude of the beam current pulse did not depend on the amplitude of the applied pulse. The pulsed

2 volts/division

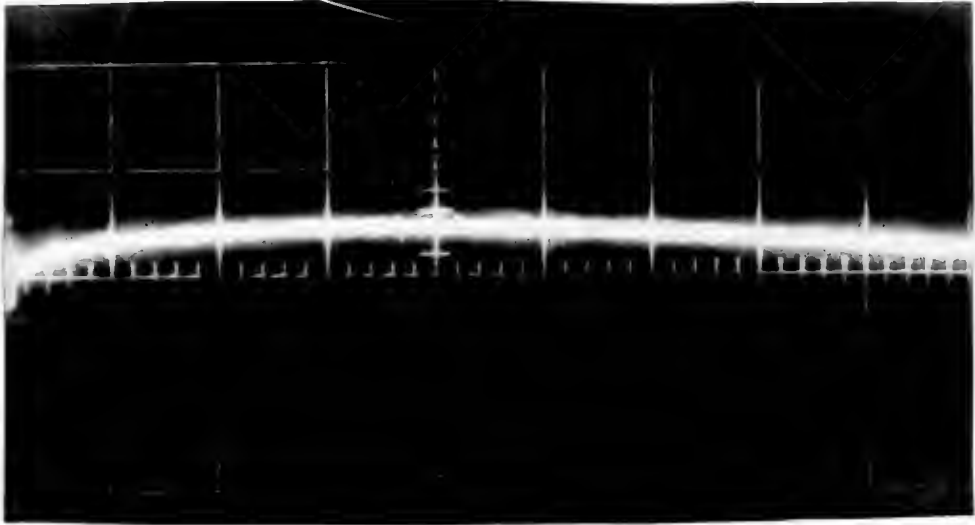
20 μ sec/division

Fig. 34. The pulsed beam voltage resulting from a 6-amp arc pulse is plotted as a function of time. The arc current was 1.5 amps and the pulse voltage was measured across a 100-ohm resistor between the collector and ground.

current did, however, increase when the steady beam current was increased.

Reflex Discharge Results

Fig. 35 represents a typical oscillogram of the frequencies observed on the variable probe or on any of the ungrounded electrodes when using the discharge arrangement shown in Fig. 18. For the source parameters given in Fig. 35, a frequency of 4.2×10^4 cycles/sec was observed. This low frequency range, which was investigated by changing the magnetic field, pressure, cathode-button separation, and button radius, was found only when the magnetic field was on while the button was insulated from the anode. Fig. 36 shows the frequency dependence on the magnetic field while using the separation distance as a constant parameter. The graph shows, as in all cases, that the observed frequency increases as the magnetic field B is increased. The amplitudes of the increased frequencies, however, appeared to be independent of B . The minimum B necessary for the low frequency oscillations to become apparent was not investigated because the magnet power supply was not continuously variable.

The frequency dependence on the cathode-button separation is shown in Fig. 37. By adjusting the cathode, the separation was varied from 1/8 inch to 7 inches. For values above 1 inch,



10 μ sec/division

Arc current = 1 amp

Electrode separation = 2 inches

Button radius = 3/4 inch

Pressure = .2 microns

Magnet power on 1

Fig. 35. The oscillogram represents the variable current fluctuation in time to the probe and arc electrodes.

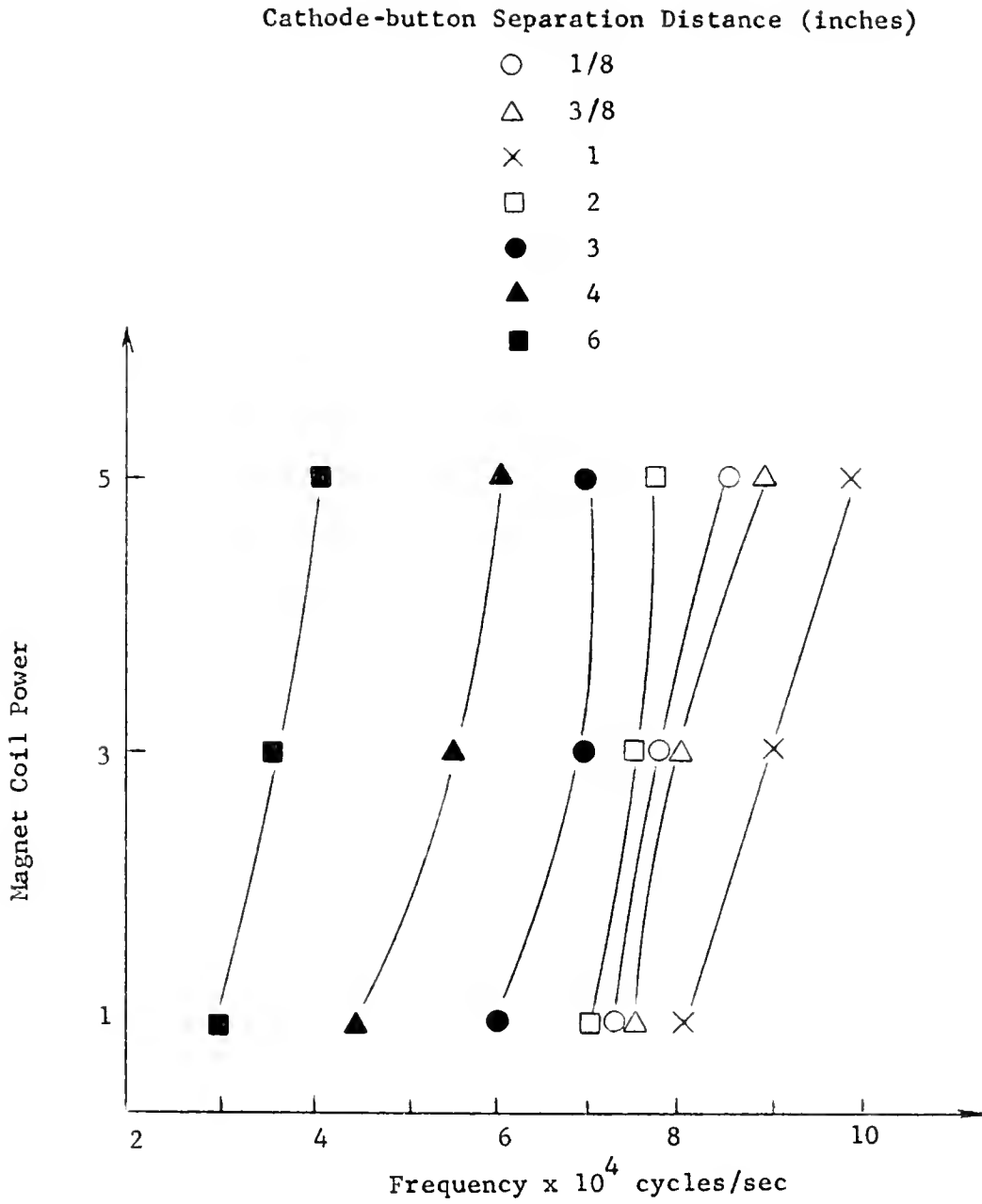


Fig. 36. The frequency is plotted as a function of the magnetic field for different cathode-button separation distances. The arc was operated at 1.0 amp with a 3/4-inch-diameter button at a pressure of .2 microns.

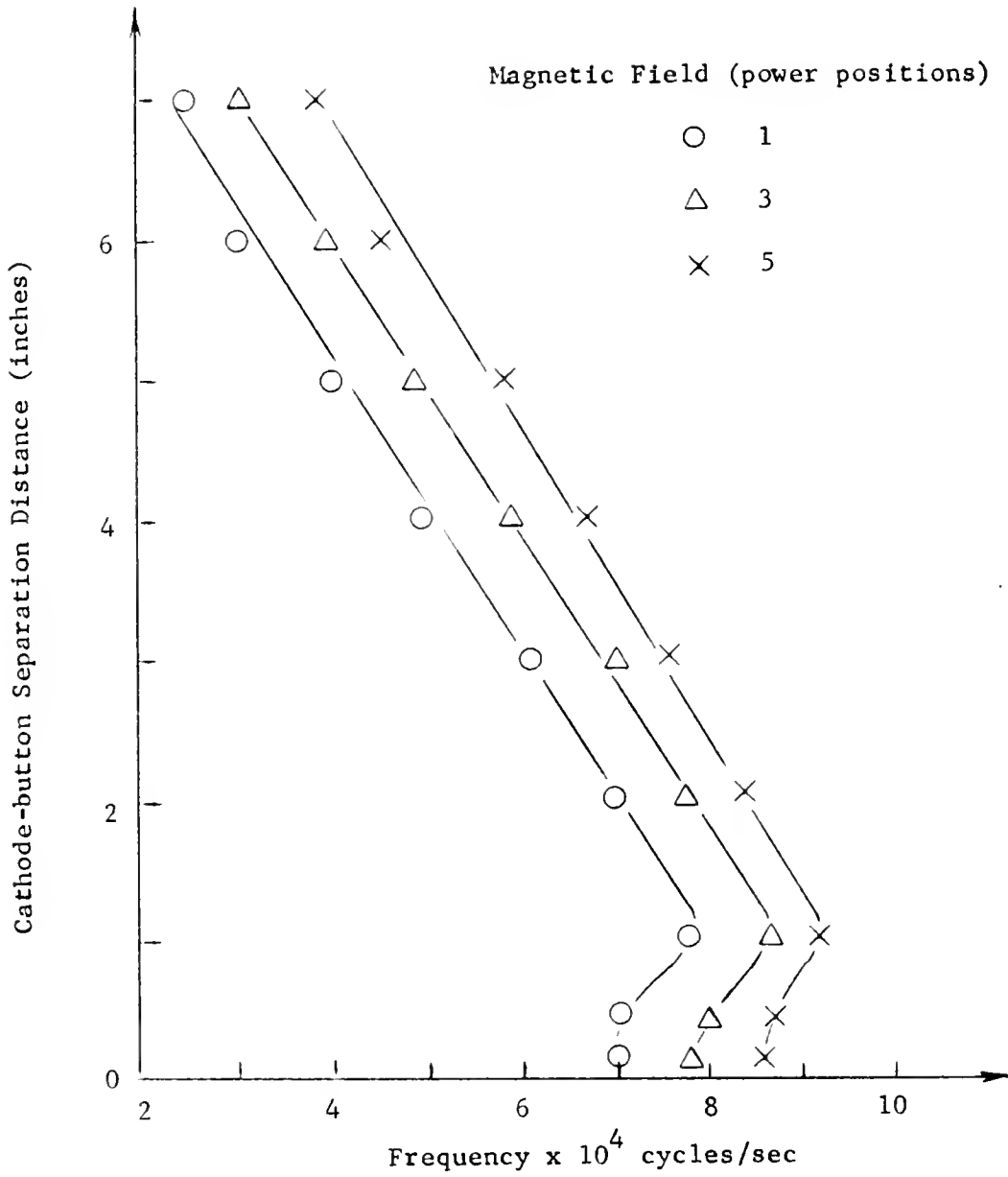


Fig. 37. The frequency is plotted as a function of the cathode-button separation distance for different magnetic fields. The arc was operated at 1.0 amp with a 3/4-inch-diameter button at a pressure of .2 microns.

the frequency decreased as the separation was increased. For separation values below 1 inch, the frequency increased as the separation was increased. The frequency dependence on the pressure is shown in Fig. 38. In general, the frequency increased for given source conditions as the pressure was decreased. It should be noted that these low frequency oscillations were never observed until the pressure dropped below the 1.0 microns range. This was the same pressure range at which the ion beam was extracted from the high current source shown in Fig. 10. Although the frequency dependence on the pressure was not too critical in the low pressure region, it was found that the amplitude decreased as the pressure was increased. Above the 1.0 micron-range, megacycle noise, as shown in Fig. 39, independent of the magnetic field, was observed on the probe.

By taking points from curves plotted using different buttons, a button-radius versus frequency curve was obtained. Fig. 40 shows that the frequency decreased as the button radius was increased. This dependence was found to exist for all magnetic field strengths, electrode separations, and pressures.

A series of measurements were made plotting frequency as a function of the magnetic field, pressure, and electrode separation for different arc currents. Fig. 41 shows that the

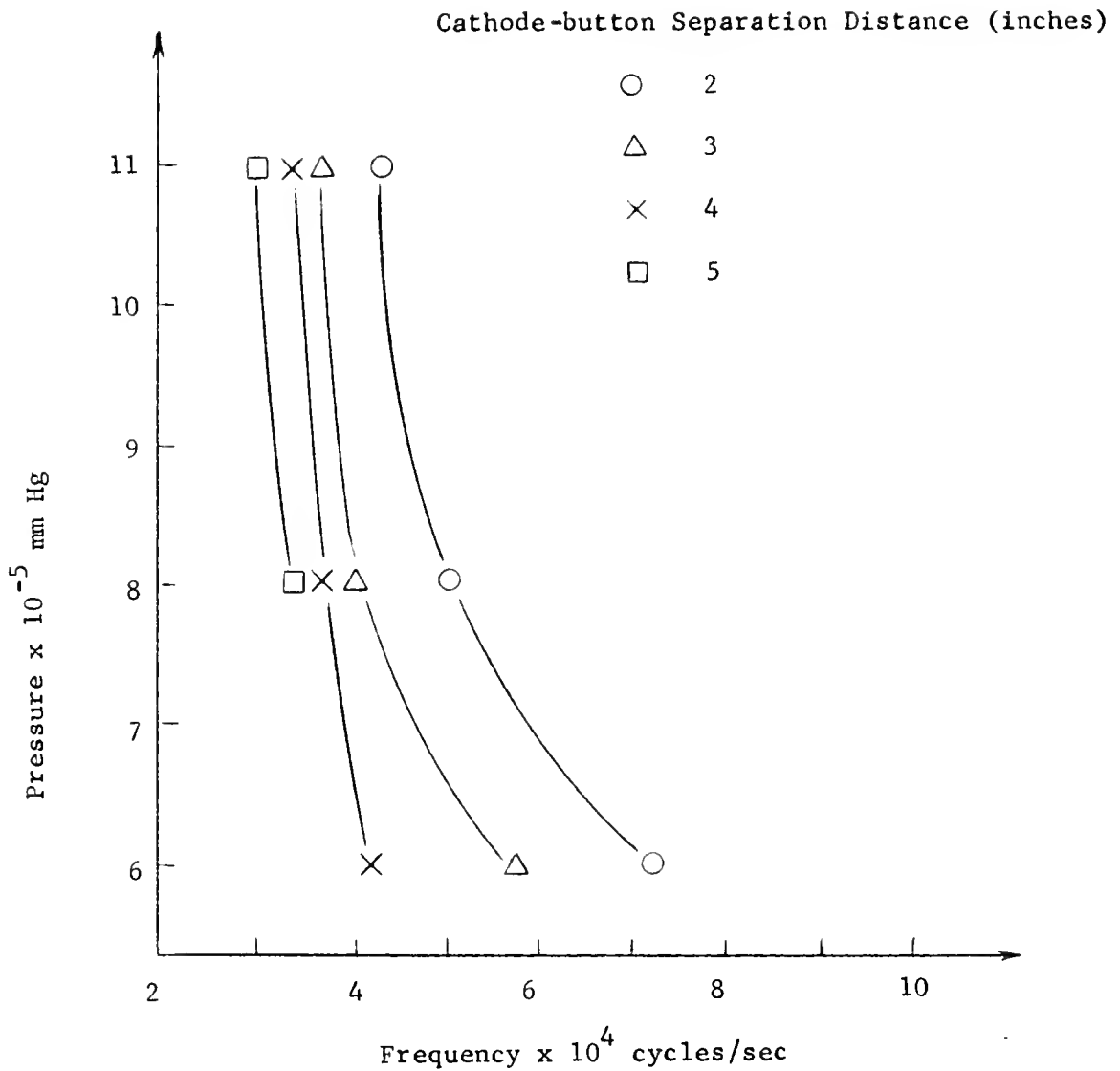
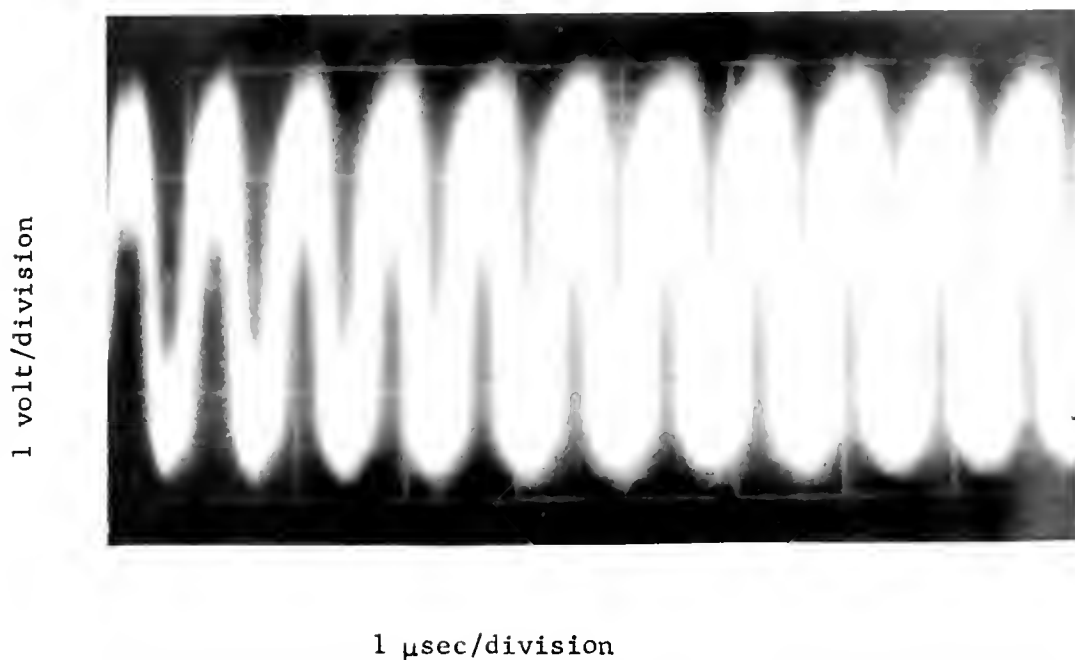


Fig. 38. The frequency is plotted as a function of the pressure for given cathode-button separation distances. A 1 1/4-inch-diameter button was used while the arc was operated at 1.0 amp with the magnet power on 1.



Arc current = 1.0 amp

Magnetic field = 0

Electrode separation = 2 inches

Button radius = 1 inch

Pressure = 50 microns

Fig. 39. The oscillogram represents the constant current fluctuation in time to the probe and arc electrodes.

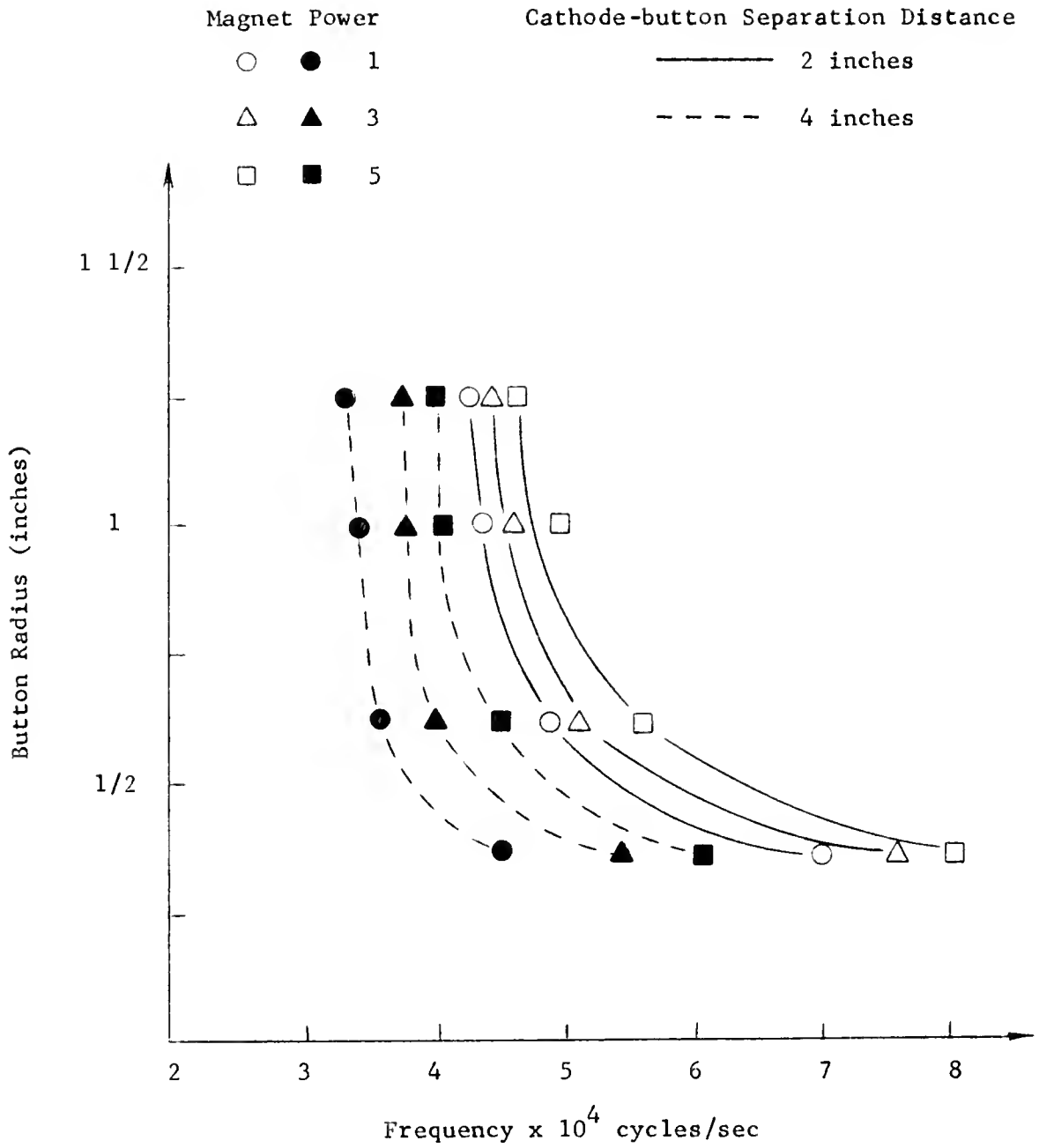


Fig. 40. The frequency is plotted as a function of the button radius. The arc is operated at 1.0 amp at a pressure of .2 microns for given magnetic fields and cathode-button separation distances.

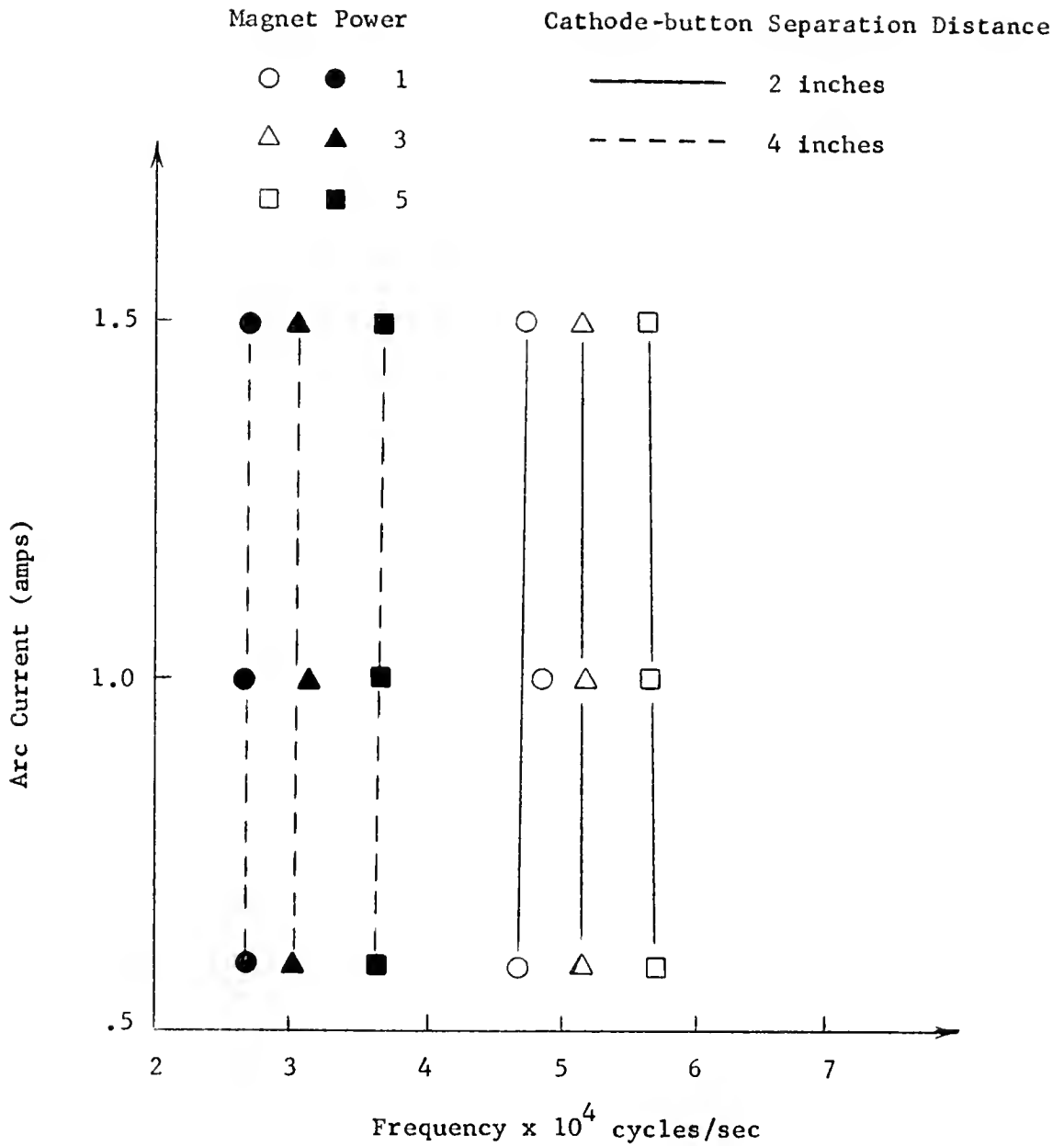


Fig. 41. The frequency is plotted as a function of the arc current. The cathode-button separation distance and magnetic field is varied using a 1 1/4-inch-diameter button at a pressure of .2 microns.

low frequency oscillations were relatively independent of the arc current.

The probe position dependence of the collected signals was carefully examined. It was found that the observed signals were independent of the longitudinal probe position, but the radial positioning of the probe was found to be important. In almost all cases observed, the cleanest and highest amplitude signal was found when the probe was located at the edge of the button. The floating potential on the Langmuir probe at the button edge was always positive as indicated in Fig.

42. As the probe was rotated toward the center, the amplitude of the signal decreased slightly. For the negative potential range, generally found within 1/8 inch from the arc axis, the coherent signals were washed out by background noise. This discontinuity in the ability to measure coherent signals indicates that the rotational modes of oscillations were no longer coupled to the longitudinal modes in the center of the arc. Therefore, most of the investigations were carried out with the probe set radially at the button edge.

Although the diffusion current from the arc was not measured, the arc voltage V_a was measured as a function of the magnetic field, electrode separation, and button radius. By assuming the

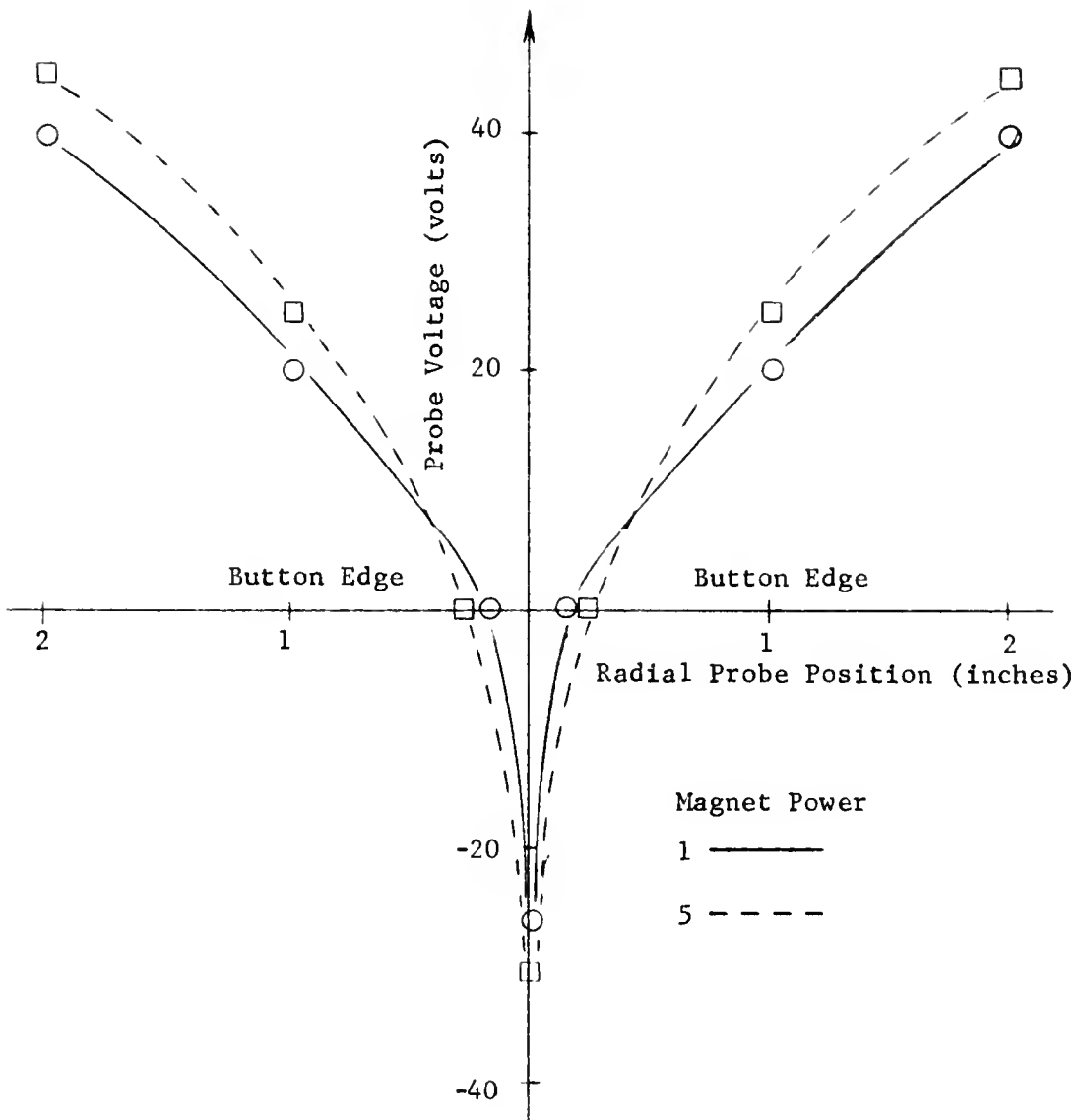


Fig. 42. The floating potential of the variable probe is plotted as a function of the radial position of the probe. Two different magnetic fields are used for an arc current of 1.0 amp at a pressure of .2 microns.

arc voltage to be proportional to the longitudinal electric field a comparison of Fig. 1 with Fig. 43 shows that the pressure and magnetic field values were in the range allowing enhanced diffusion to take place. As the magnetic field was increased, the arc potential increased in direct contrast to what is expected for collisional diffusion, but agreeing with enhanced diffusion experiments.⁹

In Fig. 44, the arc voltage is plotted as a function of the electrode separation. From this figure it can be seen that the arc voltage decreased as the separation was increased inferring a decrease of enhanced diffusion. This arc voltage decrease, however, is the normal arc behaviour for increased discharge lengths so the above statement concerning diffusion dependence should not be taken too seriously.

Fig. 45 shows a plot of the arc voltage versus the button diameter. The voltage increased as the diameter was increased up to 2 inches. For the 2 1/2-inch-diameter button, V_a decreased indicating either a decrease in the diffusion current or a change in the arc operating mode.

The Langmuir probe was used to measure the ion density n_+ and the electron temperature T_- of the reflex discharge. Although there is no theoretical basis for the Langmuir theory to

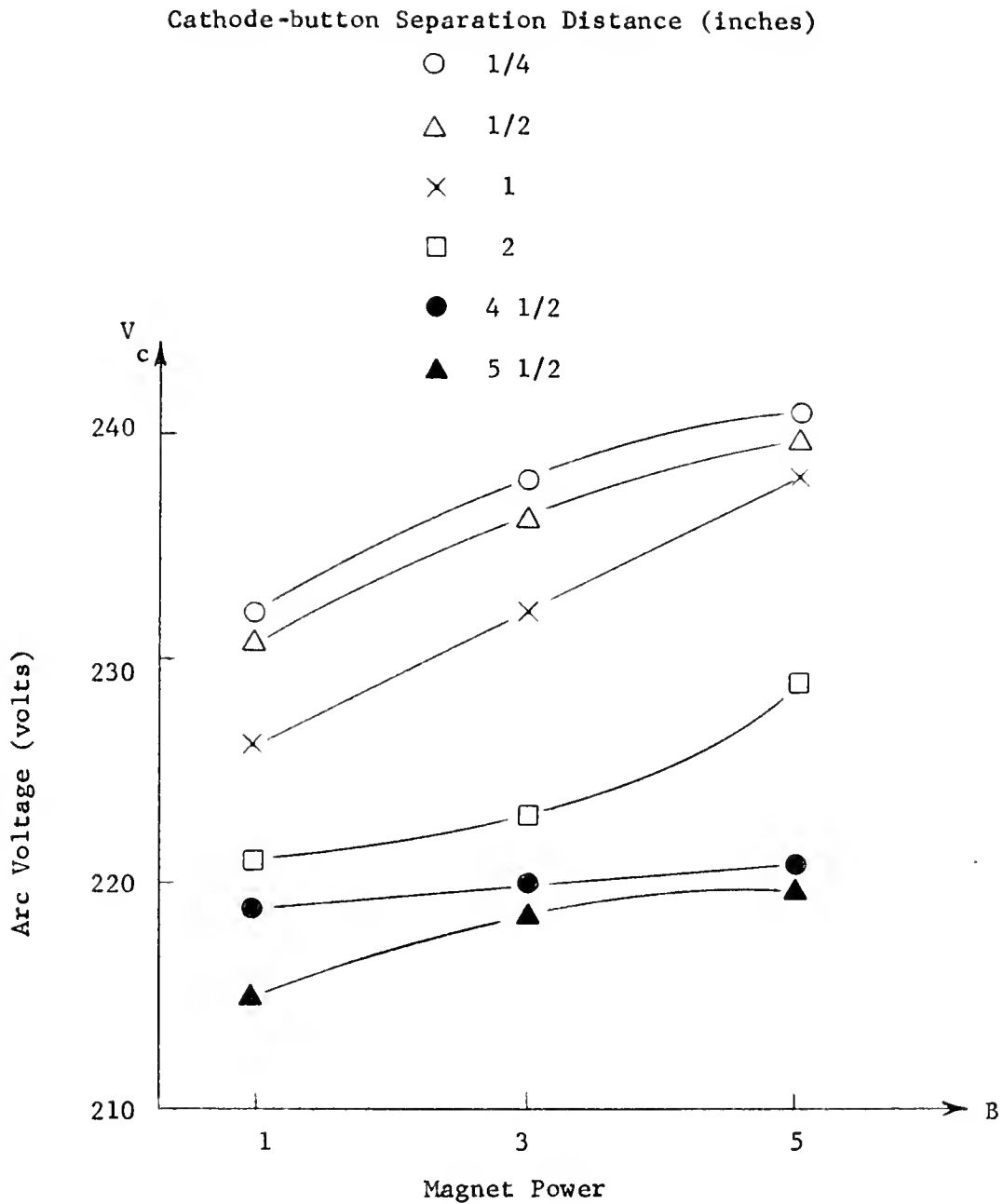


Fig. 43. The arc voltage is plotted as a function of the magnetic field for different cathode-button separation distances. A 2-inch-diameter button was used while the arc was operated at 1.0 amp at a pressure of .15 microns.

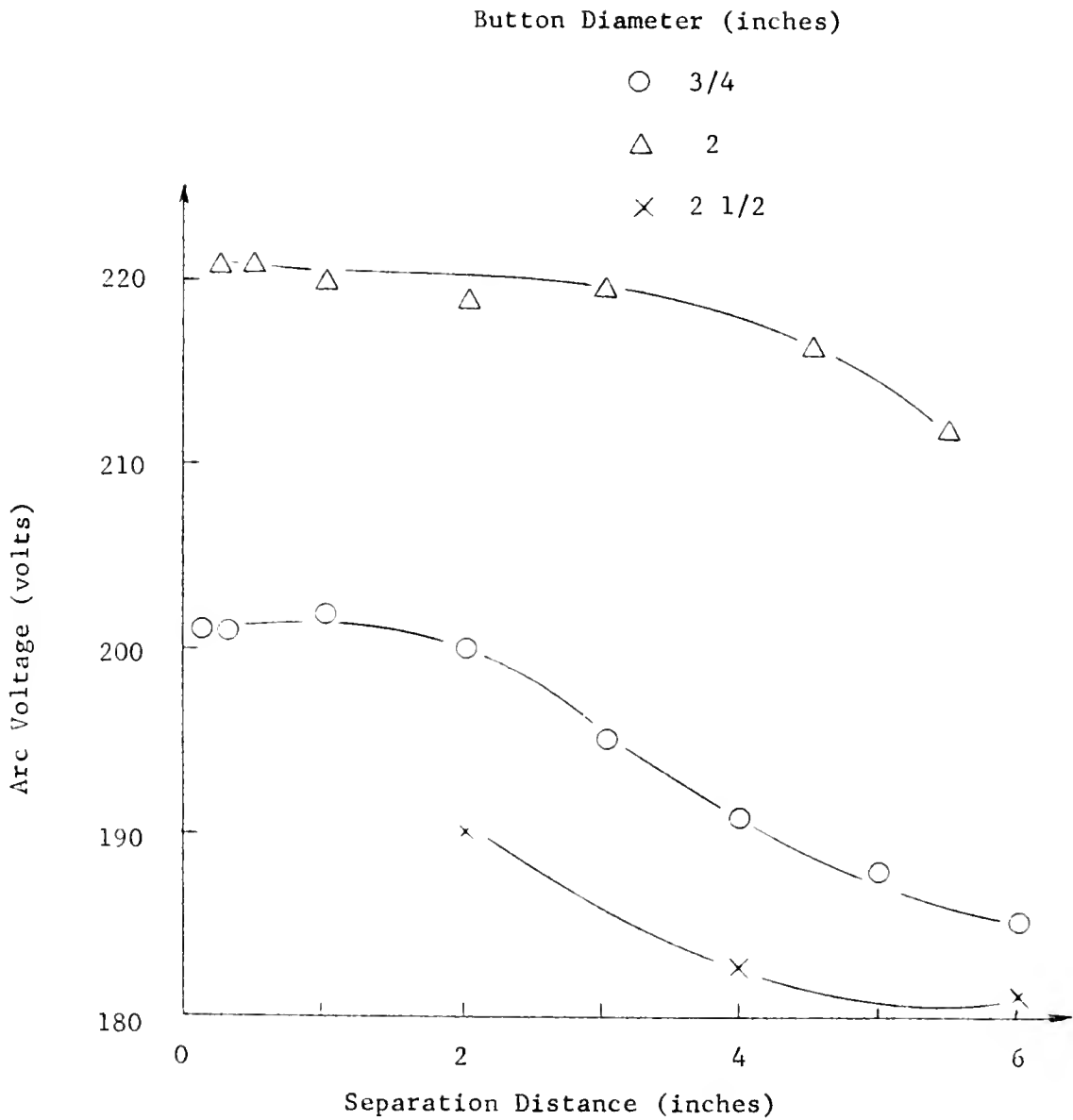


Fig. 44. The arc voltage is plotted as a function of the cathode-button separation distance for different button diameters. The magnet power was on 1 while the arc was operated at 1.0 amp at a pressure of .2 microns.

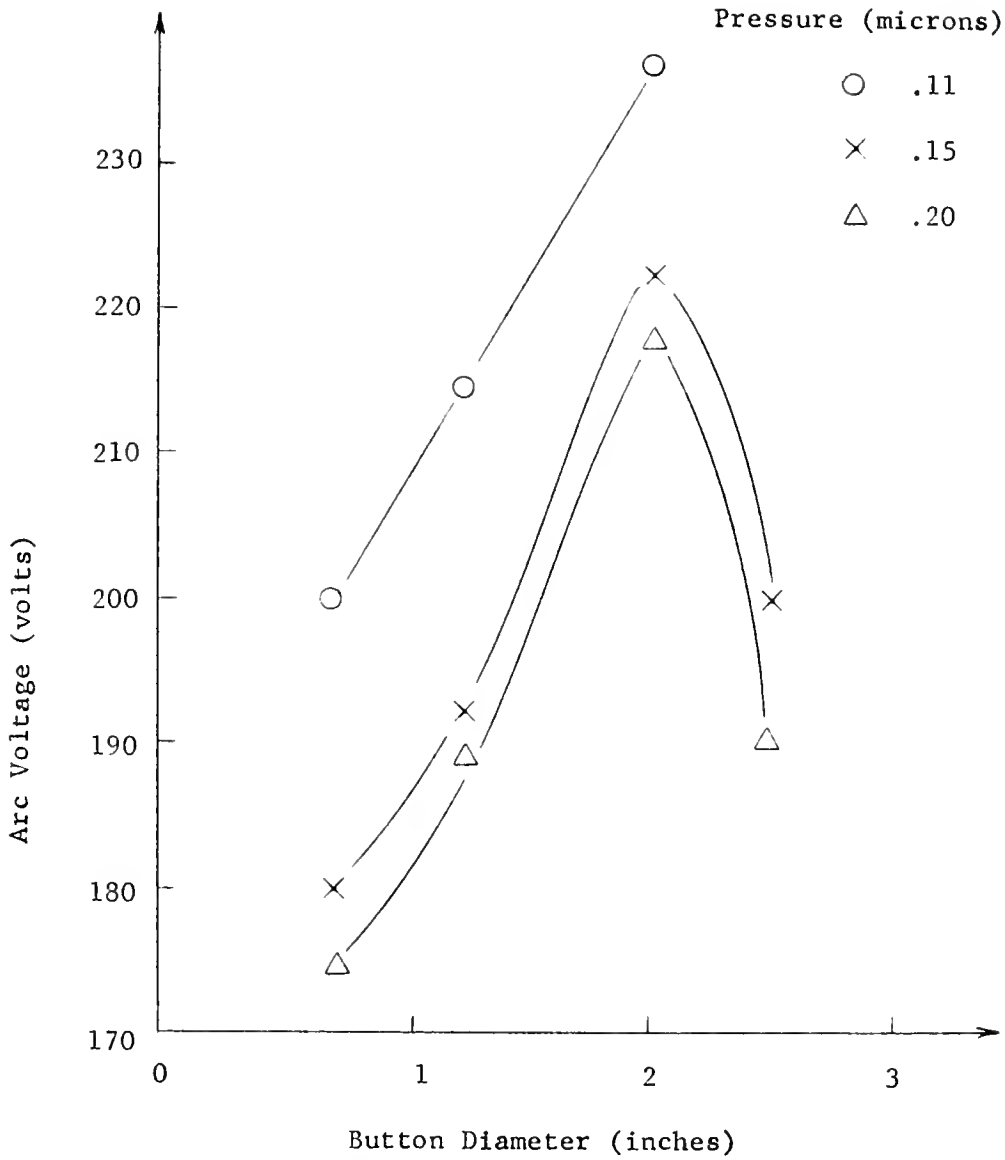


Fig. 45. The arc voltage is plotted as a function of the button diameter for three different pressures. The arc was operated at 1.0 amp with the magnet power on 1 and a separation distance of 2 inches.

hold in a magnetic field, it appears from experiments that these two parameters can be determined in the same way as in the absence of a magnetic field.¹⁷ The ion density was found to be on the order of 10^{12} particles/cm³ while the electron temperature values varied between 10^4 and 10^5 °K.

By assuming the plasma to be charge neutral, the electron plasma frequency was determined to be on the order of 9×10^9 cycles/sec while the ion plasma frequency was on the order of 3×10^7 cycles/sec. The gyrofrequency of the electrons ranged from 5×10^8 cycles/sec to 1.4×10^9 cycles/sec depending on the longitudinal position of the electron and the magnet power. The gyrofrequency of the argon ions in the reflex discharge ranged from 6.8×10^3 cycles/sec to 14.5×10^3 cycles/sec.

CHAPTER 5

CONCLUSIONS

A brief summary of the experimental results and a comparison with theory, where possible, is given below. Again the discussion will be divided into the three phases of work covered in the body of this dissertation.

Dual Beam-Plasma Interaction

Positive potentials on the order of 100 volts were found on the magnetic target of the high energy hydrogen ion beam when the magnetic field was increased to the 2000 to 4000 gauss range. These results were essentially the same when argon, helium and hydrogen were used to create the background plasma. Without the magnetic field the potentials on the beam target were negligible. These simple measurements of the floating potential of a target exposed to an ion beam in the presence of a plasma are fundamentally indicative of beam stability. This is particularly so when the comparison is made with the well known behaviour of the potentials on a target for an electron beam in place of the ion beam.

The target potential measurements with and without the magnetic field and in different gases demonstrate rather clearly that the potential variations along the ion beam and the longitudinal

electric field components are quite limited and depend upon thermal electron transport from the plasma along the beam. It is only by restricting this longitudinal electron transport that the longitudinal fields may arise. In this case strongly converging magnetic fields which should have been effective had, in fact, very little influence on the field developments. It thus seems clear that an ion beam is unable to develop longitudinal electric fields anywhere along its path in the presence of electrons of low thermal energy and which have no special restrictions along the path. The system is therefore stable and one would not expect two stream instability in counter-streams unless the electron temperature was sufficiently high with the average thermal energy of an electron comparable to the ion energy in the beam. This is a very extreme situation and essentially possible only in very low energy ion beams.

The experimental method for creating the dual beam system was admittedly crude and no coherent interactions were observed. Whether a system composed of two independent ion beams interacting in a plasma will give rise to standing waves remains to be seen. It is the author's opinion that these ion enhanced oscillations, if found at all, would be very weak and of little significance.

High Current Source

A hollow cathode argon arc was operated in a parallel magnetic field in the .1-micron range. Under optimum conditions, ions

diffusing radially from the 2.5-amp arc column allowed a steady, 200-ma argon ion beam to be extracted from the arc without the use of any external accelerating electrode. Measurements on this diffusion beam indicated that it was charge neutral with the beam velocity corresponding essentially to that provided by the arc potential. The beam current could be either completely defocused or enhanced by superimposing a diverging magnetic field from the anode on the already present focusing field from the external coils. A pulsed ion beam current, 2 to 4 times the steady value, could be obtained for 60 microseconds by applying a 200 to 400-volt pulse to the anode of the arc.

The purpose of this unusual source and intense low energy ion beam complimented the previous experiment for possible counter-streaming instabilities. It was becoming clearer at this point, however, that such instability as might arise from ion behaviour alone was of little possible significance and interest. On the other hand it was made evident that the source mechanism of this low energy beam did involve strong oscillations in the arc column coincident with the ions diffusing from the arc and forming the beam. From the results of the target potential measurements and the evidence for the stability of the ion stream in general, it followed that the instabilities in the arc stream associated with

the ion diffusion from the arc had to be associated with electron streaming within the arc column. For the ordinary arc running between the cathode and anode directly along the magnetic field, it is difficult to attain high amplitudes of instability, so in order to examine the arc instabilities more closely, the standard arc geometry used in the high current source was changed to the reflex arc.

Reflex Discharge

The situation for a reflex discharge in the magnetic field is quite different from the ordinary straight arc. For this kind of arc the electron current must cross the magnetic field and do so essentially by collective behaviour at the low pressures of operation. The reflex arc, therefore, operates by means of an electron beam instability. It thus appeared possible to alter the ion currents in the diffusion beam from the arc by changing the electron diffusion rates. The reflex discharge was then set up to study the control of diffusion by controlling the arc characteristics through geometry, pressure, and magnetic field changes.

The low frequency oscillations (25 - 100 kilocycles/sec) observed in the reflex discharge were found to be strongly dependent on the magnetic field, electrode separation, and button radius. The oscillations were slightly dependent on the pressure in the 0.06 to 1 micron range and independent of the arc current. Although no single theory has been developed which explains the

frequency dependence on all these arc parameters, a number of theories have been developed which contain features related to the observed dependences. The results found in this work will be compared, when possible, with the results and theories developed from other systems and considerations.

The screw instability in a relatively high pressure discharge (collision frequency being much greater than the gyrofrequency) discussed by Hoh states that the rotation frequency of the screw driven by an external E_z is given by

$$\omega = 5.5 b_+ D_- / \omega_- \tau_- b_- R^2 \quad (19)$$

where b_+ is the ion mobility, D_- is the electron diffusion coefficient, ω_- is the electron cyclotron frequency, τ_- is the electron - neutral collision time, b_- is the electron mobility, and R is the screw radius. The inverse magnetic field dependence and the independence of the discharge length does not correspond to our results, whereas the $1/R^2$ dependence corresponding to the different button radii does lie in the right direction. A longitudinal component of the electric field existed in our discharge, but the background pressure in the chamber was considerably lower than the high pressure discharge assumed by Hoh. Experimental results quoted by Hoh for a 2-micron hydrogen discharge in a 32-gauss field gave frequencies on the order of 30 kilocycles/sec, well within our

observed values. In a 300-micron helium discharge frequencies of 4×10^4 cycles/sec were observed when anomalous diffusion set in.

No external E_z was assumed to be required to drive the screw instability discussed by Guest and Simon.¹⁹ They assumed low pressure conditions ($\omega_+ \tau_+$ and $\omega_- \tau_-$ both very much greater than 1) and arrived at a frequency dependent on the reciprocal of the discharge length in agreement with what we found. However, no discharge diameter nor magnetic field dependence was noted from their first order frequency relation, Eq. (15).

Low frequency oscillations (10 - 30 kilocycles/sec) in a potassium plasma may be compared to our results in the argon discharge keeping in mind the fact that the ion masses are nearly the same.²⁸ The oscillations in the potassium discharge were found to be independent of both the magnetic field and discharge length, in disagreement with what we found.

A sound wave phenomenon has been used to explain low frequency oscillations in reflex discharges.²⁴ The frequencies in the 10 to 100 kilocycle/sec range were found experimentally to be inversely proportional to the discharge length in agreement with our results. However, the oscillations were found to be independent of the magnetic field, in disagreement with what we found. It was also noted that overtones could be excited by changing the electron current, also an effect we did not observe.

The "three fluid" model may be used to show that the oscillations are dependent on the button radius.²¹ This can be seen by noting that the radial component of the electric field, which should be a function of the button radius, is the driving mechanism for the instability in this model. Another point substantiating this instability mechanism is the fact that the third fluid neutral gas allows a smooth transition to the unstable mode as observed in our experiment. This is in contrast to the sharp onset of the screw instability.

In the various theories investigated, little mention was given to the frequency dependence on the discharge current. The independence of the frequency on the arc current in the limited range observed in our work indicates a frequency independence of the plasma density of the central arc column. This result and the fact that the oscillations were not observable in the central arc column implies that the instabilities arose off the arc axis immediately outside the primary source region of the discharge. A model developed around these two results and appearing to be consistent with the general trend of other instability models is presented in the following discussion.

The main plasma column, the length of which is determined by the button-cathode separation distance, is driven by a d. c. current-regulated power supply. A core of primary electrons thermionically emitted from the self-heated hollow cathode is initially confined to the axis of the discharge within a radius equal to

that of the hollow cathode. This is the region in Fig. 42 where the floating potential becomes negative and no coherent oscillations are found on the probe. These electrons are responsible for ionizing the argon gas and for forming the primary plasma column. With the button insulated from the anode, these electrons have to diffuse perpendicularly across the longitudinal magnetic field in order to reach the anode. The radial electric field generated or associated with this process couples with the magnetic field producing an azimuthal drift, $V_{\theta} = E_r/B$, of the charged particles. The rotational frequency of this drift velocity has been adjusted by the geometry changes in the system in the following ways.

The radial potential drop becomes larger for larger diameter buttons, but the region over which this drop occurs increases also, and at a faster rate. This results in an overall decrease of E_r and hence a decrease in the rotational drift frequency of the plasma. The increase of the observed frequencies with the magnetic field may be explained as follows. In a normal arc geometry, ions tend to diffuse radially at a rate greater than that of the electrons. With the anode-button geometry of this experiment shown in Fig. 19, the necessary radial electric field is in the opposite direction to ion diffusion since electrons must ultimately pass the edge of the button to reach the anode. An increase in B tends to suppress or restrict the electron transverse motion more than the ions, thus requiring a further increase in E_r to maintain the electron current

flow to the anode. The rate of increase of E_r is faster than the increase of B thereby increasing the drift velocity. The general decrease in the frequency as the arc length is increased may be explained by noting that the arc potential decreases also as the arc length is increased. The radial electric field, which is a function of the arc voltage, decreases resulting in a decrease of the rotational frequency. The oscillations found in the discharge are then the result of this rotational motion coupled to the longitudinal electron oscillatory motion generated in the potential well between the button and cathode.

From all points considered in this dissertation, it appears that the ion beam alone in a plasma is relatively stable in contrast to the electron beam-plasma system. No large potentials develop on the collector of an ion beam or along the beam as they do in the electron beam case and it is reasonable to assume that no large potential changes are induced in a plasma by an ion beam as in the electron beam case. In an arc consisting of both ion and electron streams, the situation is different. The streams may be unstable, but the instabilities are associated with the electron stream which in turn couples to the ion stream. Instabilities leading to enhanced diffusion allow diffusion limited, rather than space charge limited, high current ion beams to emanate from the arc. Our results indicate that a rotational motion initiated

by the magnetic field and dependent on the arc geometry is coupled to the observed longitudinal oscillations. Suitable changes in the arc geometry and magnetic field may enhance the diffusion process by shifting the natural arc frequencies toward system resonances. A point of note is that the critical magnetic field considered by many investigators to be associated with all enhanced diffusion experiments does not seem to be the important parameter governing anomalous diffusion.²⁹ It is, in fact, a combination of several parameters including the magnetic field, discharge length, and discharge radius which determines the observed frequencies that drive the particles outward.

This reflex arc arrangement and its behaviour relative to its geometry may have both academic interest and practical applications. As an example, seeding the arc with a gas that has an ion gyro-frequency in the range of the governed frequencies of the system could certainly lead to interesting results on the role of the ions in the diffusion process. On the other hand, this high current low energy ion beam has many possibilities for use as an ion engine without a great deal of basic alteration.

From the theoretical point of view, the problem is still unsolved since the boundary conditions of the finite geometry must be taken into account to provide the detailed solution. The results presented here are the first demonstration of this severe requirement.

LIST OF REFERENCES

1. D. Bohm and E. Gross, Phys. Rev. 79, 992 (1950).
2. Y. B. Fainberg, J. Nucl. Energy 4, 203 (1962).
3. B. N. A. Lamborn and D. L. Lafferty, Phys. Fluids 7, 292 (1964).
4. M. J. Kofoed, Phys. Fluids 5, 712 (1961).
5. D. Bohm and E. Gross, Phys. Rev. 75, 1851 (1949).
6. G. G. Kelley and O. B. Morgan, Phys. Fluids 4, 1446 (1961).
7. A. Guthrie and R. K. Wakerling, The Characteristics of Electrical Discharges in Magnetic Fields (McGraw Hill Book Co., Inc., New York, 1949).
8. A. Simon, Phys. Rev. 98, 317 (1955).
9. F. C. Hoh and B. Lehnert, Phys. Fluids 3, 600 (1960).
10. J. Bonnal, G. Brifford, and C. Manus, Phys. Rev. Letters 6, 65 (1961).
11. F. C. Hoh, Phys. Rev. Letters 4, 559 (1960).
12. B. B. Kadomtsev and A. V. Nedospasov, J. Nucl. Energy, Part C 1, 230 (1961).
13. T. K. Allen, G. A. Paulikas, and R. V. Pyle, Phys. Rev. Letters 5, 409 (1960).
14. F. C. Hoh, Phys. Fluids 5, 22 (1962).
15. F. C. Hoh and B. Lehnert, Phys. Rev. Letters 7, 71 (1961).
16. W. B. Thompson, An Introduction to Plasma Physics (Addison-Wesley Publishing Co. Inc., Reading, Massachusetts, 1962).
17. S. Glasstone and R. H. Lovberg, Controlled Thermonuclear Reactions (D. Van Nostrand Co. Inc., Princeton, New Jersey, 1960).

18. W. A. Perkins and R. F. Post, Phys. Fluids 6, 1537 (1963).
19. G. Guest and A. Simon, Phys. Fluids 5, 503 (1962).
20. F. Schwirzke, Phys. Fluids 7, 311 (1964).
21. F. C. Hoh, Phys. Fluids 6, 1184 (1963).
22. F. F. Chen and A. W. Cooper, Phys. Rev. Letters 9, 333 (1962).
23. F. W. Crawford, Phys. Rev. Letters 6, 663 (1961).
24. I. Alexeff and R. V. Neidigh, Phys. Rev. 129, 516 (1963).
25. L. Tonks and I. Langmuir, Phys. Rev. 33, 195 (1929).
26. Progress Report, U. S. A. E. C. Division of Controlled Thermonuclear Branch Contract AT-(40-1) 2783 (University of Florida, 8, 1962).
27. W. A. Dunnill, M. S. Thesis (University of Florida, 6, 1962, Unpublished).
28. N. D'Angelo and R. W. Mottey, Phys. Fluids 6, 442 (1963).
29. F. Boeschoten, J. Nucl. Energy 6, 339 (1963)

Other References

- P. L. Auer, H. Hurwitz, and R. D. Miller, Phys. Fluids 1, 501 (1958).
- L. S. Hall, W. Heckrotte, and T. Kammash, Phys. Rev. Letters 13, 603 (1964).
- D. L. Morse, Phys. Fluids 8, 516 (1965).
- M. V. Nezlin and A. M. Solntsev, J. E. T. P. 18, 576 (1963).
- T. H. Stix, Phys. Fluids 7, 1960 (1964).
- K. I. Thomassen, Phys. Rev. Letters 14, 587 (1965)

BIOGRAPHICAL SKETCH

William Arthur Dunnill was born in Chicago, Illinois, on November 30, 1937. In 1955, he graduated from Proviso Township High School, Maywood Illinois. In September, 1955, he entered Rollins College in Winter Park, Florida where he received the Bachelor of Science degree in physics in June, 1959. In September, 1959, he entered the Graduate School of the University of Florida where he received the Master of Science degree in physics in June, 1962. On April 21, 1963, he married the former Alice Frances Connor of St. Petersburg, Florida. While pursuing his graduate studies, he held assistantships from the Physics Department and from an Atomic Energy Commission Contract.

This dissertation was prepared under the direction of the chairman of the candidate's supervisory committee and has been approved by members of that committee. It was submitted to the Dean of the College of Arts and Sciences and to the Graduate Council, and was approved as partial fulfillment of the requirements for the degree of Doctor of Philosophy.

June 22, 1965

E. R. Pifer
Dean, College of Arts and Sciences

Dean, Graduate School

SUPERVISORY COMMITTEE:

John W. Flowers
Chairman

John Krenshaw

L. Bailey

L. Ehlmann

John Cowan

2
1
3202